



# Durham E-Theses

---

## *A Study of Streamwise Vortex Interactions*

MARSHALL, ADAM

### How to cite:

---

MARSHALL, ADAM (2021) *A Study of Streamwise Vortex Interactions*, Durham theses, Durham University. Available at Durham E-Theses Online: <http://etheses.dur.ac.uk/14361/>

### Use policy

---

The full-text may be used and/or reproduced, and given to third parties in any format or medium, without prior permission or charge, for personal research or study, educational, or not-for-profit purposes provided that:

- a full bibliographic reference is made to the original source
- a [link](#) is made to the metadata record in Durham E-Theses
- the full-text is not changed in any way

The full-text must not be sold in any format or medium without the formal permission of the copyright holders.

Please consult the [full Durham E-Theses policy](#) for further details.

# A Study of Streamwise Vortex Interactions

Adam Marshall

## Abstract

Wind tunnel experiments and numerical simulations using RANS modelling were conducted to investigate the effect of a wall on the evolution of co and counter-rotating vortex pairs. The counter-rotating vortices had a mutually induced velocity that moved the pair away from the wall. Such pairs occur in the wakes of race car front and rear wings, as well as other areas of race cars where vortices are used for flow control purposes. In the experiments, two vortices were generated using two vortex generators, with NACA0012 profiles, attached to a flat plate. Whereas in the simulations the superposition of two Batchelor vortices was used to investigate the evolution of a vortex pair. Despite differences in Reynolds number, there was good correlation between the experiments and simulations. It was found that the presence of a wall increases the rate at which co-rotating vortices move towards each other and merge. This is due to the lateral and vertical induced velocities due to the image vortices and secondary vorticity respectively. At very low initial heights two initially symmetric vortices will merge like an asymmetric pair. The rate of rotation of the co-rotating pairs increased with decreasing initial height, until the initial height became too small and the rotation was inhibited. The generation of secondary vorticity and the interaction between primary vortices and this secondary vorticity was shown to accelerate the decay of circulation for both co and counter-rotating pairs. For counter-rotating pairs whose mutually induced velocity moved the pair away from the wall, the secondary vorticity was found to have little effect on the trajectory. That is significantly different from counter-rotating pairs whose mutually induced velocity moves the pair towards the wall, which rebound multiple times.

# A Study of Streamwise Vortex Interactions

Adam Marshall

Supervised by

Dr. Lian Gan and Prof. D. B. Sims-Williams

A thesis submitted for the degree of  
Master of Science by Research



Department of Engineering

Durham University

2021

# Contents

List of Figures . . . . .	viii
List of Tables . . . . .	ix
List of Abbreviations . . . . .	x
List of Symbols . . . . .	xi
Statement of Copyright . . . . .	xii
Acknowledgement . . . . .	xiii
<b>1 Introduction</b>	<b>1</b>
<b>2 Literature Review</b>	<b>3</b>
2.1 Co-Rotating Vortices . . . . .	3
2.1.1 Properties of a Co-Rotating Vortex Pair . . . . .	3
2.1.2 The Merging of Co-Rotating Vortices . . . . .	5
2.2 Counter-Rotating Vortices . . . . .	10
2.2.1 Properties of Counter-Rotating Vortex Pairs . . . . .	10
2.2.2 Instabilities . . . . .	13
<b>3 Experimental Methodology</b>	<b>21</b>
3.1 Wind Tunnel and Measurement Technique . . . . .	21
3.2 Experimental Geometry . . . . .	25
<b>4 CFD Methodology</b>	<b>28</b>
4.1 Turbulence Modelling . . . . .	28
4.1.1 Reynolds Averaged Navier-Stokes Equations . . . . .	28
4.1.2 Turbulence Model . . . . .	29
4.2 Numerical Procedure . . . . .	31
4.2.1 Discretisation . . . . .	31

4.2.2	Solution Algorithm . . . . .	31
4.2.3	Convergence Criteria . . . . .	33
4.3	Computational Domain . . . . .	33
4.3.1	Boundary Conditions . . . . .	33
4.3.2	Mesh . . . . .	34
<b>5</b>	<b>Results</b>	<b>39</b>
5.1	Co-Rotating Results . . . . .	40
5.2	Counter-Rotating Results . . . . .	76
<b>6</b>	<b>Discussion</b>	<b>89</b>
6.1	Comparison Between Experimental and Numerical Co-Rotating Cases and Limitations . . . . .	89
6.2	Vortex Merging . . . . .	91
6.3	Decay of Circulation . . . . .	96
6.3.1	Co-Rotating Pairs . . . . .	96
6.3.2	Counter-Rotating Pairs . . . . .	101
6.4	Vortex Pair Trajectories . . . . .	103
6.4.1	Co-Rotating Pairs . . . . .	103
6.4.2	Counter-Rotating Pairs . . . . .	104
<b>7</b>	<b>Conclusions and Future Work</b>	<b>107</b>
7.1	Conclusions . . . . .	107
7.2	Future Work . . . . .	109

# List of Figures

2.1	Trajectories of equal strength (left) and unequal strength (right) co-rotating point vortex pairs from Leweke et al. . . . .	4
2.2	Streamline patterns of an equal strength co-rotating pair in the comoving frame from Leweke et al. . . . .	4
2.3	Elliptical streamlines due to the induced strain for a co-rotating vortex pair from Leweke et al. . . . .	5
2.4	Normalised core separation during vortex merging from Cerretelli and Williamson. . . . .	6
2.5	Vorticity distribution and streamlines in the corotating frame for a vortex pair at $Re = 530$ from Cerretelli and Williamson. . . . .	6
2.6	Total vorticity, symmetric vorticity and antisymmetric vorticity for a vortex pair at $Re = 530$ from Cerretelli and Williamson. . . . .	7
2.7	Vorticity contours for different ratios of initial vortex circulation, showing the different types of unequal vortex merging from Brandt and Nomura. . . . .	8
2.8	Vorticity contours for a co-rotating vortex pair in ground effect from Wang et al. . . . .	9
2.9	Streamline patterns of an equal strength counter-rotating pair in the comoving frame from Leweke et al. . . . .	10
2.10	Elliptical streamlines due to the induced strain for a counter-rotating vortex pair from Leweke et al. . . . .	10
2.11	Trajectories of counter-rotating point vortex pairs from Leweke et al.	11
2.12	Actual (black line) and ideal (grey line) trajectories of a counter-rotating vortex pair approaching a wall from Kramer et al. . . . .	12

2.13	Vorticity contour plots showing the evolution of one vortex of a pair colliding with a no-slip wall. . . . .	13
2.14	A sketch of the evolution of the Crow Instability from Lweke and Williamson. . . . .	14
2.15	Diagram of the Crow instability from Lweke et al. . . . .	14
2.16	(a) The stability diagram for an equal strength counter-rotating vortex pair (The region where $\frac{a_e}{b} > 0.5$ has no physical meaning because the cores are overlapping there) (b) The growth rate of the Crow instability as a function of normalised axial wavelength, where the symbols represent experimental measurements from Lweke et al. . .	15
2.17	Primary vorticity for the vertical rings mode, from the experimental work of Asselin and Williamson. . . . .	17
2.18	Secondary vorticity for the vertical rings mode, from the experimental work of Asselin and Williamson. . . . .	18
2.19	The normalised amplitudes of the unbounded, large rings mode and vertical rings mode Crow Instability from Asselin and Williamson. .	19
2.20	Water tank visualisation of elliptic instability: (a) For a counter-rotating pair at $Re_\Gamma = 2750$ from Lweke and Williamson . . . . .	20
3.1	Plan, side and isometric views of the Durham 1m Wind Tunnel . . .	21
3.2	(a) Schematic of a five hole pneumatic pressure probe. (b) A view of the five hole probe tip, with the number of each hole shown in red. .	24
3.3	Five hole probe calibration. . . . .	25
3.4	The vortex generators and flat plate experimental setup. . . . .	27
3.5	The vortex generators and flat plate experimental setup. . . . .	27
4.1	The SIMPLE algorithm . . . . .	32
4.2	The computational domain and boundary conditions. . . . .	34
4.3	The superposition of two Batchelor vortices. . . . .	34
4.4	Variation in vortex circulation in the planes $x = 20a_0$ (blue), $x = 40a_0$ (red) and $x = 60a_0$ (green) due to changes in mesh density. . . . .	35
4.5	Variation in vortex centroid in the planes $x = 20a_0$ (blue), $x = 40a_0$ (red) and $x = 60a_0$ (green) due to changes in mesh density. . . . .	36

4.6	(a) The mesh in the region containing the vortices and (b) the mesh region near the edges of the domain, away from the vortices. . . . .	38
5.1	Contours of $\omega_x$ for Experimental Co-Rotating Case 1. . . . .	41
5.2	Vortex centroids for Experimental Co-Rotating Case 1. . . . .	41
5.3	Contours of $\omega_x$ for Experimental Co-Rotating Case 2. . . . .	42
5.4	Vortex centroids for Experimental Co-Rotating Case 2 . . . . .	43
5.5	Contours of $\omega_x$ for Co-Rotating Case 1. . . . .	44
5.6	Vortex centroids for Co-Rotating Case 1. The trajectories in the XY plane are shown on the left and in the XZ plane on the right. . . . .	45
5.7	Definition of the angle of orientation, theta. . . . .	46
5.8	Vortex centroids for a single vortex ( $\frac{h_0}{a_0} = 1.67$ ). The trajectories in the XY plane are shown on the left and in the XZ plane on the right. . . . .	46
5.9	Contours of $\omega_x$ for Co-Rotating Case 2. . . . .	47
5.10	Vortex centroids for Co-Rotating Case 2. The trajectories in the XY plane are shown on the left and in the XZ plane on the right. . . . .	48
5.11	Angle of orientation for Co-Rotating Case 2. . . . .	48
5.12	A schematic of a co-rotating vortex pair and secondary vorticity very close to the ground. The image vortices are shown below the plate. . . . .	50
5.13	Contours of $\omega_x$ for Co-Rotating Case 3. . . . .	51
5.14	Vortex centroids Co-Rotating Case 3. The trajectories in the XY plane are shown on the left and in the XZ plane on the right. . . . .	52
5.15	Angle of orientation for Co-Rotating Case 3. . . . .	52
5.16	Contours of $\omega_x$ for a Co-Rotating Case 4. . . . .	54
5.17	Vortex centroids for Co-Rotating Case 4. The trajectories in the XY plane are shown on the left and in the XZ plane on the right. . . . .	55
5.18	Angle of orientation for Co-Rotating Case 4. . . . .	55
5.19	Contours of $\omega_x$ for Co-Rotating Case 5. . . . .	57
5.20	Vortex centroids for Co-Rotating Case 5. The trajectories in the XY plane are shown on the left and in the XZ plane on the right. . . . .	58
5.21	Angle of orientation for Co-Rotating Case 5. . . . .	58
5.22	Contours of $\omega_x$ for Co-Rotating Case 6. . . . .	60
5.23	Vortex centroids for Co-Rotating Case 6. The trajectories in the XY plane are shown on the left and in the XZ plane on the right. . . . .	61

5.24	Angle of orientation for Co-Rotating Case 6. . . . .	61
5.25	A schematic of a co-rotating vortex pair and secondary vorticity in ground effect, but further from the ground than in Figure 5.12. The image vortices are shown below the plate. . . . .	63
5.26	Contours of $\omega_x$ for Co-Rotating Case 7. . . . .	63
5.27	Vortex centroids for Co-Rotating Case 7. The trajectories in the XY plane are shown on the left and in the XZ plane on the right. . . . .	64
5.28	Angle of orientation for Co-Rotating Case 7. . . . .	64
5.29	Contours of $\omega_x$ for Co-Rotating Case 8. . . . .	66
5.30	Vortex centroids for Co-Rotating Case 8. The trajectories in the XY plane are shown on the left and in the XZ plane on the right. . . . .	67
5.31	Angle of orientation for Co-Rotating Case 8. . . . .	67
5.32	Contours of $\omega_x$ for Co-Rotating Case 9. . . . .	69
5.33	Vortex centroids for Co-Rotating Case 9. The trajectories in the XY plane are shown on the left and in the XZ plane on the right. . . . .	70
5.34	Angle of orientation for Co-Rotating Case 9. . . . .	70
5.35	Contours of $\omega_x$ for Co-Rotating Case 10. . . . .	72
5.36	Vortex centroids for Co-Rotating Case 10. The trajectories in the XY plane are shown on the left and in the XZ plane on the right. . . . .	73
5.37	Angle of orientation for Co-Rotating Case 10. . . . .	73
5.38	Contours of $\omega_x$ for Co-Rotating Case 11. . . . .	75
5.39	Vortex centroids for Co-Rotating Case 11. The trajectories in the XY plane are shown on the left and in the XZ plane on the right. . . . .	76
5.40	Angle of orientation for Co-Rotating Case 11. . . . .	76
5.41	A schematic of the configuration of the counter-rotating vortex pairs investigated. U is the vertical velocity each vortex induces upon the other and b is the separation distance. . . . .	77
5.42	Contours of $\omega_x$ for Counter-Rotating Case 1. . . . .	78
5.43	Vortex centroids for Counter-Rotating Case 1. The trajectories in the XY plane are shown on the left and in the XZ plane on the right. . . . .	79
5.44	A schematic of a counter-rotating vortex pair close to the ground and it's image vortices. . . . .	80
5.45	Contours of $\omega_x$ for Counter-Rotating Case 2. . . . .	81

5.46	Vortex centroids for Counter-Rotating Case 2. The trajectories in the XY plane are shown on the left and in the XZ plane on the right. . . . .	82
5.47	Contours of $\omega_x$ for Counter-Rotating Case 3. . . . .	83
5.48	Vortex centroids for Counter-Rotating Case 3. The trajectories in the XY plane are shown on the left and in the XZ plane on the right. . . . .	84
5.49	Contours of $\omega_x$ for Counter-Rotating Case 4. . . . .	85
5.50	Vortex centroids for Counter-Rotating Case 4. The trajectories in the XY plane are shown on the left and in the XZ plane on the right. . . . .	86
5.51	Contours of $\omega_x$ for Counter-Rotating Case 5. . . . .	87
5.52	Vortex centroids for Counter-Rotating Case 5. The trajectories in the XY plane are shown on the left and in the XZ plane on the right. . . . .	88
6.1	The change in vortex separation for vortex pairs at the same initial height, $\frac{h_0}{a_0} = 1.667$ but varying initial spacings. . . . .	91
6.2	The change in vortex separation for the experimental cases, which had an initial height of $\frac{h_0}{a_0} = 1.73$ and initial spacings of $\frac{a_0}{b_0} = 0.12$ and $\frac{a_0}{b_0} = 0.32$ respectively. . . . .	92
6.3	The change in vortex separation for vortex pairs at the same initial spacing, $\frac{a_0}{b_0} = 0.2$ , but varying initial heights. . . . .	92
6.4	The change in vortex separation for vortex pairs at the same initial spacing, $\frac{a_0}{b_0} = 0.3$ , but varying initial heights. . . . .	93
6.5	A schematic of a co-rotating vortex pair with an angle of orientation of (a) $0 \leq \theta \leq 90^\circ$ and (b) $90^\circ \leq \theta \leq 180^\circ$ . . . . .	94
6.6	The circulation outside of the core region for vortex pairs at the same initial spacing of $\frac{a_0}{b_0} = 0.3$ , but varying initial heights. . . . .	95
6.7	Circulation for: (a) vortex pairs at multiple spacings and an initial height of $\frac{h_0}{a_0} = 1.67$ (b) vortex pairs at an initial spacing of $\frac{a_0}{b_0} = 0.2$ and multiple heights and (c) vortex pairs at an initial spacing of $\frac{a_0}{b_0} = 0.3$ and multiple heights. . . . .	97
6.8	Circulation for the Experimental Co-Rotating Vortex Pairs at initial spacings of: $\frac{a_0}{b_0} = 0.12$ and $\frac{a_0}{b_0} = 0.32$ . . . . .	98

6.9	Secondary Circulation for: (a) vortex pairs at multiple spacings and an initial height of $\frac{h_0}{a_0} = 1.67$ (b) vortex pairs at an initial spacing of $\frac{a_0}{b_0} = 0.2$ and multiple heights and (c) vortex pairs at an initial spacing of $\frac{a_0}{b_0} = 0.3$ and multiple heights. . . . .	100
6.10	Turbulent kinetic energy for: (a) vortex pairs at multiple spacings and an initial height of $\frac{h_0}{a_0} = 1.67$ (b) vortex pairs at an initial spacing of $\frac{a_0}{b_0} = 0.2$ and multiple heights and (c) vortex pairs at an initial spacing of $\frac{a_0}{b_0} = 0.3$ and multiple heights. . . . .	101
6.11	The circulation at multiple downstream locations for counter-rotating pairs at multiple initial spacings and an initial height of $\frac{h_0}{a_0} = 1.67$ . .	102
6.12	The circulation of secondary vorticity at multiple downstream locations for counter-rotating pairs at multiple initial spacings and an initial height of $\frac{h_0}{a_0} = 1.67$ . . . . .	103
6.13	The trajectories counter-rotating vortices for simulation with a no slip condition applied to the ground and a slip condition applied to the ground. The initial spacings of the vortex pairs are: (a) $\frac{a_0}{b_0} = 0.1$ , (b) $\frac{a_0}{b_0} = 0.3$ (c) $\frac{a_0}{b_0} = 0.5$ . . . . .	106

# List of Tables

4.1	The GCI for circulation. . . . .	36
4.2	Variation in vortex pair circulation at $x = 80a_0$ for differing domain widths compared to the widest domain tested. . . . .	37
4.3	Variation in vortex pair circulation at $x = 80a_0$ for differing domain heights compared to the largest domain tested. . . . .	37
5.1	List of Cases . . . . .	40

# List of Abbreviations

<b>Abbreviation</b>	<b>Definition</b>
CFD	Computational Fluid Dynamics
CAD	Computer Aided Design
RANS	Reynolds Averaged Navier-Stokes
VG	Vortex Generator
DNS	Direct Numerical Simulation
LES	Large Eddy Simulation

# List of Symbols

<b>Symbol</b>	<b>Definition</b>
$\Gamma$	Circulation
$\Gamma_0$	Initial Circulation
$\Gamma_s$	Secondary Circulation
Re	Reynolds Number
$Re_\Gamma$	Reynolds Number Based on Circulation
$\omega_x$	Streamwise Vorticity
b	Vortex Pair Separation
$b_0$	Initial Vortex Separation
a	Vortex Core Size
$a_0$	Initial Vortex Core Size
$y^+$	Dimensionless Wall Distance
$\theta$	Angle of Orientation
h	Height of Vortex Above Ground
$h_0$	Initial Height of Vortex Above Ground
$Y_c$	Vortex Centroid Y Component
$Y_z$	Vortex Centroid Z Component
$C_{p_{dyn}}$	Dynamic Pressure Coefficient
$C_{p0}$	Static Pressure Coefficient
$C_{pitch}$	Pitch Coefficient
$C_{yaw}$	Yaw Coefficient
C	Chord Length
$\omega$	Specific Turbulence Dissipation Rate
k	Turbulent Kinetic Energy
$\mu_t$	Turbulent Viscosity

# Statement of Copyright

The copyright of this thesis rests with the author. No quotation from it should be published without the author's prior written consent and information derived from it should be acknowledged.

# Acknowledgement

I would like to thank my supervisors, Dr Lian Gan and Professor David Sims-Williams, for their support and advice throughout this project. I would also like to thank Gary Parker for his assistance in the laboratory, as well as his work to open the lab after lockdown.

# Chapter 1

## Introduction

Modern race cars utilise vortices to improve performance, for example, to increase mass flow under the car and increase downforce. This results in multiple interacting vortices near a solid boundary. These vortices can be counter or co-rotating and of equal or unequal strength [1, 2]. Zhang et al attributed an increase in downforce for a race car front wing with decreasing ride height to the wing tip vortices inducing suction on the surface [2]. Other examples of interacting vortices near a solid boundary in practical flows are submarines, on surfaces such as aircraft wings where vortices are used to provide momentum addition into the boundary layer and delay separation and aircraft trailing vortices during take off or landing [3, 4, 5]. Aircraft vortices are often modelled as an equal strength counter-rotating pair, however in high-lift configurations with part-span flaps, more than two vortices are produced [6]. One model is of a four vortex system containing two unequal strength co-rotating pairs [7]. The majority of the existing research on vortex pairs in ground effect focuses on counter-rotating vortex pairs whose mutually induced velocity moves the pair towards the wall, and as such not studied in this research. Because of that, little is known about the effect of a wall on the evolution and merging of a co-rotating vortex pair. As well as the effect of a wall on the evolution of a counter-rotating vortex pair whose mutually induced velocity moves the pair away from the wall. Such a vortex pair close to the ground occurs in the wake of race car front and rear wings [8], inside the rear diffuser of a race car [2] and around the bargeboard area of a race car, where vortices are utilised for flow control purposes [1].

This research aims to identify the effect of being in close proximity to a wall on the evolution of a vortex pair, as well as the effect of initial spacing on the evolution

of the pair, using both experimental and numerical techniques. To achieve this wind tunnel testing of vortices generated by two vortex generators at multiple spacings will be completed. As well as this, numerical simulations using OpenFOAM of both co-rotating and counter-rotating vortex pairs with different initial parameters will be conducted. To achieve this a pneumatic 5 hole probe will be calibrated so that it can be used to take measurements during the wind tunnel tests. Vortex generators, as well as a method of mounting them within the wind tunnel in such a way that the angle of attack can easily be adjusted, will be designed and manufactured. To allow vortex pairs to be analysed numerically, code that sets the inlet velocity of the computational domain to the superposition of two Batchelor vortices and allows the initial parameters to be adjusted will be produced. The data from this work will then be used to calculate the trajectories of the vortices, so that the effect of ground and initial spacing can be identified. Counter-rotating vortex pairs whose mutually induced velocity moves the pair away from the ground will be investigated, as much less research exists for such counter-rotating pairs. The effect of the proximity of the ground as well as the initial spacing on the merging of co-rotating vortices will be investigated by calculating the separation distance between the vortices at multiple planes and analysing how this changes. It has been identified that the ground effect promotes merging, however this was only investigated at one height above the ground [9], this research will investigate vortex pairs at multiple heights above the ground to further study this promoted merging. The circulation of the vortex pairs will be calculated for all cases, which will allow the effect of the ground on the decay of this to be identified. As well as the mechanism by which this decay occurs.

## Chapter 2

# Literature Review

### 2.1 Co-Rotating Vortices

Vortices in practical flows will interact with other vortices of the same sense (co-rotating) and opposite sense rotation (counter-rotating) and both equal and unequal strength. In this section the case of co-rotating vortices is considered.

#### 2.1.1 Properties of a Co-Rotating Vortex Pair

If the total circulation is non zero,  $\Gamma_{total} \neq 0$ , for counter or co-rotating vortex pair there will be rotation of the system. Thus, co-rotating vortices will rotate about a point between the two vortex centres because of the mutually induced velocity. This point is the invariant vorticity centre, and for a point vortex pair is given by  $(\Gamma_1 \mathbf{X}_1^c + \Gamma_2 \mathbf{X}_2^c)/(\Gamma_1 + \Gamma_2)$ , with an angular velocity given by  $(\Gamma_1 + \Gamma_2)/(2\pi b^2)$ , where  $\mathbf{X}_1^c$  and  $\mathbf{X}_2^c$  are the centres of the two vortices respectively and  $b$  is the separation distance of the vortex centroids [10]. The trajectories of co-rotating pairs are shown in Figure 2.1.  $\Omega$  is the angular velocity of the pair around the invariant vorticity centre and it can be seen that for an unequal strength pair, this centre is not at the mid point between the vortices, as is the case with an equal strength pair.

A co-rotating vortex pair in a co-moving reference frame it consists of multiple regions, as shown in Figure 2.2 from Leweke et al. [10], bounded by separatrices. The regions consist of an outer recirculation region, an inner core region and the region between the two called the inner recirculation region. Within the inner core region the flow is like two single vortices, moving outwards to the inner recirculation region the fluid flows around both vortices. Within the outer recirculation region

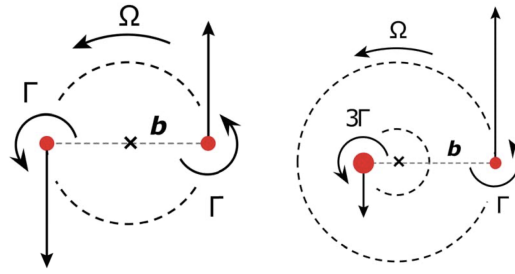


Figure 2.1: Trajectories of equal strength (left) and unequal strength (right) co-rotating point vortex pairs from Leweke et al. [10]

the fluid behaves like a pair of secondary vortices, termed ghost vortices. These regions, identified by Leweke et al. [10], are crucial to understanding the process of vortex merging.

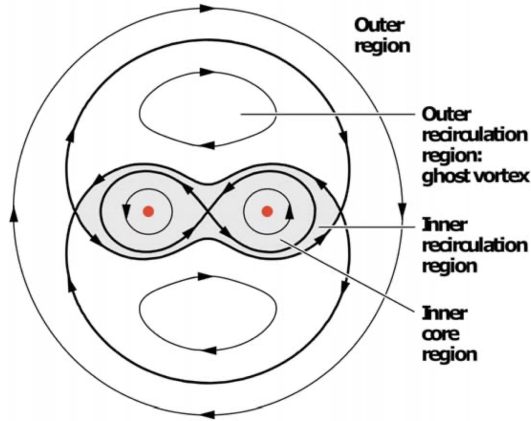


Figure 2.2: Streamline patterns of an equal strength co-rotating pair in the comoving frame from Leweke et al. [10]

Each vortex in the pair induces upon the other a strain field resulting in a stretching of the vortices. Due to the strain and rotation, the streamlines become elliptical, orientated at an angle  $45^\circ$  to the principle stretching axis. This is shown in Figure 2.3, from Leweke et al. [10]. A vortex of  $\Gamma_1$  generates a strain field at the centre of vortex  $\Gamma_2$  of amplitude  $S_e = \Gamma_1/(2\pi b^2)$ . The deformation caused by the external strain further increases the strain within the vortex, thus the strain rate at the centre of the vortex is larger than the strain rate induced by the presence of the other vortex. [10]

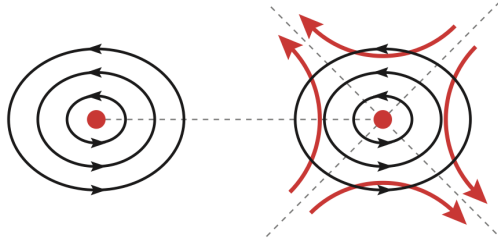


Figure 2.3: Elliptical streamlines due to the induced strain for a co-rotating vortex pair from Leweke et al. [10]

### 2.1.2 The Merging of Co-Rotating Vortices

The onset of merging for a pair of co-rotating vortices occurs at a critical normalised core size,  $a/b$ , where  $a$  is the core size and  $b$  is the separation distance. Early work to determine this value was undertaken by Saffman and Szeto, Overman and Zabusky, and Dritschel [11, 12, 13]. All of these studies utilised numerical methods focusing on uniform vorticity patches in two dimensions. They found the critical size to be 0.29 to 0.32. Meunier et al experimentally measured  $a/b_{cr} = 0.24 \pm 0.01$ . [14] In order to deduce this value the core size was defined as  $a = (\frac{1}{\Gamma} \int_S |\mathbf{X} - \mathbf{X}^c|^2 \omega_x dS)^{0.5}$ , where  $\omega_x$  is the streamwise vorticity,  $\mathbf{X}$  is the displacement and  $\mathbf{X}^c$  is the vortex centroid. This means that the calculated  $a/b_{cr}$  is independent of vorticity distribution.

For an equal strength co-rotating pair there are 4 stages of vortex merging: the first diffusive stage, the convective stage, the second diffusive stage and the merged diffusive stage. Initially, Melander et al identified two stages of merging, the viscous metastable stage and the convective stage. [15] The merged diffusive stage was then identified by Meunier and Leweke [16] and Meunier et al [14], then the second diffusive stage was defined by Cerretelli and Williamson [17]. During the first diffusive stage the vortex cores grow due to viscous diffusion with very little change in separation distance,  $b$ . The growth of the cores follows the viscous diffusion law,  $a^2 = a_0^2 + 4\nu t$ , where  $a_0$  is the initial core size,  $\nu$  is kinematic viscosity and  $t$  is time [16]. This stage of merging continues until a critical core size is reached, as mentioned above, at which point the convective stage begins. During this stage there is a rapid decrease in separation distance, as shown in Figure 2.4. It was found by Meunier et al that this is because some vorticity is advected to the outer region, which moves the cores together in order for total momentum to be conserved

[18]. During the second diffusive stage the separation distance decreases slowly due to Biot-Savart induction [10]. Finally, during the merged diffusive stage the vortex becomes more axisymmetric.

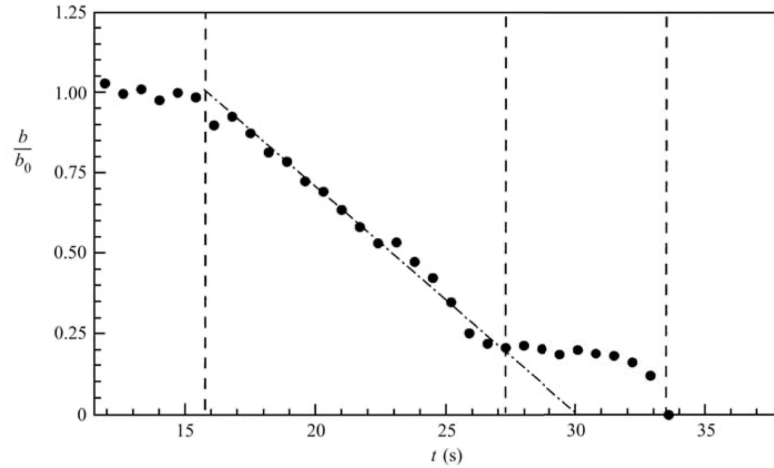


Figure 2.4: Normalised core separation during vortex merging from Cerretelli and Williamson. [17]

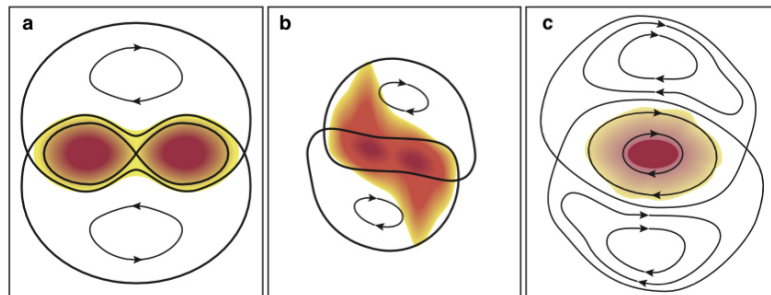


Figure 2.5: Vorticity distribution and streamlines in the corotating frame for a vortex pair at  $Re = 530$  from Cerretelli and Williamson. [17]

In order to determine the reason for the rapid reduction in  $b$  during the convective stage, Cerretelli and Williamson superimposed the vorticity onto the streamlines in the comoving frame, as shown in Figure 2.5 [17]. In Figure 2.5a the vorticity is diffusing from the inner core region to the inner recirculation region, then in Figure 2.5b filaments have formed extending into the outer recirculation region. This is because vorticity is convected by the velocity field up and to the left of the left vortex core and down to the right of the right vortex core. Focusing on the left hand vortex, the effect of the filament, which consists of anti-clockwise vorticity, is to induce a velocity on the vortex centre. The filament is below and to the right of the

vortex centre so the induced velocity is to the left, thus the vortices move towards each other. In order to determine what vorticity is responsible for the convective merging, Cerretelli and Williamson decomposed the skewed vorticity into symmetric and antisymmetric vorticity [17]. To do so the vorticity was made skewsymmetric (symmetric about the origin) and the vorticity was decomposed as follows

$$\omega_x(x, y) = \frac{1}{2} [\omega_x(x, y) + \omega_x(x, -y)] + \frac{1}{2} [\omega_x(x, y) - \omega_x(x, -y)] \quad (2.1)$$

From this, it was found that the induced horizontal velocity due to the symmetric vorticity anywhere along the axis passing through the vortex centroids is 0. The antisymmetric vorticity is comprised of two counter-rotating vortex pairs where the induced velocities drive the vortex centroids together. This is shown in Figure 2.6 from Cerretelli and Williamson [17].

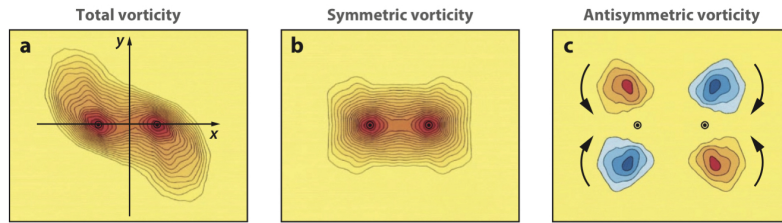


Figure 2.6: Total vorticity, symmetric vorticity and antisymmetric vorticity for a vortex pair at  $Re = 530$  from Cerretelli and Williamson. [17]

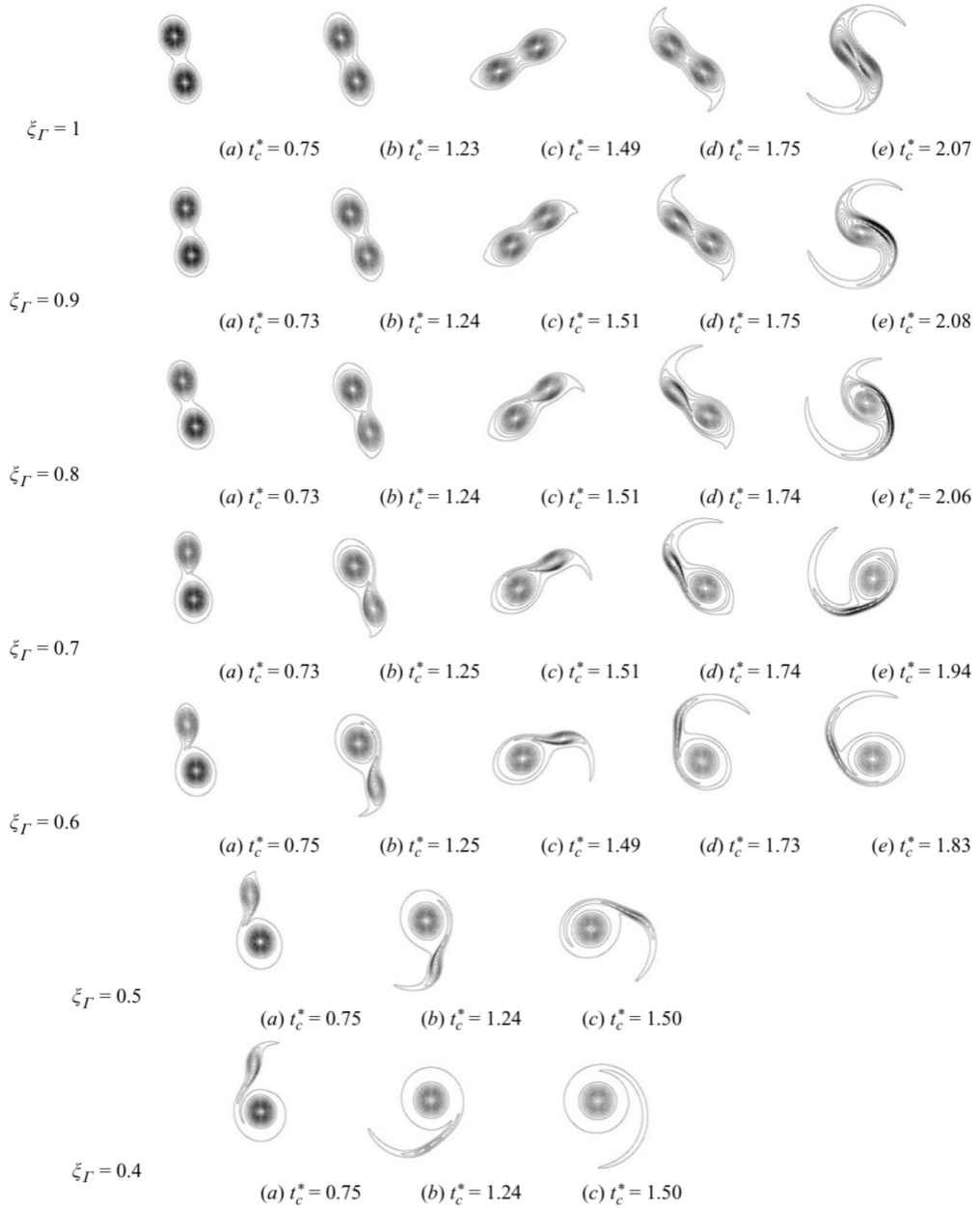


Figure 2.7: Vorticity contours for different ratios of initial vortex circulation, showing the different types of unequal vortex merging from Brandt and Nomura. [19]

In the case of vortices of different size or circulation, partial merger, partial straining out or complete straining out can occur [10], shown in Figure 2.7. Using contour simulations, Dritschel and Waugh [20] observed that the interaction between a pair of vortices with a large difference in size is significantly different than the interaction of a pair of vortices with a small discrepancy in size. Often a vortex pair with a large difference in size results in partial or complete straining of the

smaller vortex. For a pair of more similar sized vortices, the result is an increase in larger vortex size, complete merger, or a smaller small vortex, partial merger. They defined the different asymmetric vortex pair interactions based on normalised circulation. These interactions occur when one vortex is too weak to support the strain field induced by the other vortex and the weaker vortex is elongated [21, 22] or vorticity is stripped from the weaker vortex by an erosion process [23, 24].

Studies of vortex merging in proximity to the ground are limited. Wang et al experimentally investigated a co-rotating pair in ground effect [9], at  $h_0/b_0 = 1.0$ , where  $h_0$  is initial vortex height and  $b_0$  is initial vortex separation. A secondary vortex was formed, which is believed to be the cause of the upwards motion of the pair, much like for a counter-rotating pair in ground effect. It was found that the proximity of the ground promoted merging as the vortex separations, initially equal for both cases, were smaller for the in ground effect pair at downstream locations. Wang et al. concluded that the ground effect promoted the merger of the vortices because the of lateral movement induced by the ground and the vertical movement induced by the secondary vorticity. The velocities induced on the vortex closer to the ground, so for certain orientations of the vortex pair, resulting in the vortices moving towards each other. When the angle of orientation of the vortex pair, defined in Figure 5.7, between  $0^\circ$  and  $90^\circ$ , both the effect of the image vortices and the secondary vortex induced velocities upon the primary vortices which reduced the separation distance,  $b$ . For angles of orientation between  $90^\circ$  and  $180^\circ$ , the image vortex effect increased the separation distance whilst the secondary vortex still had the effect of reducing  $b$ . It was also observed that the pair in ground effect had an accelerated rotational rate and moved laterally and upwards.

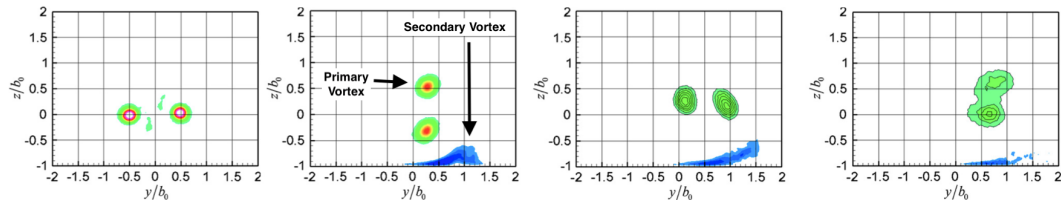


Figure 2.8: Vorticity contours for a co-rotating vortex pair in ground effect from Wang et al. [9]

## 2.2 Counter-Rotating Vortices

### 2.2.1 Properties of Counter-Rotating Vortex Pairs

The streamlines in the comoving frame for an equal strength counter-rotating vortex pair are less complex than those of a co-rotating pair, consisting only of an inner and outer region, shown in Figure 2.9 [10].

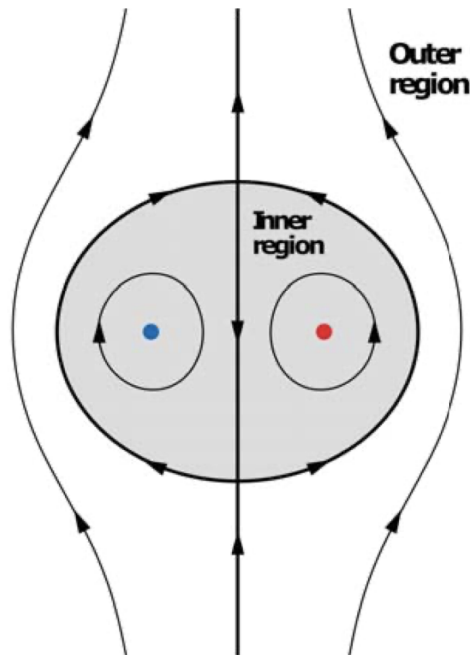


Figure 2.9: Streamline patterns of an equal strength counter-rotating pair in the comoving frame from Leweke et al. [10]

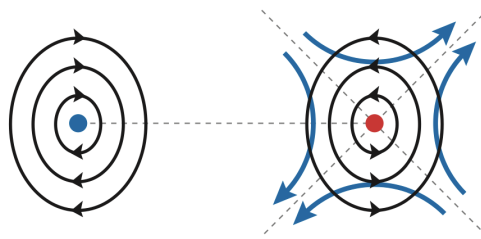


Figure 2.10: Elliptical streamlines due to the induced strain for a counter-rotating vortex pair from Leweke et al. [10]

Similarly to co-rotating vortex pairs each vortex induces a strain at the centre of the other vortex. However, the elliptical streamlines in the case of counter-rotating vortices are orientated  $45^\circ$  in the opposite direction compared to a co-rotating pair.

[10]. This can be seen by comparing Figure 2.3 to Figure 2.10. The same as co-rotating pairs, if  $\Gamma_{total} \neq 0$  for a vortex system there will be rotation of the system. For point vortex pairs with  $\Gamma_1 = -\Gamma_2$  the pair will translate along the axis of symmetry with a speed of  $U = \Gamma/(2\pi b)$  [10]. The trajectories of unbound counter-rotating pairs are shown in Figure 2.11.

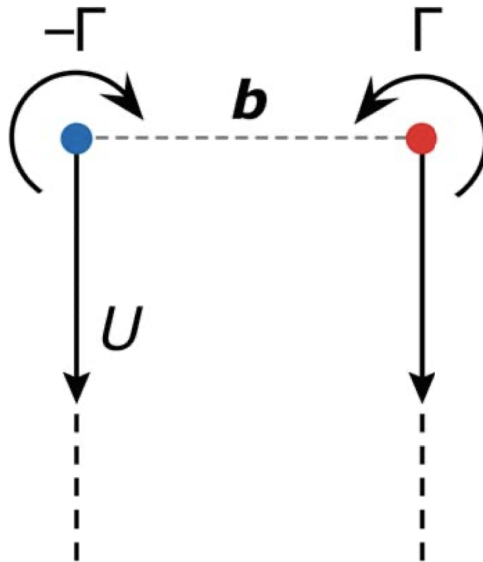


Figure 2.11: Trajectories of counter-rotating point vortex pairs from Leweke et al. [10]

A counter-rotating vortex pair in close proximity to a wall has a significantly different trajectory to that of an unbound pair. A counter-rotating vortex pair in proximity to a no-slip wall will rebound unlike a pair approaching a stress free wall, as shown in Figure 2.12. When a vortex pair approaches a wall, a boundary layer of opposite sign vorticity to the primary vortex forms. The vortex results in a low pressure region as well as a cross flow, this causes the cross flow to be subject to an adverse pressure gradient as it flows under the vortex, which causes a bubble containing the vorticity to form [25]. At the low Reynolds numbers simulated by Peace and Riley,  $\mathcal{O}(10^2)$ , separation from the wall does not occur, however, vorticity from the wall region is swept up into the main body of the flow [26]. In the experiments by Harvey and Perry and simulations by Orlandi, at larger Reynolds numbers ( $\mathcal{O}(10^5)$  and  $\mathcal{O}(10^3)$  respectively), separation of the boundary layer was observed forming a secondary vortex of opposite vorticity. This can be seen in Figure

2.13. The interaction of the secondary vortex and primary vortex induces an upwards velocity on the primary vortex, resulting in the rebound away from the wall. Multiple rebounds are possible, when secondary vortices separate from the wall and form a pair with the primary vortices, the interaction of the two primary-secondary pairs causes them to move towards the wall again. At the Reynolds numbers simulated by Orlandi, this approach of the primary vortices towards the wall again resulted in the detachment of vorticity from the wall [27].

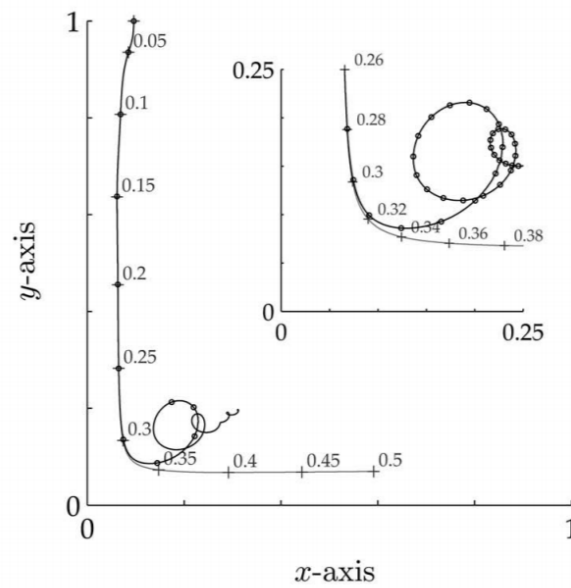


Figure 2.12: Actual (black line) and ideal (grey line) trajectories of a counter-rotating vortex pair approaching a wall from Kramer et al. [28]

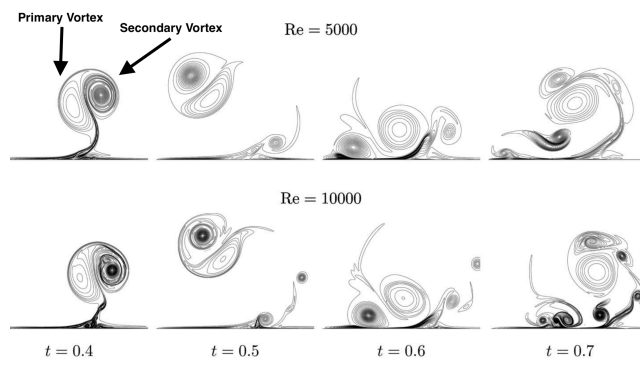


Figure 2.13: Vorticity contour plots showing the evolution of one vortex of a pair colliding with a no-slip wall. Vorticity dynamics of a dipole colliding with a no-slip wall from Kramer, Clercx and van Heijst. [28]

## 2.2.2 Instabilities

### 2.2.2.1 Crow Instability

The Crow Instability is a long wave instability with large wavelengths relative to the core size, the evolution of this can be seen in Figure 2.14 from Lweke and Williamson [29]. This was first studied by Crow [30] who undertook an analysis of a pair of equal strength counter-rotating Rankine vortices. A vortex pair subject to a sinusoidal perturbation is affected by the self induced rotation, the induced strain and rotation by the other vortex in the pair and the motion due to the perturbation. The system becomes unstable when these three rotations cancel and the perturbation plane is held at a constant angle, approximately  $45^\circ$ , where the total stretching rate is positive [10]. This can be seen in Figure 2.15. The amplitude of the displacements increases until the vortices touch and reconnection occurs. This results in the formation of vortex rings [31]. When the circulations of the pair are not equal and opposite, the rotation of the pair ( $\Omega_{Crow}$ ) has to be taken into consideration. Rather than the rotation effects summing to 0, they have to sum to  $\Omega_{Crow}$  if the perturbation plane is to remain aligned with plane where total radial stretching is positive. It was shown by Jimenez [32] that this can never be achieved for a co-rotating pair of vortices.

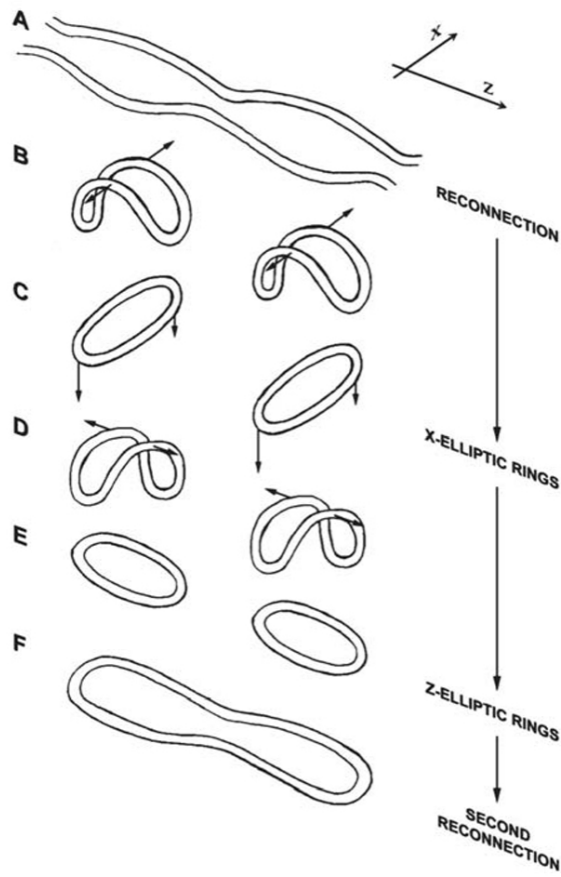


Figure 2.14: A sketch of the evolution of the Crow Instability from Lweke and Williamson. [29]

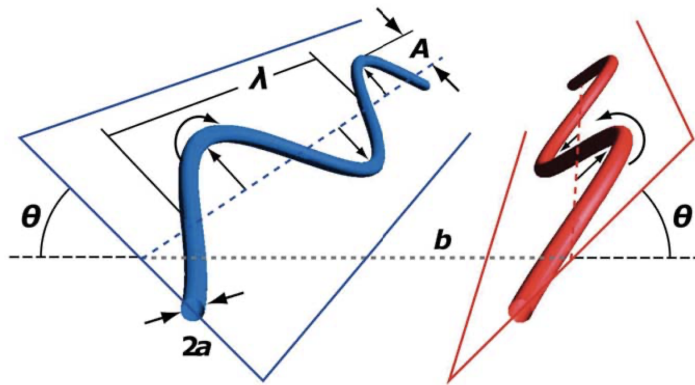


Figure 2.15: Diagram of the Crow instability from Lewke et al. [10]

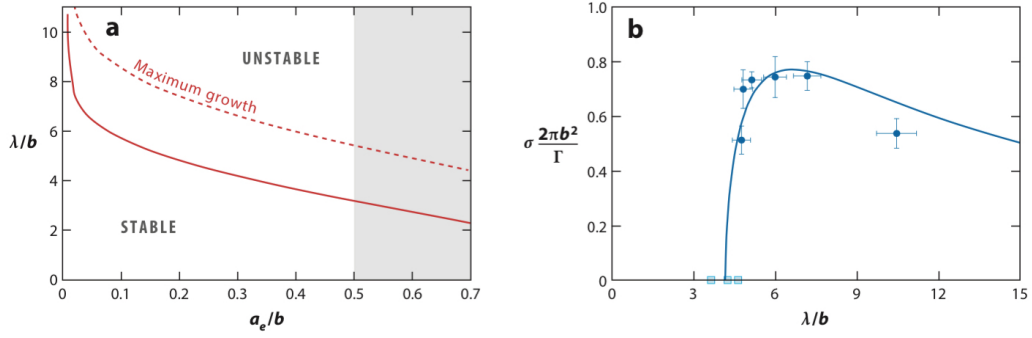


Figure 2.16: (a) The stability diagram for an equal strength counter-rotating vortex pair (The region where  $\frac{a_e}{b} > 0.5$  has no physical meaning because the cores are overlapping there) (b) The growth rate of the Crow instability as a function of normalised axial wavelength, where the symbols represent experimental measurements from Leweke et al. [10]

Widnall et al [33] further investigated this using vortex models which included axial velocities and as such better represented wing tip vortices. This was possible as the concept of equivalent core size was introduced. For a non Rankine vortex the core size equivalent to that of a Rankine vortex can be found using the following equation:  $\ln(\frac{a_e}{a}) = \frac{1}{4} - A + C$ , where  $a_e$  is the Rankine vortex core size,  $a$  is the non Rankine vortex core size and  $A$  and  $C$  depend on the vorticity distribution and axial velocity respectively ( $C=0$  for no axial velocity). Using this, Klein et al [34] and Fabre [35] showed that all co-rotating pairs are stable whilst all counter-rotating pairs are unstable with respect to the Crow mechanism. Leweke and Williamson [29] were able to build upon the work of Klein et al and Fabre, using the exact rotation rate for small-amplitude sinusoidal displacement waves on Rankine vortices to plot the stability diagram shown in Figure 2.16 (a). This was an improvement on the work of Crow [30] as it avoided the spurious short-wave instability in the stability diagrams. It can also be seen from Figure 2.16 (b) that for an equal strength pair the most unstable wavelengths are between 6 and 10 times the separation distance.

Asselin and Williamson [36] experimentally investigated the influence of a wall on a vortex pair which is unstable with respect to a long wave instability. Three modes were identified, vertical rings mode, horizontal rings mode and large rings mode. The vertical rings mode occurs for  $3 \leq \frac{h_0}{b_0} \leq 6$ , in this mode the instability is inhibited and the vortices do not reconnect into vortex rings, shown in Figures 2.17

a and b, instead collapsed vortices form, as seen in Figure 2.17 c. As the troughs interact with the wall before the peaks, vorticity is generated at the wall in those locations first. This secondary vorticity separates from the wall and wraps around the primary vortex and forms a "tongue" as shown in in Figure 2.18 a-d show the vortices in plan view and e-h show the vortices in side view. The "tongues" are transported to the peaks, by a strong pressure driven axial flow, where they rotate by self induction into a vertical orientation, shown in Figures 2.17 c, d and e. They then move towards each other and grow, forming the vertical rings. The final configuration of the primary vortices in the vertical rings mode is shown in Figures 2.17 d and h. Moving to heights of  $6 \leq \frac{h_0}{b_0} \leq 9$  horizontal vortex rings were formed. At these heights the Crow instability is able to develop further prior to wall interaction, thus the vortices have moved closer together at the troughs resulting in more vorticity cancellation than at the lower initial heights. The Crow instability is still inhibited at these heights and two collapsed vortices form per wavelength. The troughs also interact with the secondary vorticity generated at the wall, further weakening the vortices at those points, increasing the pressure. This increased pressure at the troughs drives a strong axial flow, stronger than in the vertical rings mode. The axial flow changes the topology of the primary vortex, becoming hollow vortices. The hollow vortices reconnect with the secondary vortices to form horizontal vortex rings. At values of  $\frac{h_0}{b_0}$  greater than 9 the instability grows and reaches reconnection forming vortex rings before being influenced by the wall. These vortex rings then generate secondary vorticity at the wall. Figure 2.19 shows the effect of the ground on the amplitudes of the Crow instability compared to the unbounded Crow instability.

Dehtyriov et al. [37] renamed the vertical rings mode the small amplitude mode and the horizontal rings mode the large amplitude mode. For the small amplitude mode the formation of four tongues was observed compared to the two observed by Asselin and Williamson. It was also found that reconnection of the tongues does not occur, thus vertical vortex rings were not formed. The simulation did not support the finding of horizontal rings either, instead finding the two vortex tongues formed wrapped around the primary vortices but do not result in the formation of vortex rings.

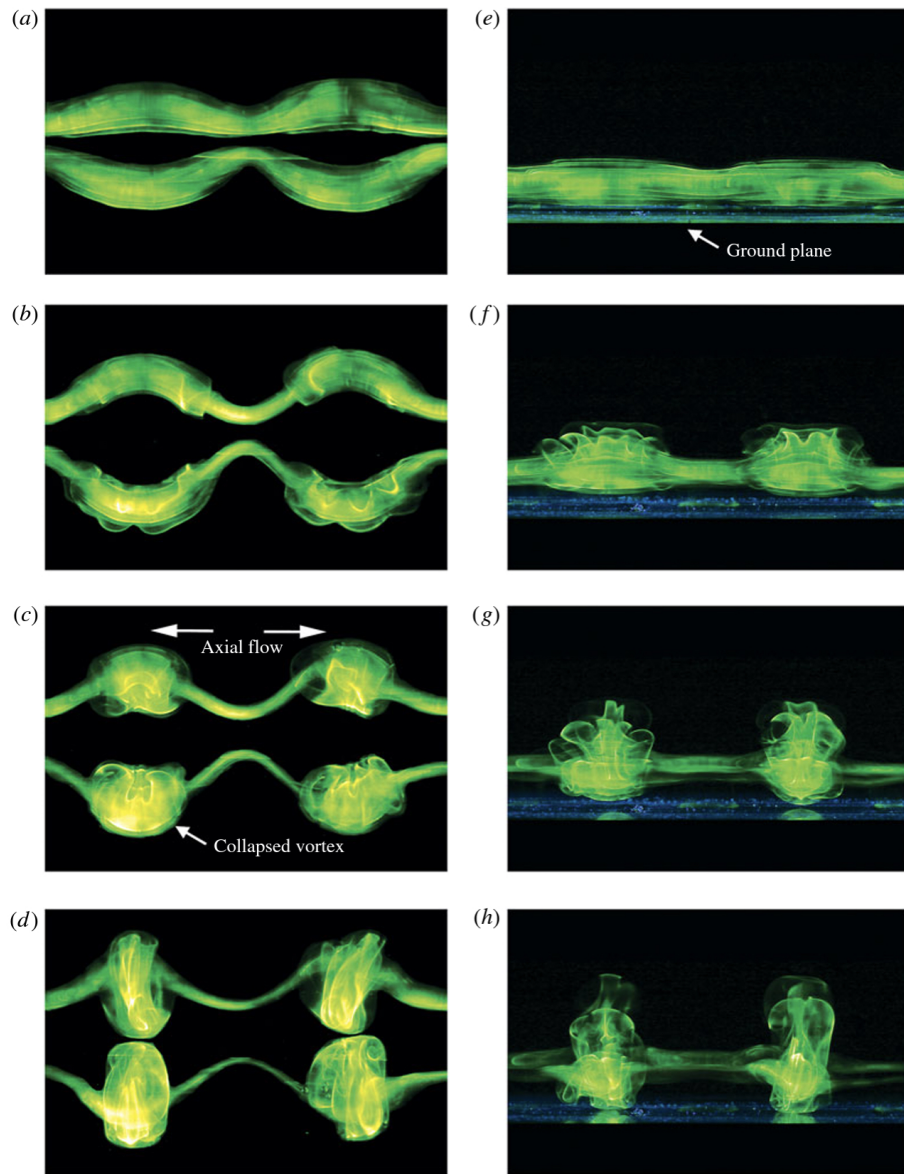


Figure 2.17: Primary vorticity for the vertical rings mode, from the experimental work of Asselin and Williamson. [36] a-d show the vortices in plan view and e-h show the vortices in side view.

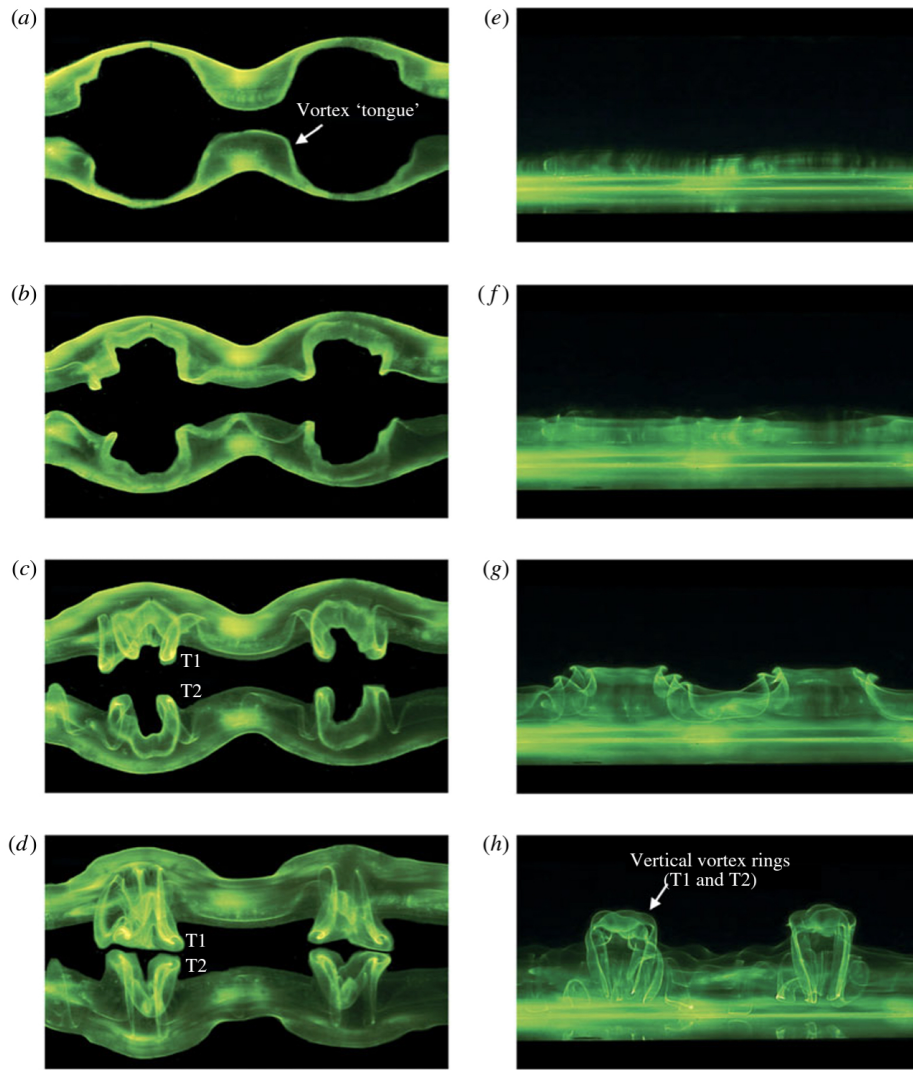


Figure 2.18: Secondary vorticity for the vertical rings mode, from the experimental work of Asselin and Williamson. [36] a-d show the vortices in plan view and e-h show the vortices in side view.

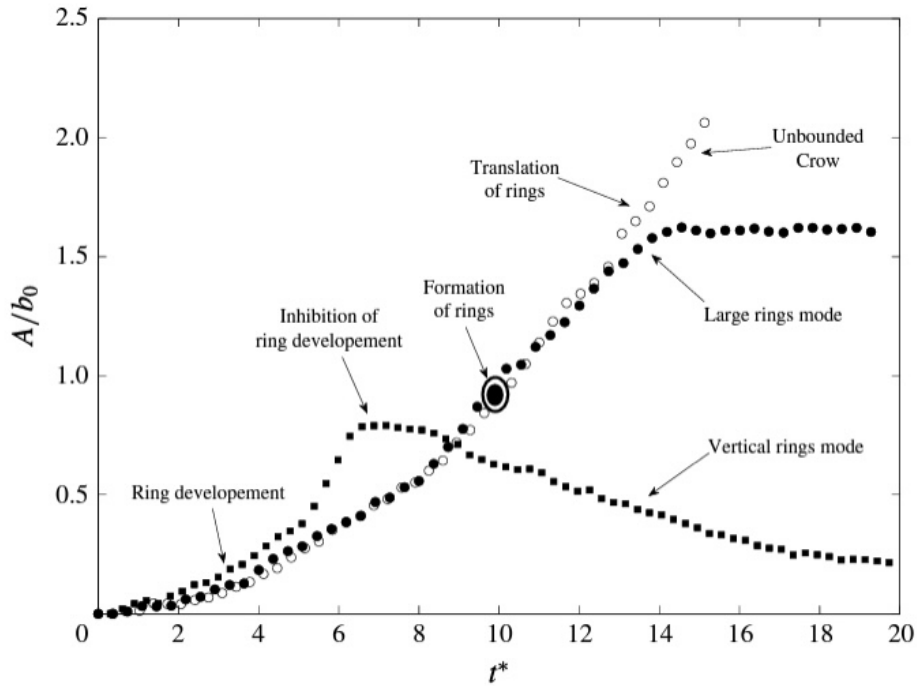


Figure 2.19: The normalised amplitudes of the unbounded, large rings mode and vertical rings mode Crow Instability from Asselin and Williamson. [36]

### 2.2.2.2 Elliptic Instability

The elliptic instability is a short wave instability which can occur in both counter-rotating and co-rotating vortices. This was first investigated and explained by Moore and Saffman [38] and Tasi and Widnall [39] which followed on from the work of Widnall [40]. The mechanism responsible for the instability is a resonance between two Kelvin waves within the vortex core, caused by the strain induced by the other vortex. The instability can be visualised for both counter and co-rotating pairs in Figure 2.20. It was shown experimentally by Leweke and Williamson [41] and Meunier and Leweke [42] that for a vortex pair without axial flow that the core deformations correspond to an instability mode of  $(m_1, m_2, n) = (-1, 1, 1)$ , where  $m_1$  and  $m_2$  are the azimuthal wave numbers and  $n$  characterises the radial complexity of the mode.

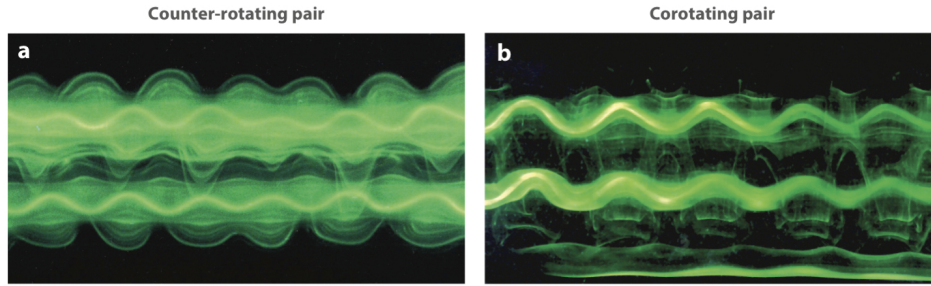


Figure 2.20: Water tank visualisation of elliptic instability: (a) For a counter-rotating pair at  $Re_\Gamma = 2750$  from Leweke and Williamson [41] (b) For a co-rotating pair at  $Re_\Gamma = 4140$  from Meunier and Leweke [42]

For vortices with axial flow, such as wing tip vortices [43], the axial flow modifies the Kelvin waves within the vortex cores. A Rankine vortex with constant axial velocity was analysed by Lacaze et al. [44] and found that the stationary symmetric Kelvin modes,  $m = 1$  and  $m = -1$ , no longer leads to a sinuous deformation. A Batchelor vortex was then analysed by Lacaze et al. [45] using the same method used by Moore and Saffman [38] and found that for small axial flow components the symmetry between the two kelvin modes is broken and there is no sinuous deformation. When the axial flow component is increased the resonance between the Kelvin modes  $m = 1$  and  $m = -1$  disappears due to damping, but a new resonance between Kelvin modes  $m = 0$  and  $m = -2$  occurs. As the axial flow component is increased the resonance mode is replaced by  $m = -1$  and  $m = -3$  and so on. Direct numerical simulations for equal strength co-rotating pairs by Roy et al. [46] and unequal strength counter-rotating pairs by Ryan et al. [47] showed that the rotation of the vortex system does not significantly change the stability characteristics however, co-rotating pairs have increased growth rates.

## Chapter 3

# Experimental Methodology

### 3.1 Wind Tunnel and Measurement Technique

Experiments were performed in the Durham 1m wind tunnel, an open return fixed ground type capable of speeds up to  $45 \text{ ms}^{-1}$  with a closed 550mm by 550mm test section. The tunnel nozzle has a contraction ratio of 7.1:1 over a length of 1.8m. A schematic of the tunnel is shown in Figure 3.1.

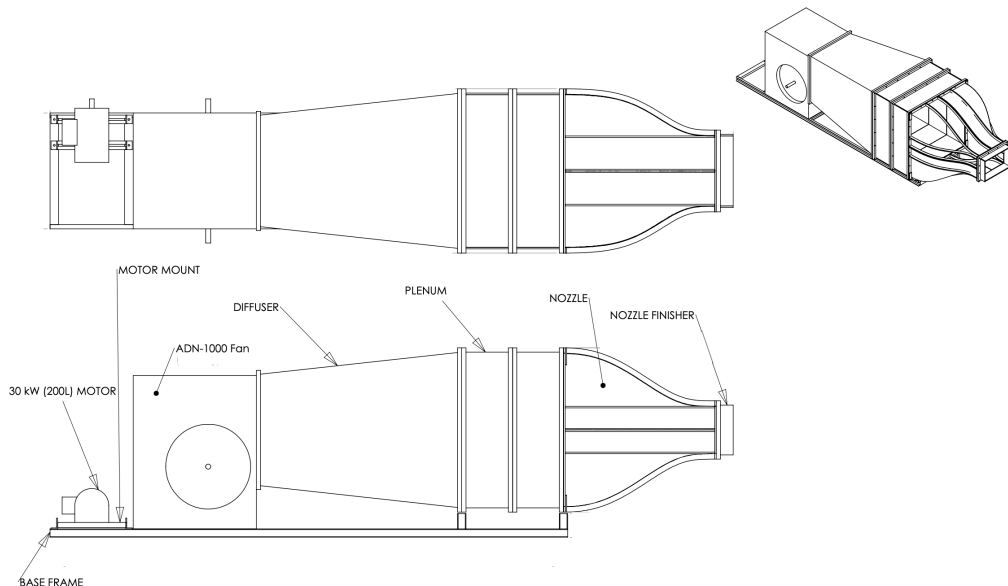


Figure 3.1: Plan, side and isometric views of the Durham 1m Wind Tunnel

Pressure measurements were taken using a five hole pneumatic probe and amplified pressure transducers connected to a NI-DAQmx data logger. The pressure transducers were calibrated by applying known pressures to each transducer, the output voltage

from the transducer was then logged and a calibration file was produced. This calibration file was then used during the processing of pressure data.

The five hole probe was designed, manufactured and calibrated. The probe tip has one hole at the centre with the other four holes positioned around, as shown in Figure 3.2. The calibration was completed using a dedicated calibration facility which consisted of a fan connected to a long diffuser and then a nozzle with a diameter of 102mm and a traverse that rotated about two axes. The probe was first aligned with the flow exiting the nozzle. The probe was inserted into the flow and measurements were taken at a small range of angles. The probe was then inverted and the process was repeated. The error in the alignment of the probe with the flow was calculated using the following equations:

$$Pitch = \sin^{-1} \left[ \frac{\left( \left( \frac{u_z}{U_\infty} \right) - \left( \frac{u_z}{U_\infty} \right)_{inverted} \right)}{2} \right] \quad (3.1)$$

$$Yaw = \sin^{-1} \left[ \frac{\left( \left( \frac{u_y}{U_\infty} \right) - \left( \frac{u_y}{U_\infty} \right)_{inverted} \right)}{2} \right]. \quad (3.2)$$

Where  $u_y$  and  $u_z$  are the horizontal and vertical components of velocity respectively and  $U_\infty$  is the freestream velocity. A non-zero angle indicates the probe is misaligned with the flow, the probe was considered aligned once the angle was less than  $0.1^\circ$ .

For the calibration the flow velocity was set to  $35ms^{-1}$ , the same as the velocity used in the wind tunnel as discussed below. This was measured using measurements of static pressure upstream and downstream of the nozzle, thus the exact velocity of the flow was known. The tip of the probe was then placed at the centre of the nozzle and calibrated between  $\pm 60^\circ$  in both pitch and yaw at  $2.5^\circ$  increments, with data logged over 5s at each orientation. Dynamic and static pressure coefficients and coefficients of yaw and pitch were calculated using the following equations:

$$C_{p_{Dyn}} = \frac{P_0 - \left( \frac{P_1 + P_2 + P_3 + P_4}{4} \right)}{P_{Dyn}}, \quad (3.3)$$

$$C_{p_0} = \frac{P_0 - P_{tot}}{P_0 - \left( \frac{P_1 + P_2 + P_3 + P_4}{4} \right)}, \quad (3.4)$$

$$C_{yaw} = \frac{P_1 - P_2}{P_0 - \left( \frac{P_1 + P_2 + P_3 + P_4}{4} \right)}, \quad (3.5)$$

$$C_{pitch} = \frac{P_3 - P_4}{P_0 - \left( \frac{P_1 + P_2 + P_3 + P_4}{4} \right)}, \quad (3.6)$$

where the subscript refers to the number hole at which the pressure was measured and  $P_{Dyn}$  is dynamic pressure. The calibration file, shown in Figure 3.3 was then produced, which relates the coefficients to the angle of the flow. It can be seen in Figure 3.3 that although the probe was calibrated between  $\pm 60^\circ$ , the probe is only sensitive to  $\pm 45^\circ$ .

During experiments measurements were taken at multiple grid points, with the probe moved using a 3 axis traverse. The angle of the local flow at a given point is then calculated using an inverse process to the creation of the calibration file. The pitch and yaw coefficients are calculated using equations 3.6 and 3.5, the angles to which these coefficients correspond to are then found from the calibration file.

The lowest the probe could be traversed was 10mm above the flat plate. Due to this and the spatial resolution of the pneumatic probe, the secondary vortices close to the plate were not resolved. The no slip condition was applied to the plate and cubic spline interpolation was then used when processing the velocity data. This allowed the velocity between the plate and  $y = 10\text{mm}$  to be interpolated. From this interpolated velocity data  $\omega_x$  was calculated using the following equation:

$$\omega_x = \frac{\partial u_z}{\partial y} = \frac{\partial u_y}{\partial z}. \quad (3.7)$$

Circulation was calculated using

$$\Gamma = \int \omega_x dS. \quad (3.8)$$

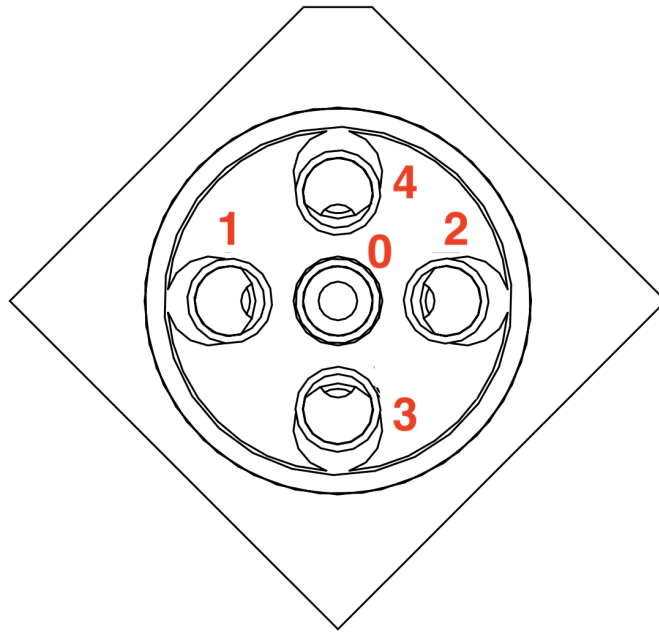
Vortex centroids are given by the integral of vorticity multiplied by displacement and divided by the circulation [10], shown below:

$$Y_c = \frac{1}{\Gamma} \int Y \omega_x dS \quad (3.9)$$

$$Z_c = \frac{1}{\Gamma} \int Z \omega_x dS \quad (3.10)$$



(a)



(b)

Figure 3.2: (a) Schematic of a five hole pneumatic pressure probe. (b) A view of the five hole probe tip, with the number of each hole shown in red.

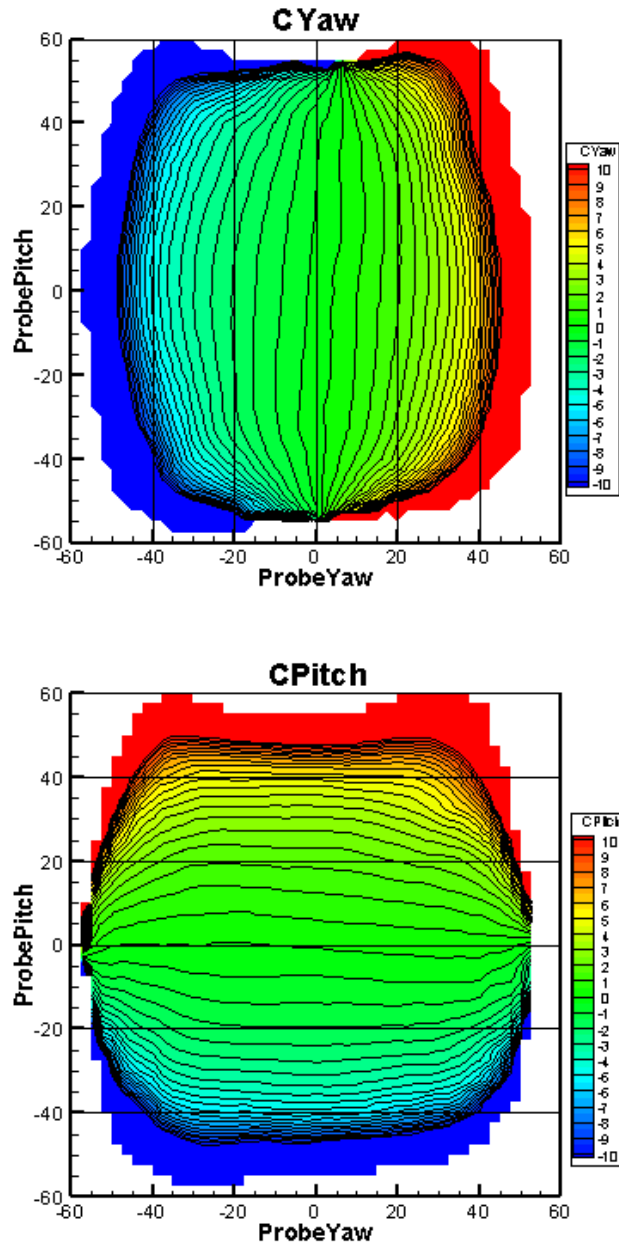


Figure 3.3: Five hole probe calibration.

## 3.2 Experimental Geometry

To generate the vortices vortex generators were used, the vortex generators are wings orientated perpendicular to the flat plate, shown in Figure 3.5, which produce trailing vortices. A NACA 0012 profile was used for the vortex generators, this was chosen as there is a large amount of existing research on it's vortices for non

interacting cases [48, 49, 50] and it's vortices for interacting cases [51, 52, 9]. It is also a symmetric aerofoil that allowed quick changes between co and counter-rotating configurations within the wind tunnel. The vortex generators were produced using additive manufacturing. Forster compared wind tunnel measurements of an aluminium NACA 0012 wing to a polylactic acid (PLA), a material commonly used for additive manufacturing, wing and found no observable differences [53]. Due to this PLA was used for the vortex generators. The vortex generators were attached to the flat plate via a bolt through the quarter chord and a tapped hole in the plate. The quarter chord was chosen as it is the aerodynamic centre and would result in no moment acting upon the vortex generator, keeping the angle of attack constant.

An angle of attack of  $10^\circ$  was chosen as it provided a balance between maximising produced circulation and being below stall angle predicted using 2-dimensional potential flow analysis (Xfoil). This angle was used for both VGs in co-rotating configuration however, for the counter-rotating configuration in order to produce two vortices with similar circulations and stagnation pressure loss, asymmetric angles of attack had to be used due to an angularity to the wind tunnel flow. In order to produce the vortices in ground effect, a low aspect ratio (span/chord) of 0.5 was used. The angle of the vortex generator was measured using a digital protractor. The wind tunnel freestream velocity was set at  $35\text{ms}^{-1}$  which gave a Reynolds number based on chord length of,  $\text{Re} = 1.17 \times 10^5$ . This was chosen as it is within the supercritical region for a NACA 0012 at  $10^\circ$  angle of attack, which was found by Huang et al [54] to be  $\text{Re} > 4.5 \times 10^4$ , therefore the vortex shedding was indicative of higher Reynolds number flows. The experimental geometry can be seen in Figures 3.4 and 3.5.

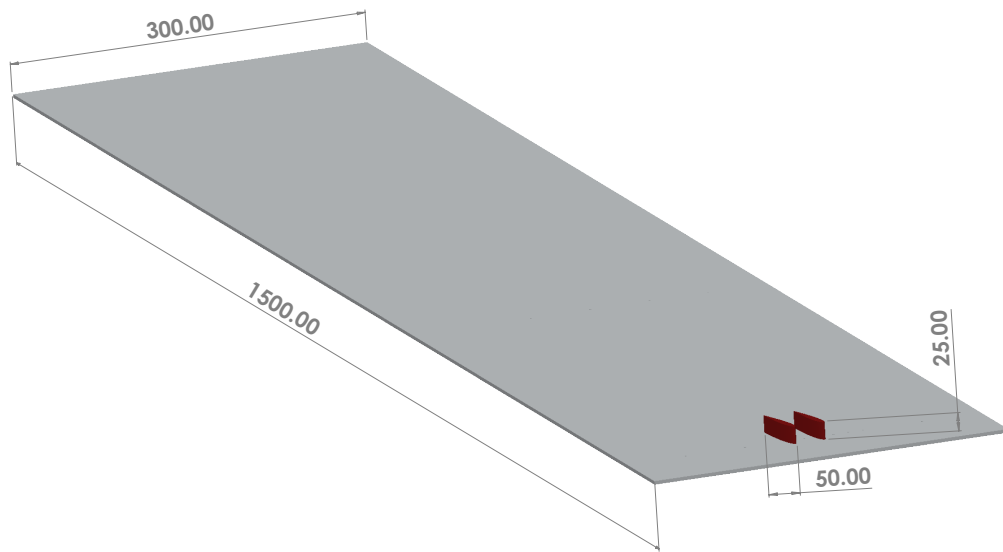


Figure 3.4: The vortex generators and flat plate experimental setup.

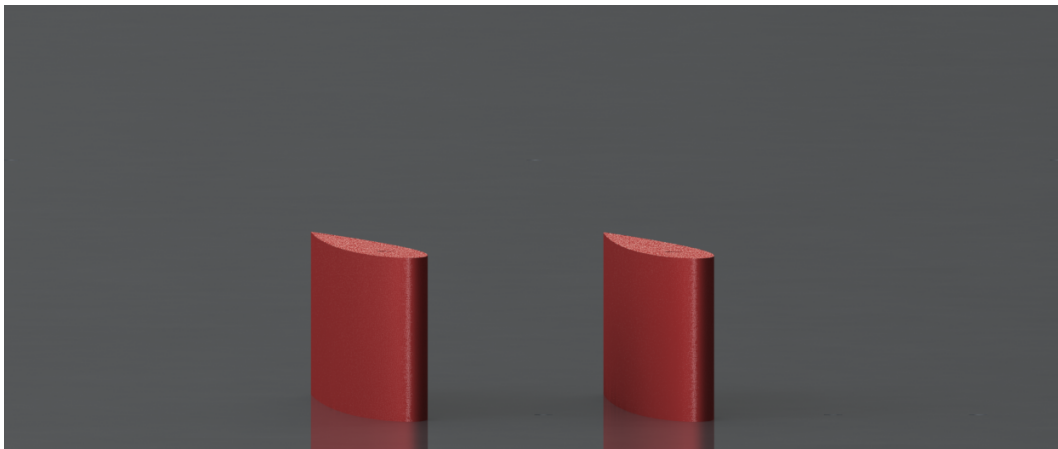


Figure 3.5: The vortex generators and flat plate experimental setup.

# Chapter 4

## CFD Methodology

Reynolds Averaged Navier Stokes (RANS) modelling was used for this research, solved using openFOAM. RANS was chosen over Large Eddy Simulations (LES) and Direct Numerical Simulations (DNS) due to the reduced computational requirements. LES and DNS resolves eddies down to grid length scale and Kolmogorov length scale respectively [55], whereas RANS describes the behaviour of eddies in the flow using a turbulence model. RANS is widely used for vortex flows in industry [56] and has also been used in the research of vortex interactions [57, 58, 59, 60].

As the flow is at a Mach number of  $M \approx 0.1$  the flow is assumed to be incompressible, as a result only the governing equations ensuring the conservation of mass and momentum need to be considered [55]. As the flow is assumed to be incompressible the density,  $\rho$ , is constant the continuity equation is the following:

$$\nabla \cdot \vec{U} = \frac{\partial u}{\partial x} + \frac{\partial v}{\partial y} + \frac{\partial w}{\partial z} = 0 \quad (4.1)$$

where  $\vec{U}$  is the velocity vector and  $u$ ,  $v$  and  $w$  are the  $x$ ,  $y$  and  $z$  velocity components respectively.

### 4.1 Turbulence Modelling

#### 4.1.1 Reynolds Averaged Navier-Stokes Equations

At the Reynolds number of the flow in this investigation turbulent flow structures are expected. In order to represent the effects of turbulence Reynolds averaging is used, the flow variables are decomposed into mean and fluctuating components:

$$u = U + u', v = V + v', w = W + w', p = P + p' \quad (4.2)$$

Substituting the velocity and pressure terms described in Equation 4.2 into the Navier-Stokes equations and taking the time average gives the Reynolds Averaged Navier-Stokes equations:

$$\nabla \cdot \vec{U} = 0 \quad (4.3)$$

$$\frac{\partial U}{\partial t} + \nabla \cdot U\vec{U} = -\frac{1}{\rho} \frac{\partial p}{\partial x} + \mu \nabla \cdot (\nabla U) - \frac{1}{\rho} \left[ \frac{\partial(\overline{\rho u'^2})}{\partial x} + \frac{\partial(\overline{\rho u'v'})}{\partial y} + \frac{\partial(\overline{\rho u'w'})}{\partial z} \right] \quad (4.4)$$

$$\frac{\partial V}{\partial t} + \nabla \cdot V\vec{U} = -\frac{1}{\rho} \frac{\partial p}{\partial y} + \mu \nabla \cdot (\nabla V) - \frac{1}{\rho} \left[ \frac{\partial(\overline{\rho u'v'})}{\partial x} + \frac{\partial(\overline{\rho v'^2})}{\partial y} + \frac{\partial(\overline{\rho v'w'})}{\partial z} \right] \quad (4.5)$$

$$\frac{\partial W}{\partial t} + \nabla \cdot W\vec{U} = -\frac{1}{\rho} \frac{\partial p}{\partial z} + \mu \nabla \cdot (\nabla W) - \frac{1}{\rho} \left[ \frac{\partial(\overline{\rho u'w'})}{\partial x} + \frac{\partial(\overline{\rho v'w'})}{\partial y} + \frac{\partial(\overline{\rho w'^2})}{\partial z} \right] \quad (4.6)$$

where  $\mu$  is dynamic viscosity.

This process introduces additional terms, the Reynolds stresses, which are associated with convective momentum transfer due to turbulent eddies within the flow. Due to these additional terms the RANS equations can not be solved without closure being provided. This is achieved by the use of the Boussinesq approximation which relates the Reynolds stresses to the mean velocity gradients:

$$-\overline{\rho u'_i u'_j} = \mu_t \left( \frac{\partial U_i}{\partial x_j} + \frac{\partial U_j}{\partial x_i} \right) - \frac{2}{3} \rho k \delta_{ij}, \quad (4.7)$$

where  $\delta_{ij}$  is the Kronecker delta.

#### 4.1.2 Turbulence Model

The k- $\omega$  shear stress transport (k- $\omega$  SST) turbulence model was chosen for this study as it is a hybrid model between the k- $\epsilon$  and k- $\omega$  models. As such it combines the k- $\epsilon$  models low sensitivity to assumed freestream conditions and the k- $\omega$  models improved performance for boundary layers subject to adverse pressure gradients compared to the k- $\epsilon$  model. [61] Furthermore, in the experimental and numerical investigations of a vortex in wall effect of Wibowo et al [62] the k- $\omega$  model performed well when compared to the experiments and was the best of the RANS turbulence models.

The standard k- $\epsilon$  model is a two equation model and solves for turbulent kinetic energy (k) and turbulence dissipation rate ( $\epsilon$ ) by introducing the following transport

equations:

$$\frac{\partial(\rho k)}{\partial t} + \nabla \cdot (\rho k \vec{U}) = \nabla \cdot \left[ \frac{\mu_t}{\sigma_k} \nabla k \right] + 2\mu_t S_{ij} \cdot S_{ij} - \rho \epsilon \quad (4.8)$$

$$\frac{\partial(\rho \epsilon)}{\partial t} + \nabla \cdot (\rho \epsilon \vec{U}) = \nabla \cdot \left[ \frac{\mu_t}{\sigma_\epsilon} \nabla \epsilon \right] + C_{1\epsilon} \frac{\epsilon}{k} 2\mu_t S_{ij} \cdot S_{ij} - C_{2\epsilon} \rho \frac{\epsilon^2}{k} \quad (4.9)$$

where  $S_{ij}$  is the strain rate tensor,  $\mu_t$  is turbulent viscosity and  $\sigma_\epsilon$ ,  $\sigma_k$ ,  $C_{1\epsilon}$  and  $C_{2\epsilon}$  are constants.

The standard k- $\omega$  model [63] uses turbulent kinetic energy and specific turbulence dissipation rate ( $\omega$ ) to solve for  $\mu_t$  by using the relation  $\mu_t = \frac{\rho k}{\omega}$  and introducing the following transport equations:

$$\frac{\partial(\rho k)}{\partial t} + \nabla \cdot (\rho k \vec{U}) = \nabla \cdot \left[ \left( \mu + \frac{\mu_t}{\sigma_k} \right) \nabla k \right] + (2\mu_t S_{ij} \cdot S_{ij} - \frac{2}{3} \rho k \frac{\partial U_i}{\partial x_j} \delta_{ij}) - \beta^* \rho k \omega \quad (4.10)$$

$$\frac{\partial(\rho \omega)}{\partial t} + \nabla \cdot (\rho \omega \vec{U}) = \nabla \cdot \left[ \left( \mu + \frac{\mu_t}{\sigma_\omega} \right) \nabla \omega \right] + \gamma_1 (2\rho S_{ij} \cdot S_{ij} - \frac{2}{3} \rho \omega \frac{\partial U_i}{\partial x_j} \delta_{ij}) - \beta_1 \rho \omega^2 \quad (4.11)$$

where  $\delta_{ij}$  is the kronecker delta and  $\sigma_\omega$ ,  $\beta^*$ ,  $\gamma_1$  and  $\beta_1$  are constants.

For the hybrid k- $\omega$  model, equation 4.9 is transformed into an  $\omega$  transport equation by substituting  $\epsilon = k\omega$ . The model received minor updates in 2003 which is the version implemented by OpenFOAM. The k- $\omega$  SST transport equations are:

$$\frac{\partial(\rho k)}{\partial t} + \frac{\partial(\rho U_i k)}{\partial x_i} = P_k - \beta^* k \omega + \frac{\partial}{\partial x_i} \left[ \left( \mu + \sigma_k \mu_t \right) \frac{k}{x_i} \right] \quad (4.12)$$

$$\frac{\partial(\rho \omega)}{\partial t} + \frac{\partial(\rho U_i \omega)}{\partial x_i} = \alpha \rho S^2 - \beta \rho \omega^2 + \frac{\partial}{\partial x_i} \left[ \left( \mu + \sigma_\omega \mu_t \right) \frac{\partial \omega}{\partial x_i} \right] + 2(1 - F_1) \rho \sigma_{\omega,2} \frac{1}{\omega} \frac{\partial k}{\partial x_i} \frac{\partial \omega}{\partial x_i} \quad (4.13)$$

Where  $F_1$  is the blending function described by the hyperbolic tangent function:

$$F_1 = \tanh \left\{ \left\{ \min \left[ \max \left( \frac{k^{0.5}}{\beta^* \omega d}, \frac{500\nu}{d^2 \omega} \right), \frac{4\rho \sigma_{\omega,2} k}{CD_{kw} d^2} \right] \right\}^4 \right\} \quad (4.14)$$

with  $CD_{kw} = \max(2\rho \sigma_{\omega,2} \frac{1}{\omega} \frac{\partial k}{\partial x_i} \frac{\partial \omega}{\partial x_i}, 10^{10})$  and  $d$  is the distance of the cell centroid to the nearest wall. The blending function,  $F_1$ , is defined in such a way that it is equal to 0 at the wall and tends to 1 away from the wall, providing a smooth transition between the  $k - \omega$  and  $k - \epsilon$  models. [64]  $\beta$  and  $\alpha$  are constants and  $\nu$  is kinematic viscosity.

In order to improve the performance of the model over the standard k- $\omega$  model for flows with adverse pressure gradients or wake regions the eddy viscosity is limited and to prevent the build up of turbulence in stagnation regions turbulent kinetic energy production is limited. The two quantities are limited by the following limiters:

$$\mu_t = \frac{a_1 \rho k}{\max(\alpha_1 \omega, SF_2)} \quad (4.15)$$

$$P_k = \min[\mu_t \frac{\partial U_i}{\partial x_j} (\frac{\partial U_i}{\partial x_j} + \frac{\partial U_j}{\partial x_i}), 10\beta^* \rho k \omega] \quad (4.16)$$

where  $\alpha_1$  is a constant and  $F_2$  is another blending function,  $F_2 = \tanh \left[ \left[ \max\left(\frac{2\sqrt{k}}{\beta\omega d}, \frac{500\nu}{d^2\omega}\right) \right]^2 \right]$ , and  $S = \sqrt{2S_{ij}S_{ij}}$ . [64]

## 4.2 Numerical Procedure

OpenFOAM uses the finite volume method which is widely used in CFD codes. First, the conservation equations are transformed to integral form and the solution domain is subdivided into a finite number of control volumes. The centroid of each volume is where the values are computed. To calculate the values of the variables on the faces of the volumes the RANS equations need to be discretised.

### 4.2.1 Discretisation

In order to calculate the values at the control volume faces from the data calculated at the centre discretisation techniques are used. Central differencing was used to discretise the diffusion term. Central differencing uses linear interpolation to obtain values at the faces and is a second order accurate scheme. For the convection terms the linear upwind scheme was chosen, it was chosen over central differencing as it possesses greater stability and transportiveness and considers the flow direction. As a result, central differencing schemes are better suited to flows with lower velocity than is used in the simulations in this research. Upwind differencing assumes a constant value of the flow properties between the face and the upstream volume centre (node) and is first order accurate which results in artificial diffusion. [55, 65] The linear upwind scheme was used by Wibowo et al. [62] for experimentally validated simulations of a vortex over a delta wing.

### 4.2.2 Solution Algorithm

A pressure based solver using the SIMPLE algorithm was used for all simulations presented in this thesis. The SIMPLE acronym stands for Semi-Implicit Method for Pressure Linked Equations, initially proposed by Patankar and Spalding [55]. The algorithm gives a method of solving for pressure and velocities iteratively starting from an initial guess. The SIMPLE algorithm is shown in Figure 4.1.

The momentum equations are solved followed by the pressure correction equation, which couples the pressure and velocities. Following the solving of the pressure correction equation the corrections are applied to the pressures and velocities. The turbulence quantities are then calculated. The initial guesses are updated with the newly calculated values, this process is iterated until convergence is reached. [55]

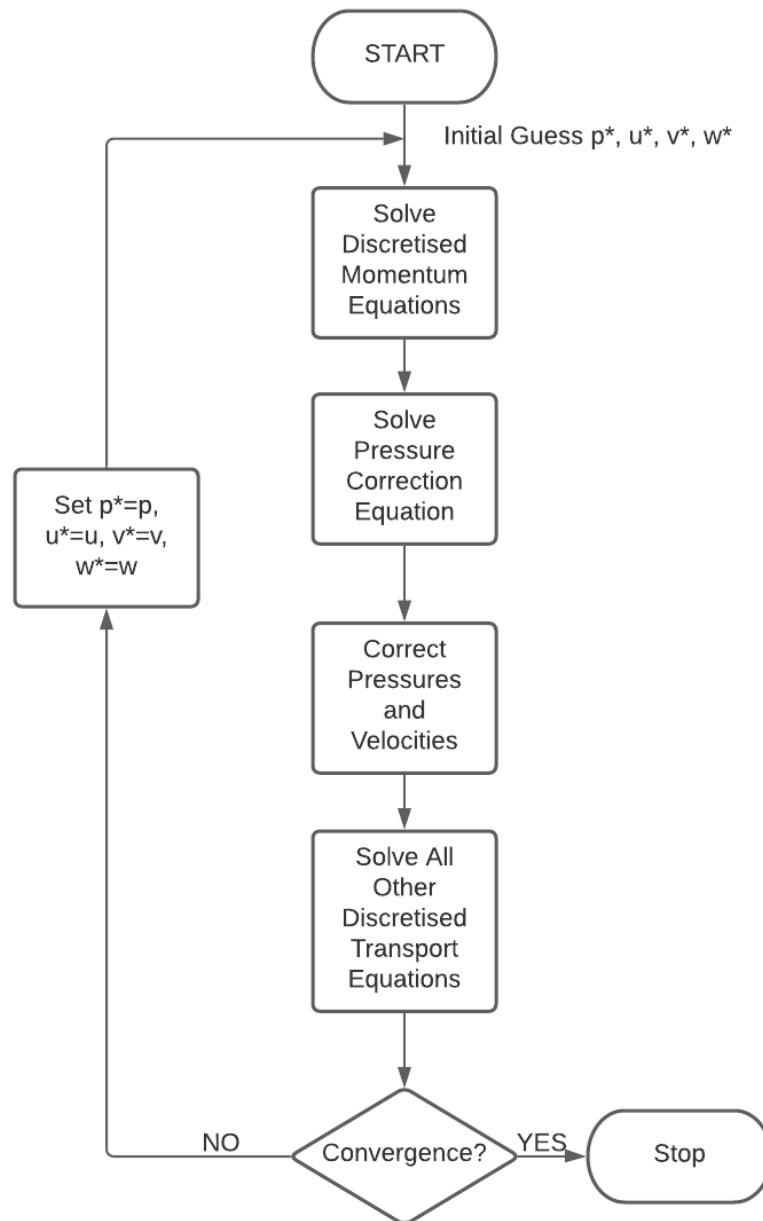


Figure 4.1: The SIMPLE algorithm

### 4.2.3 Convergence Criteria

The solution was considered converged when the residuals were steady and equal to or less than  $10^{-5}$  as well as the variation in lift force over the previous 500 iterations to be 1% or less. For all simulations conducted this took between 2000 and 3000 iterations.

## 4.3 Computational Domain

### 4.3.1 Boundary Conditions

A velocity inlet and pressure outlet were used, with the sides and top of the domain modelled as walls with zero shear and the no slip condition applied to the bottom of the domain (plate). The boundary layer was fully resolved, so the following boundary conditions were used for the plate, the omega wall function was used for omega, which sets the omega boundary condition to that recommended by Menter [66] and a fixed value of 0 was used for  $k$  and  $\mu_t$ . [67] Inlet and initial turbulence model boundary conditions were calculated from turbulence intensity, which was set to 1% and a length scale given by  $l = 0.07H$ , where  $H$  is the height of the inlet, as recommended by Versteeg and Malalasekera [55]. The computational domain and boundary conditions are shown schematically in Figure 4.2

The inlet velocity was given by the superposition of two Batchelor vortices, a vortex profile that was initially proposed by Batchelor in 1964 [68]. This vortex model was chosen as it has been successfully used in many times for similar problems [42, 69, 70, 71, 72, 73, 74, 75, 76] and it includes a velocity deficit in the core like in a tip vortex. The velocity distribution in cylindrical coordinates for the Batchelor vortex is given by:

$$u_r = 0, u_\theta = \frac{\Gamma_0}{2\pi r}(1 - e^{-r^2/a_0^2}), u_z = W_0 e^{-r^2/a_0^2} \quad (4.17)$$

where  $a_0$  is the initial core size,  $\Gamma_0$  is the initial circulation,  $r$  is the distance from the centre and  $W_0$  is the maximum axial velocity in the vortex centre and thus controls the velocity deficit in the core. The velocity was then converted to Cartesian coordinates to be used as the inlet boundary condition. The streamwise vorticity is given by:

$$\omega_x = \frac{\Gamma}{\pi a_0^2} e^{-r^2/a_0^2}. \quad (4.18)$$

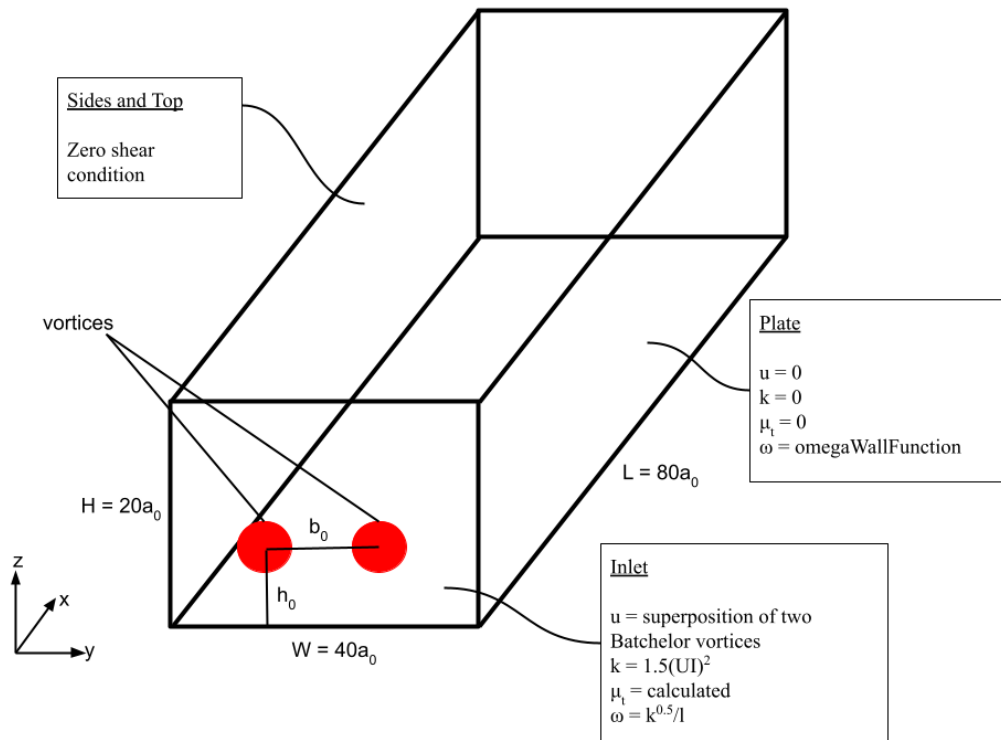


Figure 4.2: The computational domain and boundary conditions.

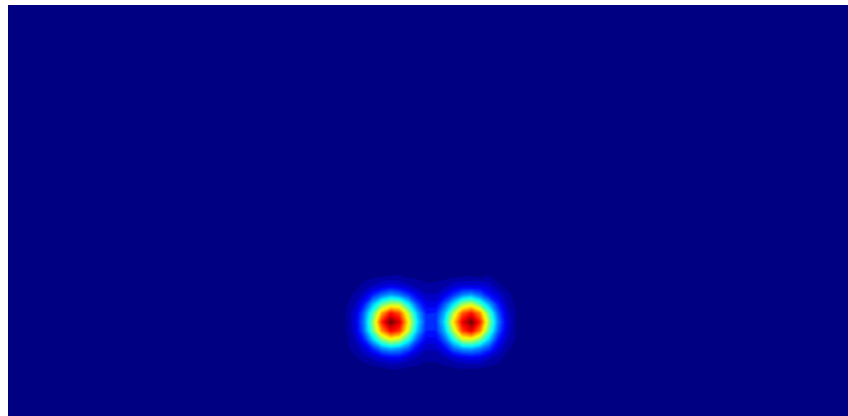


Figure 4.3: The superposition of two Batchelor vortices.

### 4.3.2 Mesh

To determine the solution obtained was mesh independent meshes of increasing density were tested. The mesh was varied so that the cell aspect ratios were maintained as the mesh densities increased. The variations in vortex circulation and centroids at multiple planes downstream of the inlet compared to the finest

mesh were obtained. This process indicated that the circulation for the mesh with  $2 \times 10^7$  control volumes varied by less than 0.5% for every position tested, as shown in Figure 4.4. It also showed that the position of the vortex centroid overlaps for the two planes closest to the inlet and by  $0.3a_0$  for the most downstream plane, as can be seen in Figure 4.5. The variation in vortex centroid was computed by calculating the distance of the centroid from the position of the centroid in the most fine mesh, non-dimensionalised by  $a_0$ .

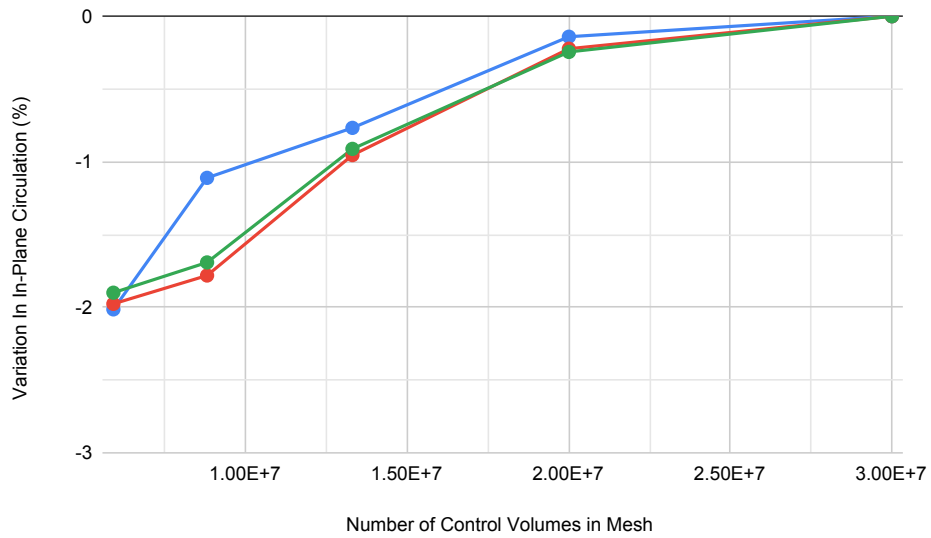


Figure 4.4: Variation in vortex circulation in the planes  $x = 20a_0$  (blue),  $x = 40a_0$  (red) and  $x = 60a_0$  (green) due to changes in mesh density.

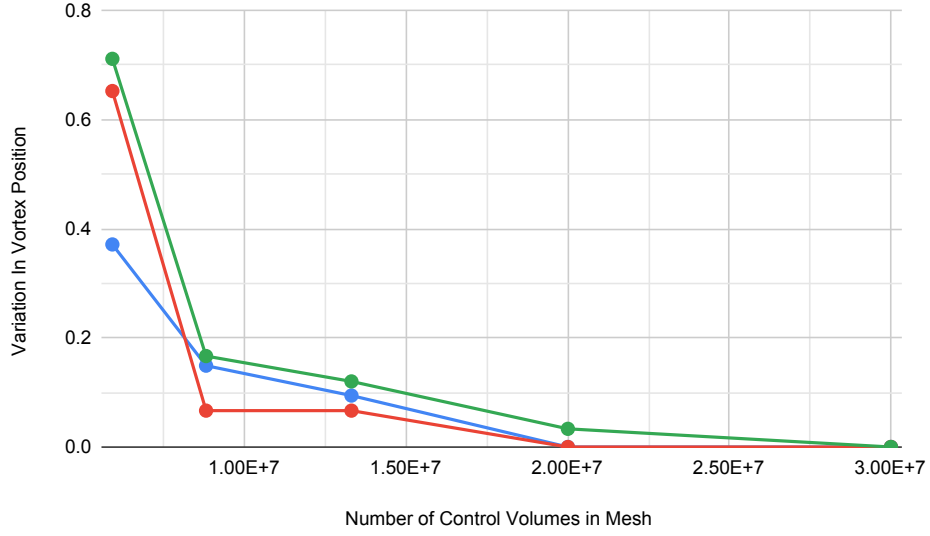


Figure 4.5: Variation in vortex centroid in the planes  $x = 20a_0$  (blue),  $x = 40a_0$  (red) and  $x = 60a_0$  (green) due to changes in mesh density.

To estimate the error associated with using the  $2 \times 10^7$  mesh rather than the more dense mesh the grid convergence indicator ( $GCI$ ) was calculated. The  $GCI$  was proposed by Roach [77] and is calculated using the following equation:

$$GCI = \frac{F_s r_{CGI}^O |\zeta|}{(r_{CGI}^O - 1)}, \zeta = \frac{f_{coarse} - f_{fine}}{f_{coarse}}, r_{CGI} = \frac{h_{coarse}}{h_{fine}}, \quad (4.19)$$

where  $F_s$  is the safety factor,  $h_{fine}$  and  $h_{coarse}$  are the characteristic lengths for the meshes,  $f_{fine}$  and  $f_{coarse}$  are the quantities which the  $GCI$  is being calculated and  $O$  is the order of the numerical scheme. A factor of safety of 3 is used. [55] The  $GCI$  values are shown in Table 4.1.

Plane	GCI for circulation
$\frac{x}{a_0} = 20$	0.864%
$\frac{x}{a_0} = 40$	1.37%
$\frac{x}{a_0} = 60$	1.50%

Table 4.1: The  $GCI$  for circulation.

To ensure the distance to the sides and top of the domain did not affect the results 3 different domain heights ( $10a_0$ ,  $20a_0$  and  $40a_0$ ) and widths ( $20a_0$ ,  $40a_0$  and  $80a_0$ ) were tested. The different widths were tested for the a co-rotating pair at the

lowest height above the ground, as this was expected to move laterally the most, therefore most likely to be affected by the domain walls. The varying domain heights were tested with the co-rotating pair at the highest initial height above the ground. The vortex pair circulation was then compared to the largest domain, as shown in Tables 4.2 and 4.3, from this it was found that there was -0.0027% and -0.0023% change for the  $40a_0$  width and  $20a_0$  height domains respectively. The mesh density was held constant as the domain size was varied.

Domain Width	Percentage Variation
$20a_0$	-6.42
$40a_0$	-0.027
$80a_0$	0

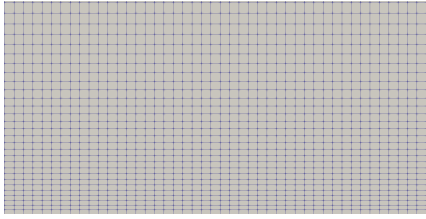
Table 4.2: Variation in vortex pair circulation at  $x = 80a_0$  for differing domain widths compared to the widest domain tested.

Domain Height	Percentage Variation
$10a_0$	-1.79
$20a_0$	-0.0023
$40a_0$	0

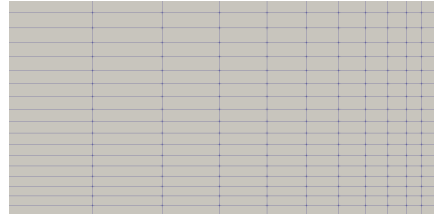
Table 4.3: Variation in vortex pair circulation at  $x = 80a_0$  for differing domain heights compared to the largest domain tested.

A structured mesh was used throughout this investigation, with grading employed so that the vortex cores and near wall flows are accurately captured whilst keeping the computational expense at a practical level. To accurately represent the near wall flow a dimensionless wall distance,  $y^+$ , must be less than 5 to place the centre of the first layer of cells within the viscous sublayer. [55, 78] The  $y^+$  was held as close to 1 as possible across the bottom of the domain, with a maximum value of 1.4. The mesh also maintained 28 cells across the vortex core, more than the minimum of 15 recommended by Dacles-Mariani et al. [79] to correctly capture the vortex core. The cell aspect ratio was kept close to 1 in the regions of the mesh containing the vortices. However, large aspect ratios do exist within the mesh but are kept to regions far from the vortices to limit the impact on the investigation. These mesh

regions can be seen in Figure 4.6.



(a)



(b)

Figure 4.6: (a) The mesh in the region containing the vortices and (b) the mesh region near the edges of the domain, away from the vortices.

# Chapter 5

## Results

Experiments were undertaken for vortex pairs at multiple separations, using two NACA0012 vortex generators to produce the vortex pair, at a Reynolds number based on vortex generator chord length,  $Re = 1.17 \times 10^5$ , as stated in Chapter 3. Further wind tunnel experiments, as well as water tunnel experiments utilising particle image velocimetry were initially planned. However, due to the Covid-19 pandemic it was not possible to complete further experimental work, as a result numerical investigations were completed. Numerical simulations, using RANS modelling, were completed for both co-rotating and counter-rotating vortex pairs at varying initial separations and heights above the ground plane. For all simulations the Reynolds number based upon circulation,  $Re_\Gamma \approx 5 \times 10^4$ . This was chosen as it is similar to the Reynolds numbers of the tip vortices found in van den Berg's investigations [80] of an inverted race car wing in ground effect. It is also approximately 35 times larger than the  $Re_\Gamma$  used by Wang et al. [9], allowing vortex merging in ground effect to be investigated at a Reynolds number closer to that observed in real world flows.

The numerical simulations did not aim to replicate the experimental setup. As the  $Re_\Gamma$  was limited for the experimental work, due to wind tunnel speed and VG geometry, the simulations presented an opportunity to investigate the vortex interactions at a higher  $Re_\Gamma$ . However, this meant that no quantitative comparison could be made between numerical and experimental work. Quantitative comparisons were still possible and an insight into vortex interactions at different  $Re_\Gamma$  can be gained.

Case	$\frac{a_0}{b_0}$	$\frac{h_0}{a_0}$	Type
Experimental Co-Rotating 1	0.12	1.73	Experiment
Experimental Co-Rotating 2	0.32	1.73	Experiment
Co-Rotating 1	0.1	1.67	CFD
Co-Rotating 2	0.2	1.67	CFD
Co-Rotating 3	0.3	1.67	CFD
Co-Rotating 4	0.4	1.67	CFD
Co-Rotating 5	0.5	1.67	CFD
Co-Rotating 6	0.2	5	CFD
Co-Rotating 7	0.2	7.5	CFD
Co-Rotating 8	0.2	10	CFD
Co-Rotating 9	0.3	3.33	CFD
Co-Rotating 10	0.3	5	CFD
Co-Rotating 11	0.3	6.67	CFD
Counter-Rotating 1	0.1	1.67	CFD
Counter-Rotating 2	0.2	1.67	CFD
Counter-Rotating 3	0.3	1.67	CFD
Counter-Rotating 4	0.4	1.67	CFD
Counter-Rotating 5	0.5	1.67	CFD

Table 5.1: List of Cases

## 5.1 Co-Rotating Results

### 5.1.0.1 Experimental Co-Rotating Case 1

Experimental Co-Rotating Case 1 is an investigation of a co-rotating vortex pair at an initial spacing of  $\frac{a_0}{b_0} = 0.12$  and an initial height of  $\frac{h_0}{a_0} = 1.73$ . This is most similar to the spacing and height to that of Co-Rotating Case 1. The first measurement plane was 50mm (1 chord length, C) downstream of the vortex generators.

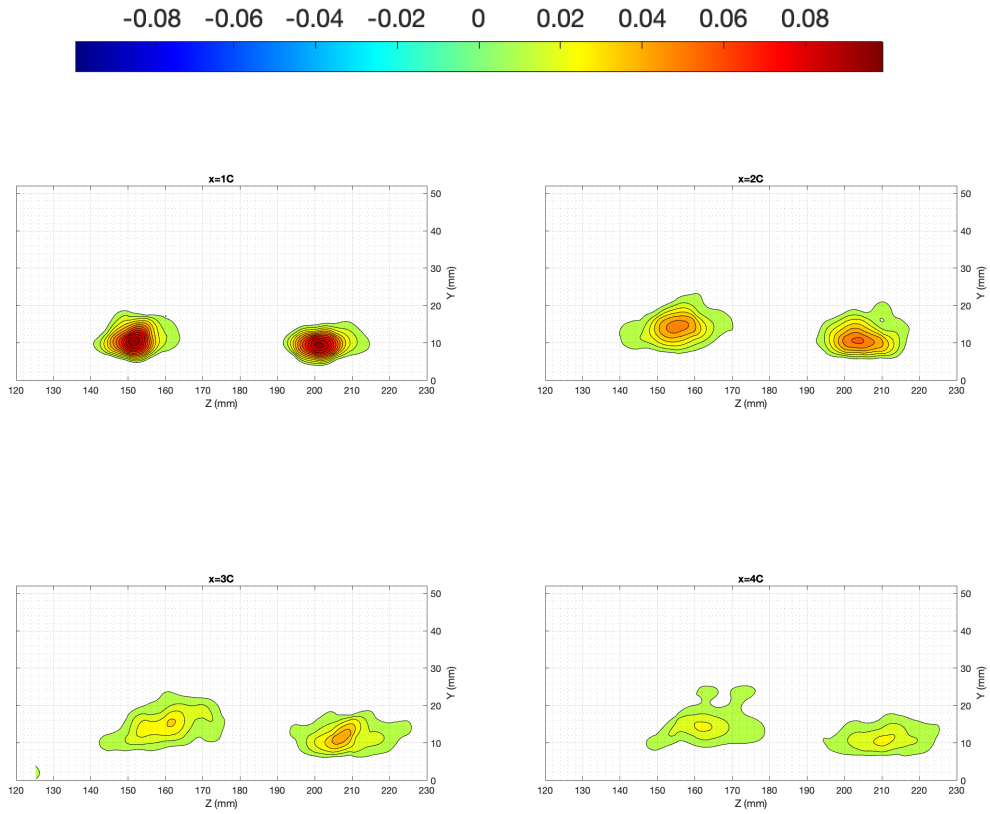


Figure 5.1: Contours of  $\omega_x$  for Experimental Co-Rotating Case 1.

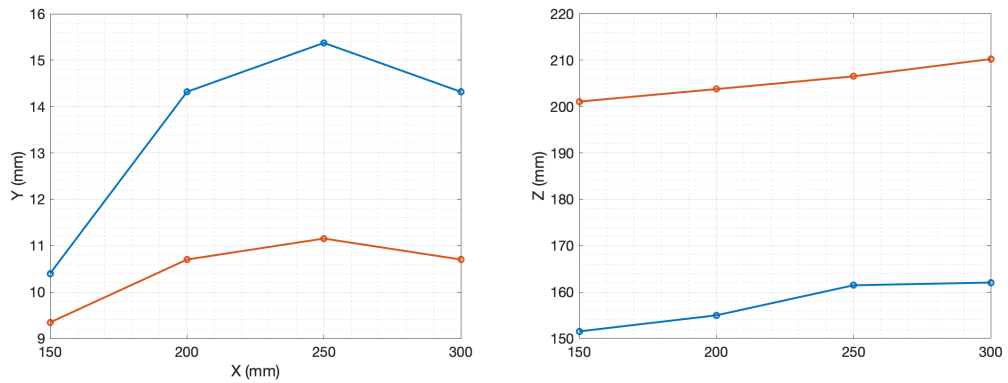


Figure 5.2: Vortex centroids for Experimental Co-Rotating Case 1.

At the first measurement plane, shown in Figure 5.1, the vortices had not started to rotate about each other. Moving downstream to the next plane the vortices had shifted laterally due to the induced velocity and started to stretch in the direction of the line between their centres. At  $x = 4C$ , a filament, similar to that seen in the

simulations, formed on the left vortex. In the plots of vortex core paths of Figure 5.2, it can be seen that the vortices shift laterally an almost equal amount, with the left and right vortices moving by 9.2mm and 10.5mm respectively between the first and last measurement planes. Rebound is also observed, as the left vortex moved upwards by 3.92mm and the right by 1.36mm between  $x = 1C$  and  $x = 4C$ . That discrepancy can be explained by the rotation of the pair, as the right vortex starts to move under the left. Although, there is only a small change in orientation angle of the pair, consistent with the simulations.

### 5.1.0.2 Experimental Co-Rotating Case 2

Experimental Co-Rotating Case 2 is the experimental case with the widest spacing, at an initial spacing of  $\frac{a_0}{b_0} = 0.32$  and an initial height of  $\frac{h_0}{a_0} = 1.73$ . This is most similar to the spacing and height to that of Co-Rotating Cases 3. The first measurement plane was 50mm (1 chord length) downstream of the vortex generators.

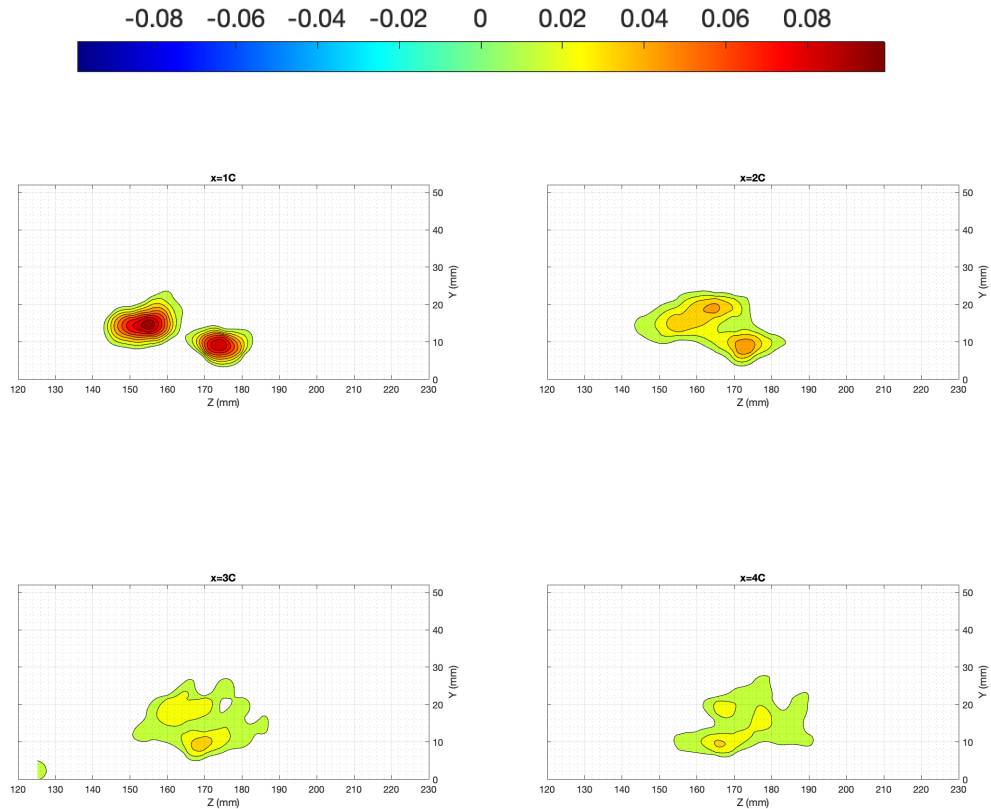


Figure 5.3: Contours of  $\omega_x$  for Experimental Co-Rotating Case 2.

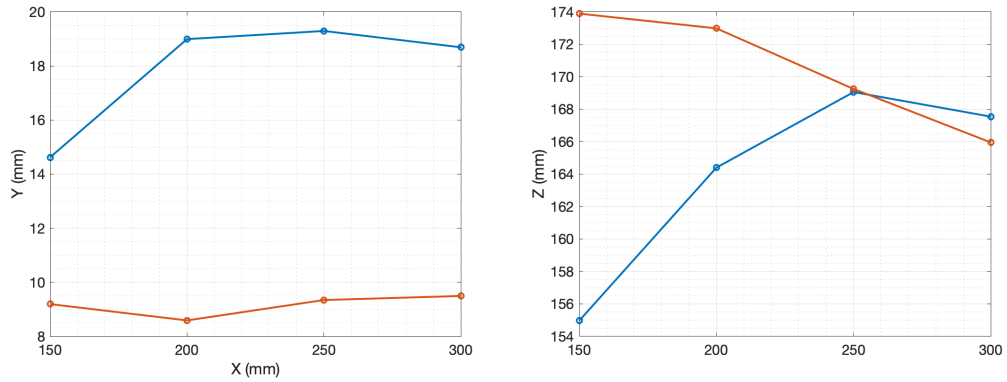


Figure 5.4: Vortex centroids for Experimental Co-Rotating Case 2

From the  $\omega_x$  contour plots in Figure 5.3 it is clear that by  $x = 1C$  the vortices had already started to rotate around each other. The right vortex which approaches the ground is also smaller than the right, despite the vortex generators being set to the same angle of attack, due to the vortex being strained as it passes between the other vortex and the ground. At  $x = 2C$ , the vortex which passed closest to the ground was starting to merge into the other. A similar merging pattern can be seen in the simulations of co-rotating vortices at an initial height of  $\frac{h_0}{a_0} = 1.67$ . By the final downstream location the vortices were not fully merged. Lateral movement of the vortices is obvious in this case and it can be seen from Figure 5.4 that the left vortex rapidly moves towards the other, with a difference in lateral position of 12.5mm between the first and last measurement planes. Like in the previous experimental case, vortex rebound was observed.

### 5.1.0.3 Co- Rotating Case 1

Co-Rotating Case 1 is the co-rotating case with the widest initial spacing, with an  $\frac{a_0}{b_0} = 0.1$  and an initial height above the ground plane of,  $\frac{h_0}{a_0} = 1.67$ . Vortex merging has been shown to commence at a spacing of  $\frac{a}{b} \approx 0.24$  [14], therefore the effect of ground effect on the evolution of a vortex pair before merging has commenced can be observed.

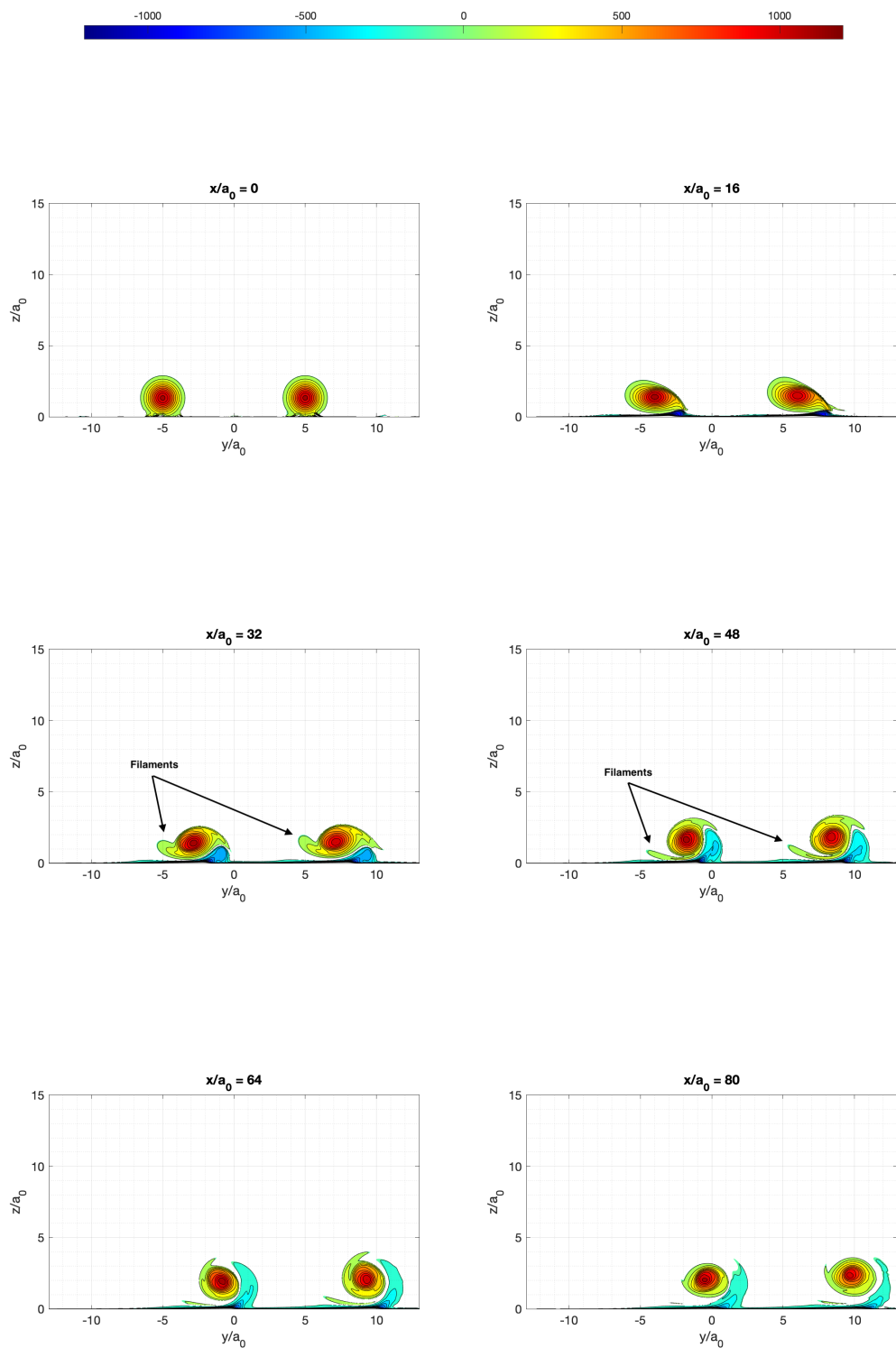


Figure 5.5: Contours of  $\omega_x$  for Co-Rotating Case 1.

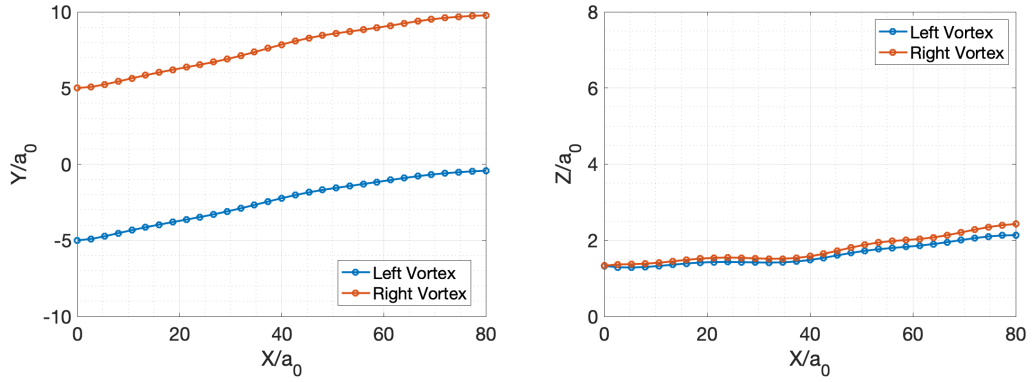


Figure 5.6: Vortex centroids for Co-Rotating Case 1. The trajectories in the XY plane are shown on the left and in the XZ plane on the right.

Figure 5.5 shows contours of  $\omega_x$  at multiple streamwise locations. The vortices are initially symmetric and at the same height with no boundary layer present at  $\frac{x}{a_0} = 0$ . At  $\frac{x}{a_0} = 16$  the vortices start to move laterally and stretch in the direction parallel to the line between their centroids. A layer of opposite sense, secondary vorticity, forms at the ground and is starting to separate under the primary vortices at the right side. This is similar to the formation and separation of boundary layer vorticity observed in the simulations of Kramer et al [28]. This separation of secondary vorticity occurred due to the suction peak below the vortex core and the vortex also induced a cross flow. As there was a suction peak below the vortex the cross flow is subject to an adverse pressure gradient after it passed under the vortex, which caused a bubble of separated secondary vorticity to form. [25] The primary vortices then start to form filaments at  $\frac{x}{a_0} = 32$  as they move laterally, they also start to rebound away from the wall. The filaments increase in length by  $\frac{a}{a_0} = 48$  but as the vortices move away from the ground start to become more axisymmetric again at  $\frac{x}{a_0} = 64$  and  $\frac{x}{a_0} = 80$ . The vortices also remain close to symmetric as they move downstream. The secondary vorticity which detaches from the wall moves upwards and is drawn around the primary vortices at  $\frac{a}{a_0} = 48$ ,  $\frac{a}{a_0} = 64$  and  $\frac{a}{a_0} = 80$ .

The trajectories of the vortices are almost identical, as shown in Figure 5.6, with both vortices moving  $5.4a_0$  laterally and  $1.1a_0$  vertically. As the trajectories of each vortex are almost identical, the separation distance,  $b$ , between the vortices remained close to initial separation,  $b_0$ . The angle of orientation of the pair is also close to 0 throughout the domain. Whereas, in the experiments of Cerretelli and

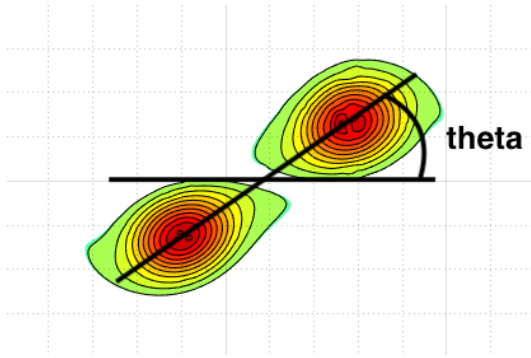


Figure 5.7: Definition of the angle of orientation, theta.

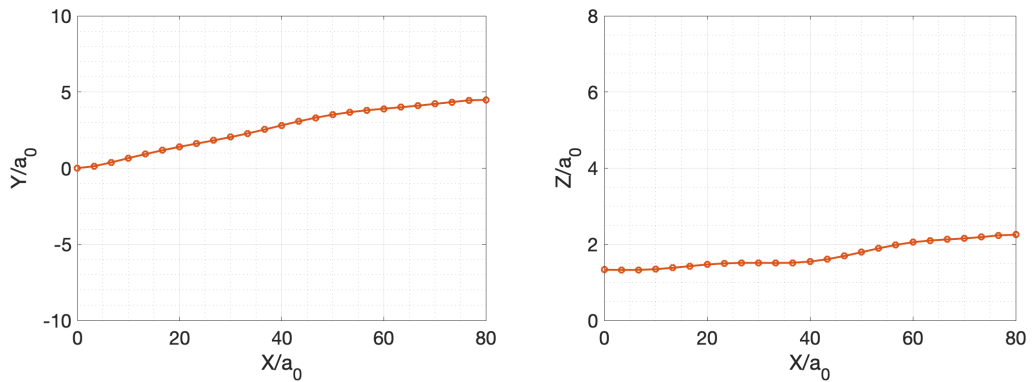


Figure 5.8: Vortex centroids for a single vortex ( $\frac{h_0}{a_0} = 1.67$ ). The trajectories in the XY plane are shown on the left and in the XZ plane on the right.

Williamson [17], for the out of ground effect vortex pair, with an initial spacing of  $\frac{a_0}{b_0} = 0.118$ , the orientation angle of the pair increases linearly during the first diffusive stage of merging. The angle of orientation is defined as shown in Figure 5.7. Therefore the vortices at this spacing and initial height are behaving like single vortices in ground effect. Further evidence of this can be seen by comparing Figure 5.6 to Figure 5.8. The y- and z-trajectories of the single vortex are almost identical to the trajectories of each of the two vortices in the pair with initial spacing  $\frac{a_0}{b_0} = 0.1$ .

#### 5.1.0.4 Co-Rotating Case 2

Co-Rotating Case 2 is a simulation of a vortex pair with an initial spacing only slightly wider than the critical spacing of  $\frac{a}{b} \approx 0.24$  [14] allowing the evolution of the pair to be observed from before the onset of merging. However, due to the closer initial spacing the likelihood of merging occurring within the domain is increased compared to Co-Rotating Case 1. The initial height of the pair is  $\frac{h_0}{a_0} = 1.67$ .

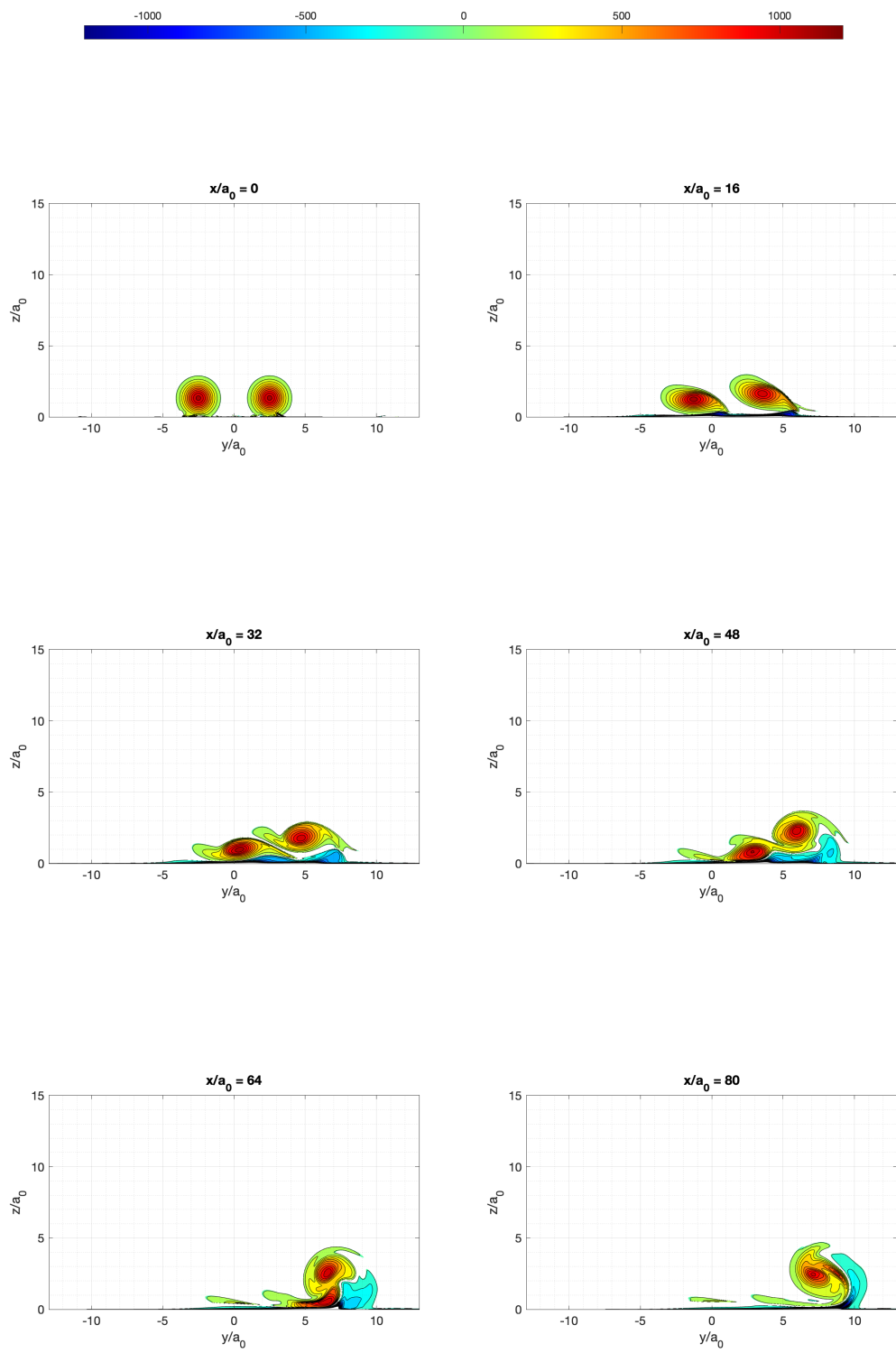


Figure 5.9: Contours of  $\omega_x$  for Co-Rotating Case 2.

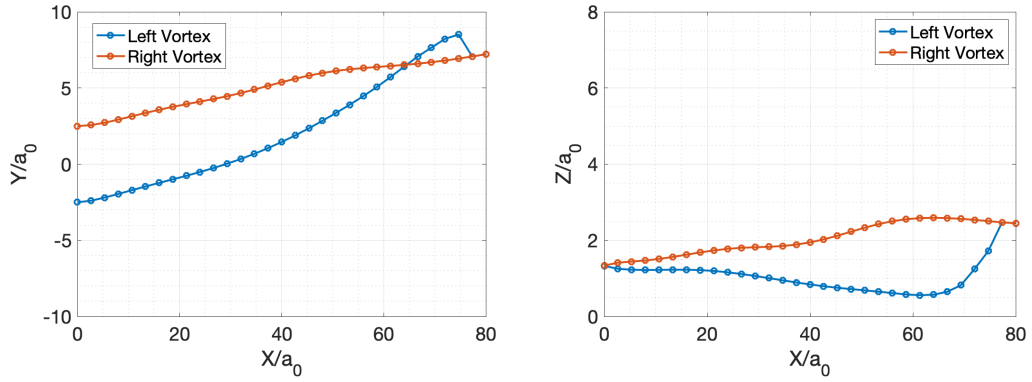


Figure 5.10: Vortex centroids for Co-Rotating Case 2. The trajectories in the XY plane are shown on the left and in the XZ plane on the right.

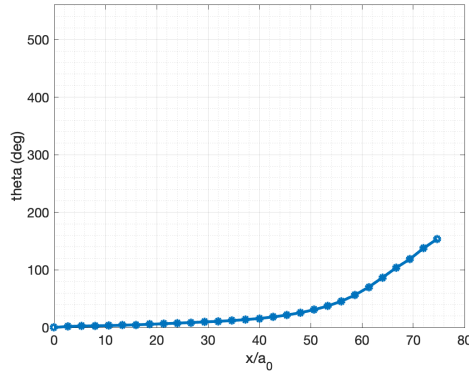


Figure 5.11: Angle of orientation for Co-Rotating Case 2.

The contours of  $\omega_x$  in Figure 5.9 show the initially symmetric vortex pair move laterally due to the ground effect and image vortices and start to deform. At  $\frac{x}{a_0} = 16$  it can be seen that the vortices become asymmetric, the direction of the stretching of the vortices differs and the left vortex remains closer to the ground. Similarly to Case 1, secondary vorticity starts to form under each vortex at the right hand side. By  $\frac{x}{a_0} = 32$  the vortices have become more asymmetric, as the left vortex starts to move under the right and compared to the right vortex has become even more elongated and both vortices have formed filaments. The layer of secondary vorticity under the left vortex remains flat whereas under the right vortex the secondary vorticity is starting to separate from the ground. Further downstream at  $\frac{x}{a_0} = 48$ , the right side vortex becomes more axisymmetric and the left vortex continues to move between the right vortex and the ground. There is also an increase in secondary vorticity.

At  $\frac{x}{a_0} = 64$  and  $\frac{x}{a_0} = 80$  the initially left vortex continues to rotate around the right vortex, passing between the right vortex and the ground. At the most downstream position the secondary vorticity which separated was advected up and around the vortex pair.

Both vortices move laterally due to the effect of the mirror image vortices, as previously stated, the initially left sided vortex moves  $9.7a_0$ , which is around 2 times further laterally than the right side vortex, which is different from Case 1 where the vortices follow almost identical paths. Vertically, vortex rebound can be seen in the initially right sided vortex, the vortex moved steadily upwards due to the secondary vorticity until  $\frac{x}{a_0} \approx 65$  where the height decreased due to the interaction with the other primary vortex. In contrast, the initially left sided vortex moved closer to the ground as the vortex pair started to rotate around each other, until  $\frac{x}{a_0} \approx 65$  where it rapidly moved upwards. The trajectories are shown in Figure 5.10. At  $\frac{x}{a_0} \approx 77$ , two vortices were no longer separable, despite not being merged. The rotation of the vortex pair is suppressed by the ground at this spacing and height, with the angle of orientation remaining close to 0, until  $\frac{x}{a_0} = 40$  where it rapidly increases. This can be seen in Figure 5.11.

A schematic of a co-rotating vortex pair close to the ground and the mirror image vortices is shown in Figure 5.12. From this it is clear to see the effect of the image vortices inducing a lateral movement on the primary vortices, as mentioned above. It is also clear to see that the secondary vorticity induces a vertical velocity on the primary vortices and causes rebound. As identified by Wang et al. [9], these effects cause the observed promoted merging for a co-rotating vortex pair in ground effect. As the secondary vorticity is closer to the right vortex, the induced vertical velocity is higher and it moves away from the ground more than the left vortex. The left vortex then moves under the right as the lateral velocity on the left vortex is now higher as it is closer to its image vortex. The deformation of the vortices seen at  $\frac{x}{a_0} = 16$  can be explained by the interaction of the primary vortices with the image vortices. When the primary vortices interact with their image vortices, which form counter rotating pairs, they become stretched as shown in the schematic of a counter-rotating pair in Figure 2.10.

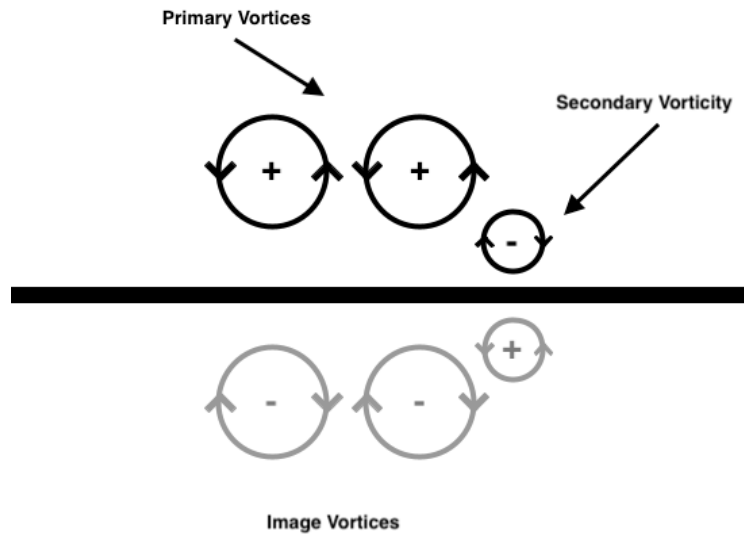


Figure 5.12: A schematic of a co-rotating vortex pair and secondary vorticity very close to the ground. The image vortices are shown below the plate.

### 5.1.0.5 Co-Rotating Case 3

Co-Rotating Case 3 is a simulation of a vortex pair with an initial spacing of  $\frac{a_0}{b_0} = 0.3$ , narrower than the critical spacing of  $\frac{a}{b} \approx 0.24$  [14] allowing the evolution of the vortex pair very close to the ground to be observed during the convective and second diffusive stages of merging. The chance of observing merging within the domain was increased compared to that of Co-Rotating Case 1 and 2 due to the closer spacing. The initial height of the pair is  $\frac{h_0}{a_0} = 1.67$ .

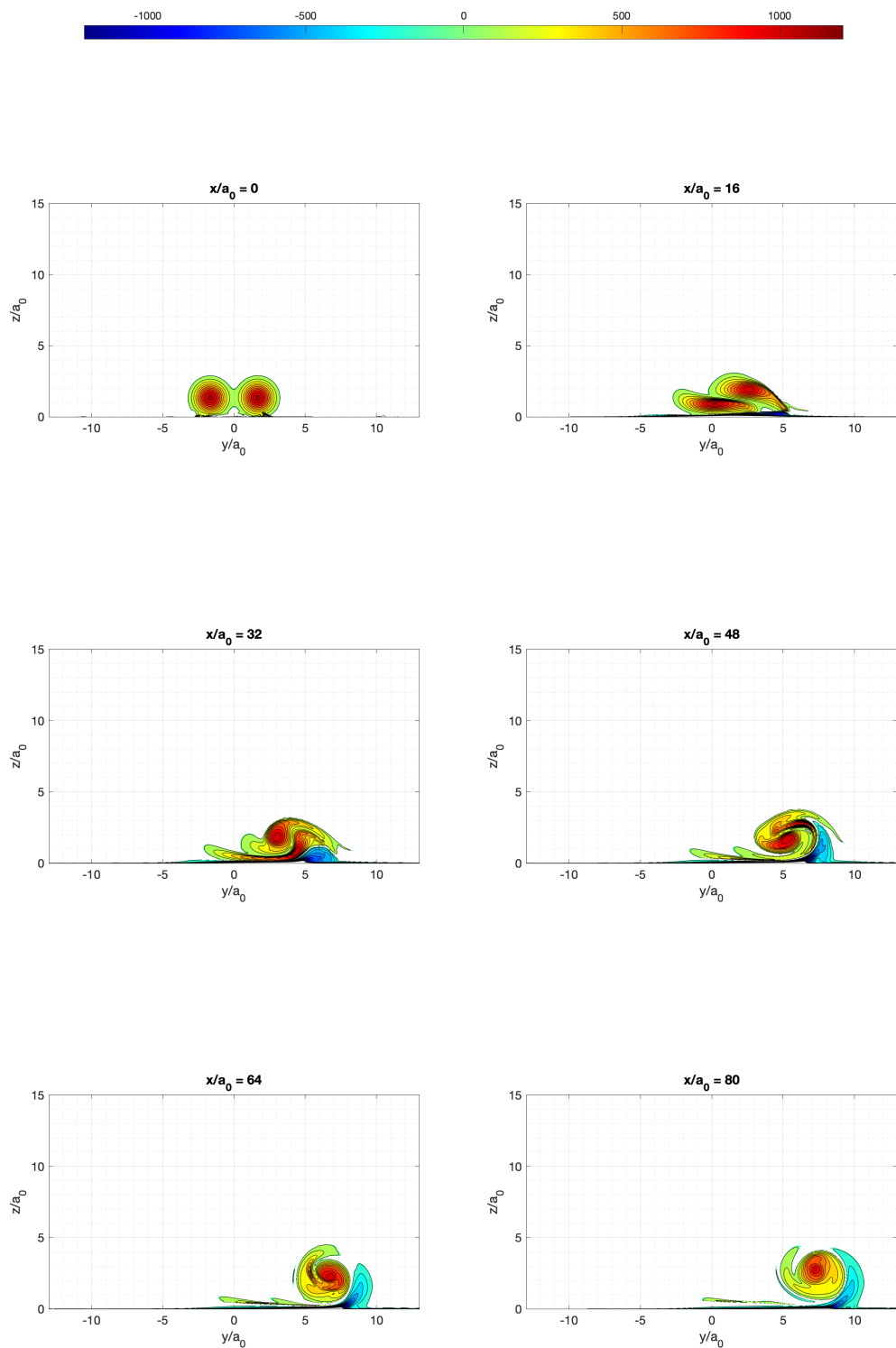


Figure 5.13: Contours of  $\omega_x$  for Co-Rotating Case 3.

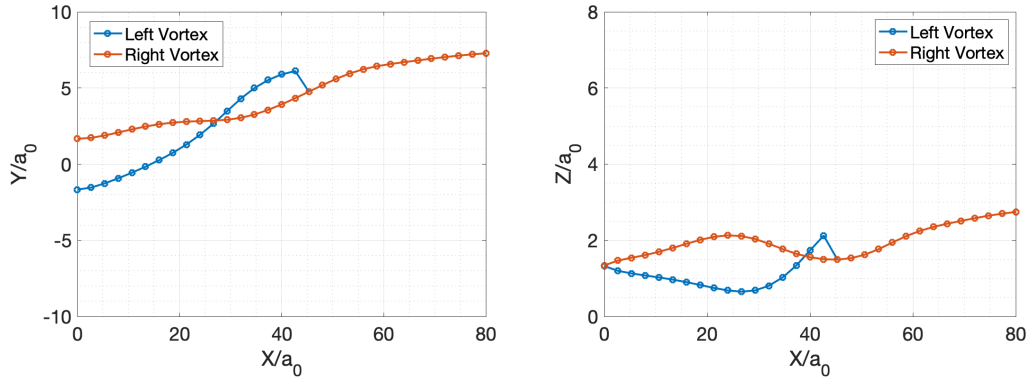


Figure 5.14: Vortex centroids Co-Rotating Case 3. The trajectories in the XY plane are shown on the left and in the XZ plane on the right.

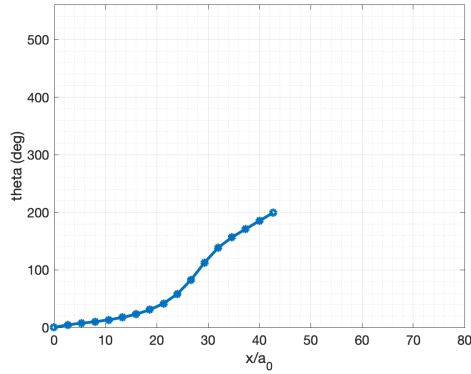


Figure 5.15: Angle of orientation for Co-Rotating Case 3.

In observing Figure 5.13, it is clear from  $\frac{x}{a_0} = 16$  that the initially left sided vortex becomes more elongated than the right side vortex as it starts to pass between the right vortex and the ground. At this streamwise location, it can also be seen that secondary vorticity forms, however unlike Co-Rotating cases 1 and 2, this vorticity only begins to separate from the ground below the right side vortex. At  $\frac{x}{a_0} = 32$  the vortex which passed closest to the ground became further elongated as it rotates around the other vortex, similar to the interaction of an asymmetric co-rotating vortex pair [19, 20]. By  $\frac{x}{a_0} = 80$  merger of the two vortices had occurred. Secondary vorticity continued to separate from the wall and was advected upwards around the vortex pair.

As shown by Figure 5.14 both vortices moved laterally with the final position of the merged vortex being  $8.95a_0$  from the initial position of the left vortex and  $5.62a_0$

different from the initial position of the right vortex. Vortex rebound also occurred, the final height of the merged vortex was  $1.41a_0$  higher than the initial height of the pair. This is higher than both Co-Rotating Cases 1 (Figure 5.6) and 2 (Figure 5.10). Like in Co-Rotating Case 2, the left vortex initially moved downwards as it moved between the right vortex and the ground. However, in contrast to Co-Rotating Case 2, the right vortex firstly moved upwards before moving down slightly as the pair rotated, before rebounding away from the wall. After  $\frac{x}{a_0} \approx 45$  two vortices were not separable. As can be seen in Figure 5.15, the pair initially rotate slowly, until the vortex which passes closest to the ground becomes partially strained and wraps around the other. After this the rotational rate rapidly increases.

#### 5.1.0.6 Co-Rotating Case 4

Co-Rotating Case 4 is the simulation with the second closest spacing, with an initial spacing of  $\frac{a_0}{b_0} = 0.4$ . This further increases the chance of observing full merging within the domain. The initial height of this case is  $\frac{h_0}{a_0} = 1.67$ .

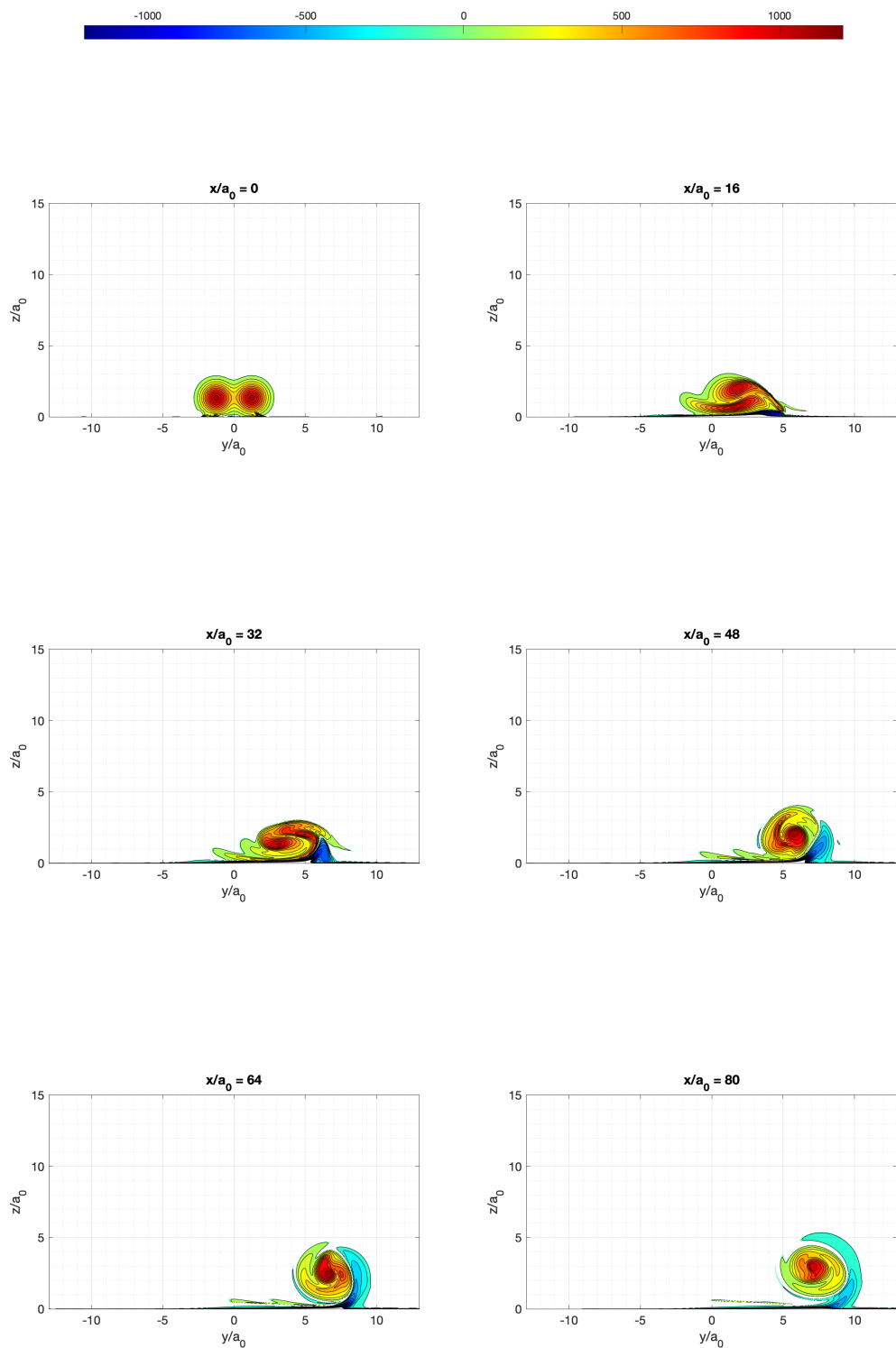


Figure 5.16: Contours of  $\omega_x$  for a Co-Rotating Case 4.

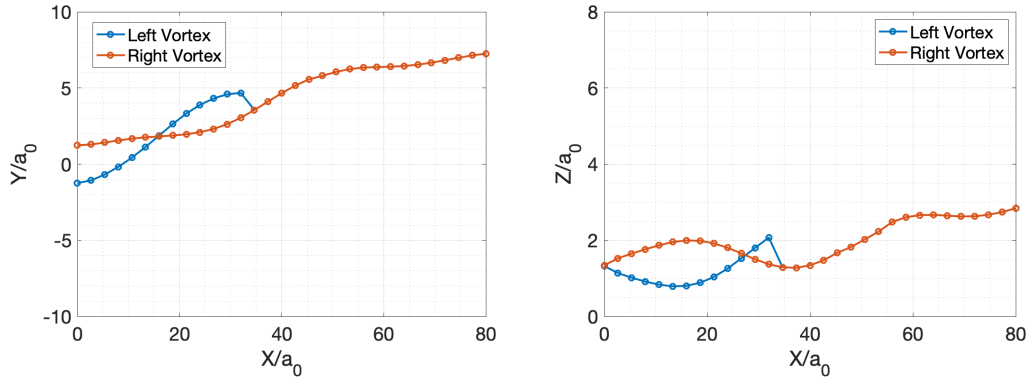


Figure 5.17: Vortex centroids for Co-Rotating Case 4. The trajectories in the XY plane are shown on the left and in the XZ plane on the right.

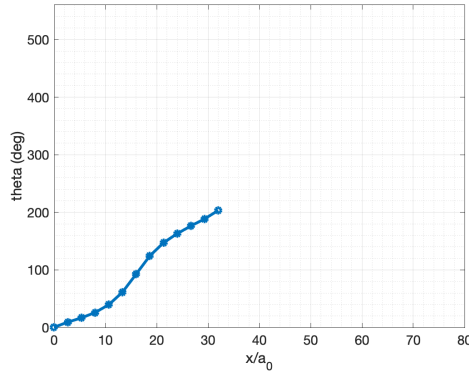


Figure 5.18: Angle of orientation for Co-Rotating Case 4.

The  $\omega_x$  contour plots, Figure 5.16, show that at this spacing then started to rotate around each other instantly, with the left vortex which passes closest to the ground becoming significantly elongated at  $\frac{x}{a_0}$  where the right vortex was less deformed but did develop a filament. Similarly to Co-Rotating Case 3, a layer of secondary vorticity forms under the vortex pair, with one region starting to separate from the ground under the right vortex. At  $\frac{x}{a_0}$  the region of separated secondary vorticity grew. The left vortex become further elongated as it wraps around the right vortex. As in Co-Rotating Cases 2 and 3, the initially symmetric vortex pair merges like an asymmetric vortex pair. At  $\frac{x}{a_0} = 80$  the pair had merged and had become more axisymmetric. At planes  $\frac{x}{a_0} = 64$  and  $\frac{x}{a_0} = 80$  the separated secondary vorticity had wrapped around the pair.

Compared to the initial positions of the left and right vortices the final merged

vortex shifted laterally by  $8.5a_0$  and  $6a_0$  respectively. The final position of the merged vortex was  $1.52a_0$  higher than  $h_0$ . This is shown in Figure 5.17 where centroids of the two vortices where separable are shown, after  $\frac{x}{a_0} \approx 35$  the centroid of the merging vortices is plotted. The vortex rebound observed in this case was greater than that of Co-Rotating Cases 1, 2 and 3. The angle of orientation of the vortex pair is shown in Figure 5.18. Unlike the previous cases, the pair begin to rotate immediately, with only a slight increase in rotational rate after the vortex which passes closest to the ground starts to wrap around the other.

#### **5.1.0.7 Co-Rotating Case 5**

Co-Rotating Case 5 has the closest spacing of all co-rotating pairs investigated. The initial spacing is  $\frac{a_0}{b_0} = 0.5$ , at this spacing the vortex cores start to touch. This allows the impact of such close spacing on the evolution and merging to be observed. Such a close spacing of vortices could occur when vortices are produced by vortex generators at different downstream locations.

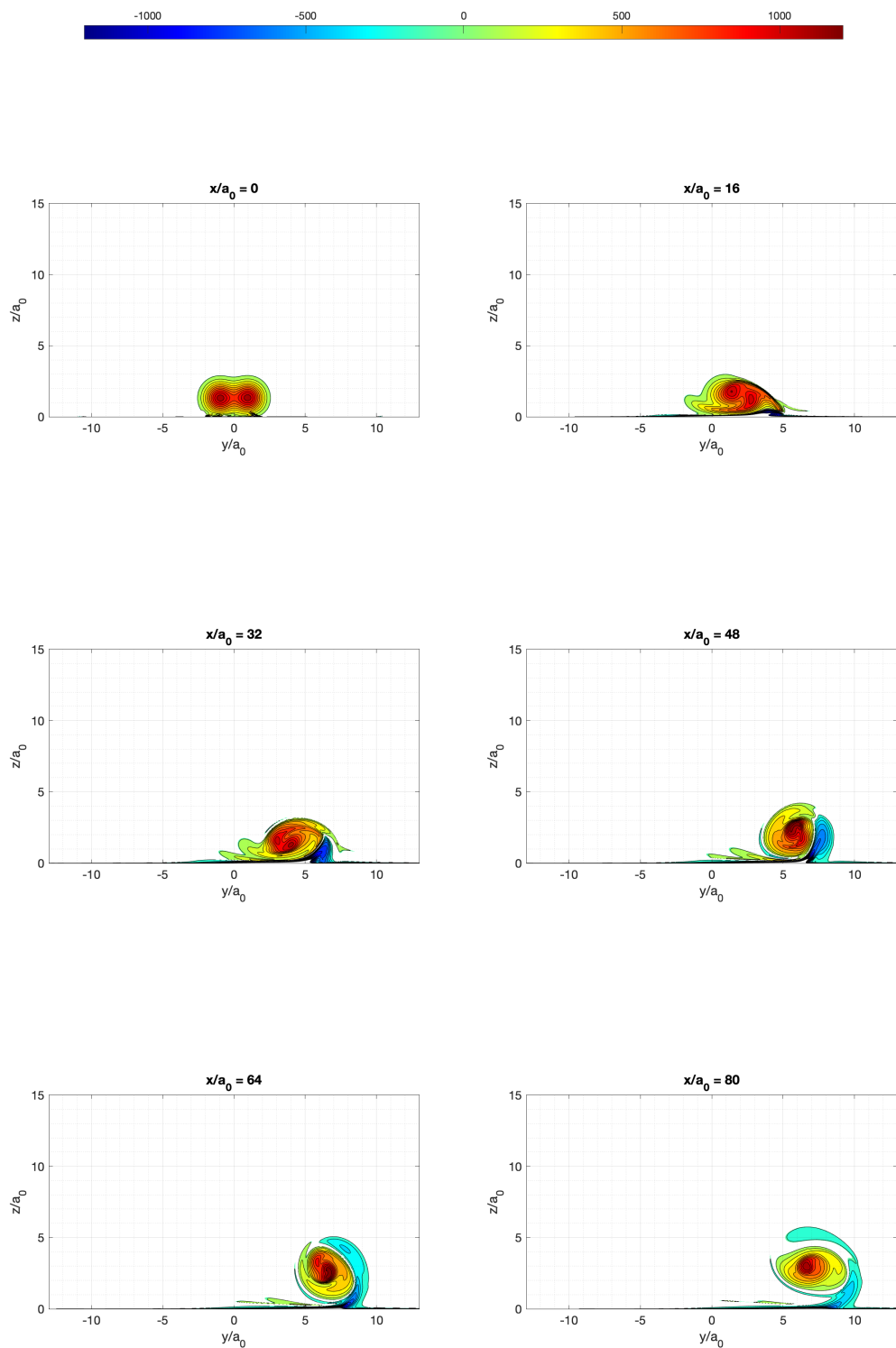


Figure 5.19: Contours of  $\omega_x$  for Co-Rotating Case 5.

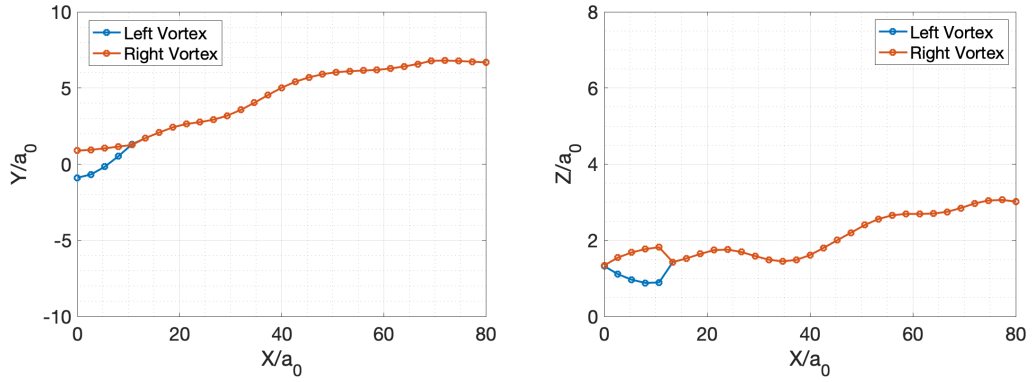


Figure 5.20: Vortex centroids for Co-Rotating Case 5. The trajectories in the XY plane are shown on the left and in the XZ plane on the right.

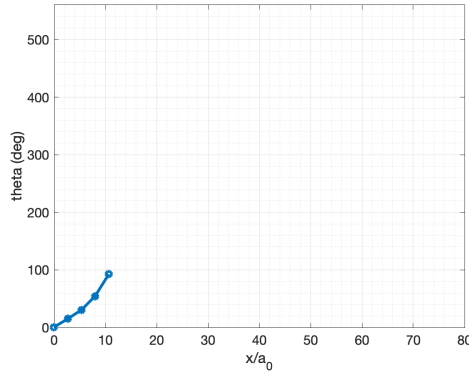


Figure 5.21: Angle of orientation for Co-Rotating Case 5.

As expected at the closest spacing the distance to merging is shortest, having merged by  $\frac{x}{a_0} = 48$ , after that the merged vortex became more axisymmetric. As in Co-Rotating Cases 2, 3 and 4, the left vortex passes closest to the ground end becomes elongated, as it rotates around the right vortex. The right vortex forms a small filament at  $\frac{x}{a_0} = 16$  and secondary vorticity started to separate from the ground below it. At  $\frac{x}{a_0} = 32$  more secondary vorticity had separated. At planes  $\frac{x}{a_0} = 48$ ,  $\frac{x}{a_0} = 64$  and  $\frac{x}{a_0} = 80$  the separated secondary vorticity was advected up and around the merged vortex causing vortex rebound. This is can be seen in Figure 5.19. The secondary vorticity wrapped further around the vortex than in Co-Rotating Cases 1, 2, 3 and 4.

Figure 5.20 shows the centroids of the two vortices for a short distance downstream, before it was not possible to separate the two vortices. After this the centroid of

the merging vortices is shown. The most downstream position of the merged vortex was shifted laterally by  $7.6a_0$  and  $5.8a_0$  compared to the initial positions of the left and right vortices respectively. This is the smallest lateral movement of the left vortex of the  $h_0 = 1.67$  cases except for the case with the widest spacing of  $\frac{a_0}{b_0} = 0.1$ . This cases also showed the greatest vortex rebound, with a final vortex height  $1.7a_0$  higher than  $h_0$ . At this close spacing, the angle of orientation, shown in Figure 5.21, started to increase rapidly immediately. However, it was only possible to calculate up to  $\frac{x}{a_0} = 10$ , as at this close spacing it quickly was not possible to separate the vortices.

#### 5.1.0.8 Co-Rotating Case 6

Co-Rotating Case 6 consists of a pair of vortices with the same spacing of  $\frac{a_0}{b_0} = 0.2$  as in Co-Rotating Case 2, however the initial height is higher. Simulations were completed for pairs of vortices at increasing heights above the ground, the initial height of the pair in this case is  $\frac{h_0}{a_0} = 5$ . This gives an  $\frac{h_0}{b_0} = 1.0$  and allows the impact of ground effect on the evolution of the vortex pair to be investigated. The spacing was chosen as it puts the vortices at a spacing wider than the critical spacing at which merging starts to occur of  $\frac{a}{b} \approx 0.24$  [14].

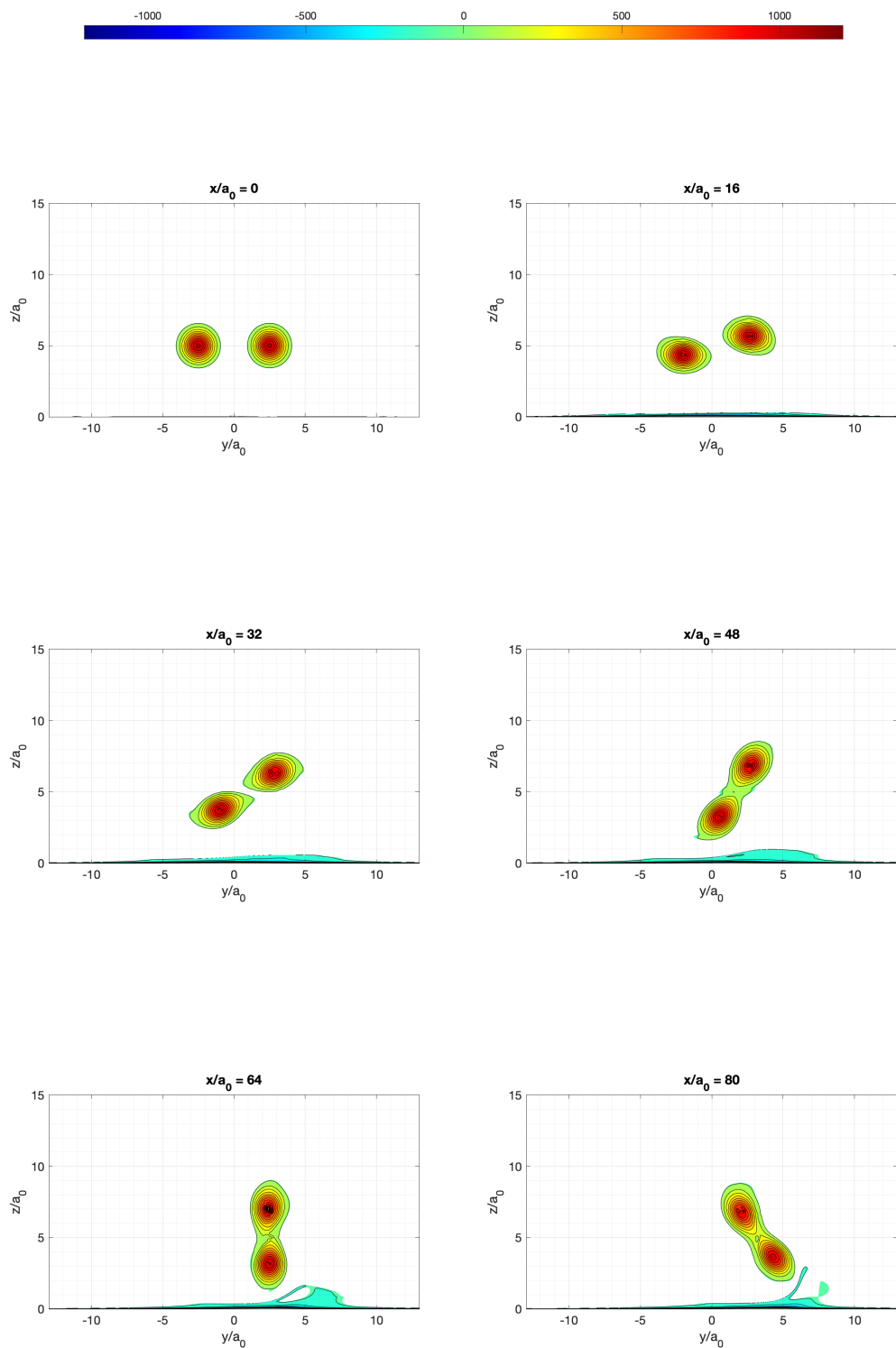


Figure 5.22: Contours of  $\omega_x$  for Co-Rotating Case 6.

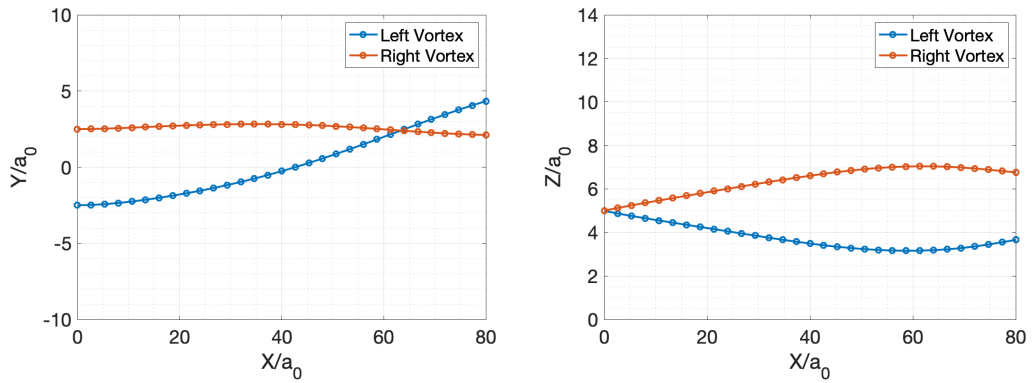


Figure 5.23: Vortex centroids for Co-Rotating Case 6. The trajectories in the XY plane are shown on the left and in the XZ plane on the right.

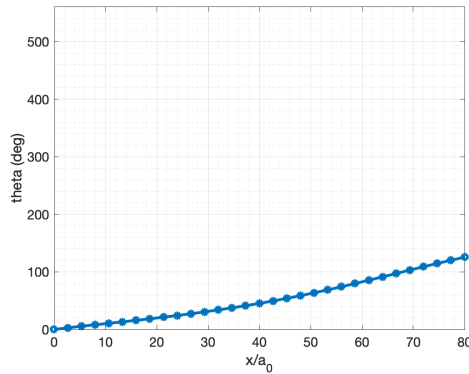


Figure 5.24: Angle of orientation for Co-Rotating Case 6.

From Figure 5.22 it can be seen that, in contrast to Co-Rotating Case 2, both vortices remained symmetrical throughout the domain. At  $\frac{x}{a_0} = 16$  the vortices had deformed slightly due to the strain induced by each vortex on the other, a layer of opposite sense vorticity also formed, unlike Co-Rotating Case 2, none of that secondary vorticity was starting to separate from the ground. Further downstream at  $\frac{x}{a_0}$ , the layer of secondary vorticity increased in thickness and the vortices continued to stretch. At  $\frac{x}{a_0} = 64$  the left vortex passed closest to the ground as the vortex pair rotated, due to this a region of secondary vorticity started to separate from the ground. Another difference between this case and Co-Rotating Case 2 (Figure 5.9) is that no filaments formed.

Figure 5.23 shows that the vortex pair shifted laterally slightly due to the ground effect, but the lateral motion of the pair became dominated by the rotation of the

pair at this initial height. The initially left vortex moved by  $6.8a_0$  in the y-direction between  $\frac{x}{a_0} = 0$  and  $\frac{x}{a_0} = 80$ . The difference in the lateral position of the right vortex between  $\frac{x}{a_0} = 0$  and  $\frac{x}{a_0} = 80$  was  $-0.4a_0$ . The motion in the z-direction was also dominated by the rotation of the pair, due to the small amount of secondary vorticity separating from the ground in this case, the left vortex which passed closest to the ground was  $1.34a_0$  lower than  $h_0$  at  $\frac{x}{a_0} = 80$  and the right vortex was  $1.76a_0$  higher at the same downstream location. Figure 5.24 shows the angle of orientation of the pair, it can be seen that the vortices start to rotate around each other immediately, unlike in Counter-Rotating Case 2 (Figure 5.11). The final orientation angle of the pair was 120 degrees.

Figure 5.25 shows a schematic of a co-rotating vortex pair similar to that of Co-Rotating Cases 6 to 11 and its image vortices. It can be seen that the image vortices interact with the primary vortices, inducing a lateral velocity, however as the distance between them is larger than in Figure 5.12, the induced velocity is lower. There is also the induced vertical velocity due to the secondary vorticity. These two effects result in the promoted merging, as identified by Wang et al. [9]. These effects also influence the rotational rate of the vortex pair, as will be discussed further in 6. The deformations of the vortices can again be explained by the interaction between primary vortices and their image vortices. The primary-image counter rotating vortex pairs, deform similarly to the counter-rotating pair shown in Figure 2.10.

#### 5.1.0.9 Co-Rotating Case 7

Co-Rotating Case 7 consists of a pair of vortices with the same spacing of  $\frac{a_0}{b_0} = 0.2$  as in Co-Rotating Case 2, however the initial height is higher. Simulations were completed for pairs of vortices at increasing heights above the ground, the initial height of the pair in this case is  $\frac{h_0}{a_0} = 7.5$ . This gives an  $\frac{h_0}{b_0} = 1.5$  and allows the impact of ground effect on the evolution of the vortex pair to be investigated.

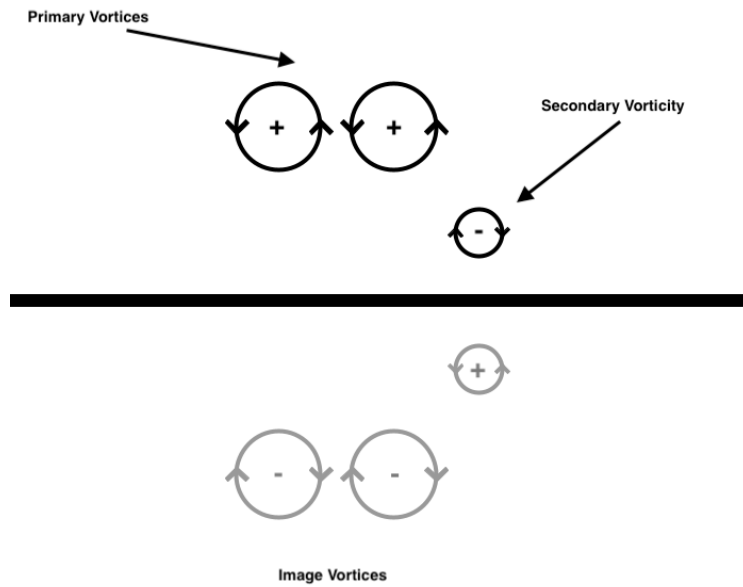
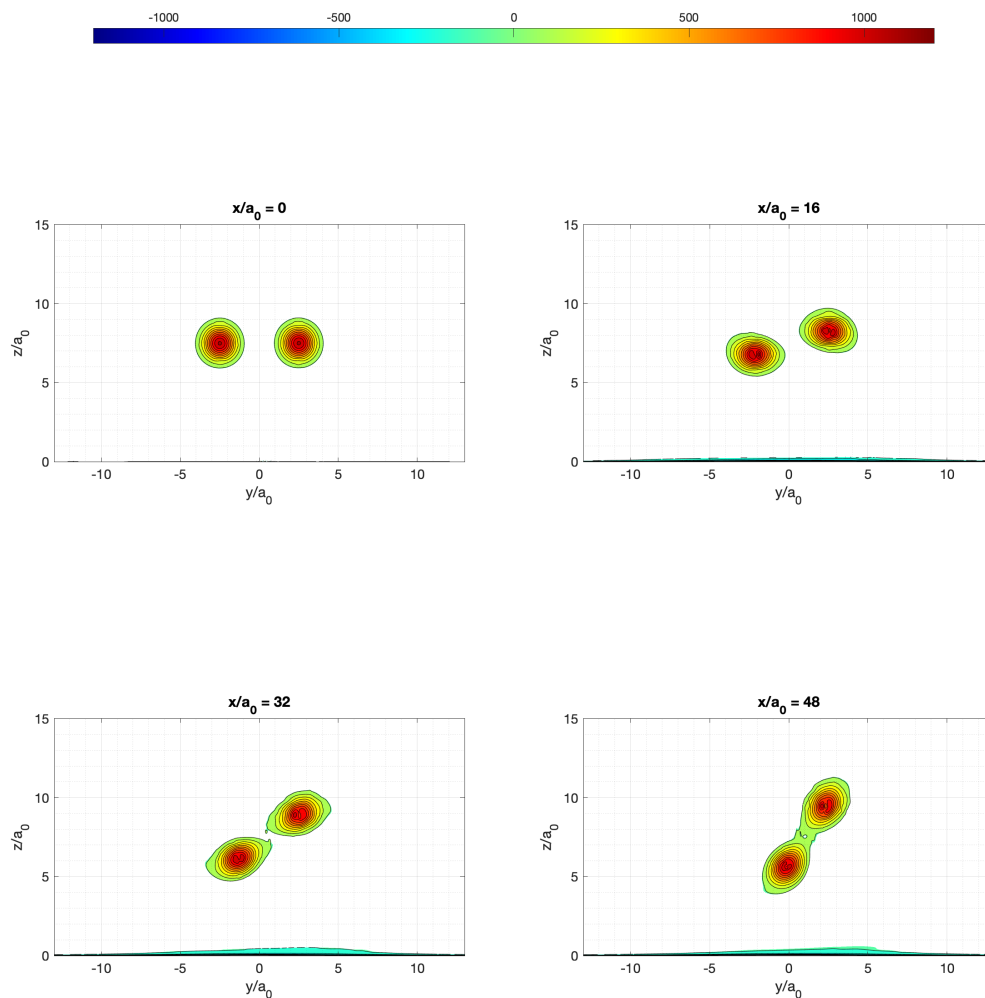


Figure 5.25: A schematic of a co-rotating vortex pair and secondary vorticity in ground effect, but further from the ground than in Figure 5.12. The image vortices are shown below the plate.



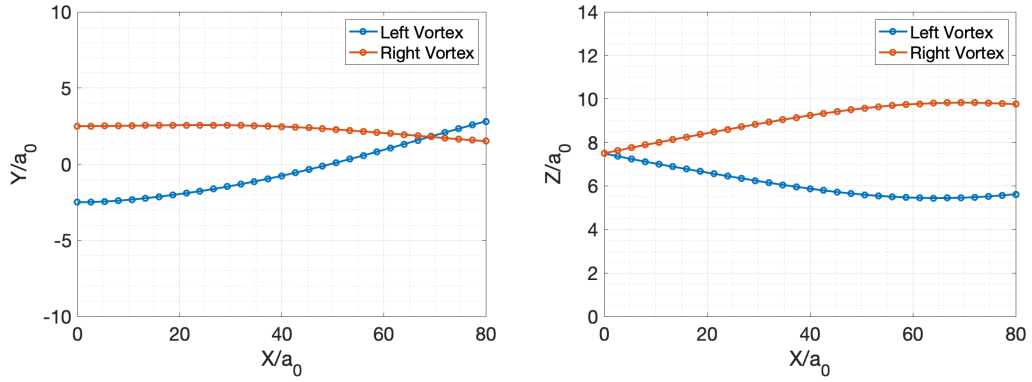


Figure 5.27: Vortex centroids for Co-Rotating Case 7. The trajectories in the XY plane are shown on the left and in the XZ plane on the right.

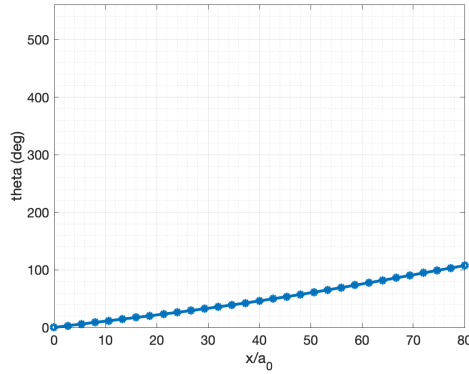


Figure 5.28: Angle of orientation for Co-Rotating Case 7.

The  $\omega_x$  plots of Figure 5.26 show that the vortices had started rotating around each other and deform by  $\frac{x}{a_0} = 16$ . Also at this streamwise location, a layer of secondary vorticity had formed. At  $\frac{x}{a_0} = 32$  the layer of secondary vorticity had increased in thickness, however, unlike Co-Rotating Case 6, there was no further growth in the thickness of the layer moving further downstream, even when the vortex passed closest to the ground. At  $\frac{x}{a_0} = 48$  the vortices have become further elongated, but there were no further significant changes in the shape of the vortices. As in Co-Rotating Case 6, no filaments formed, which differed from the case with the same spacing but lowest initial height. It can also be seen in the plots that the vortex pair shifts laterally due to the proximity of the ground.

Figure 5.27 also shows that lateral motion of the vortex pair. The left vortex moved  $5.3a_0$  between  $\frac{x}{a_0} = 0$  and  $\frac{x}{a_0} = 80$  and the right vortex moved  $-a_0$ . Similarly

to Co-Rotating Case 6, the lateral motion was dominated by the rotation of the pair. There was no rebound observed for the vortex pair at this  $h_0$  due to the lack of secondary vorticity separating from the ground, as this has been shown to cause vortex rebound [28, 26, 27, 9]. The rate of rotation of the vortex pair, shown in Figure 5.28, was slower than that of Counter-Rotating Case 6, which had a lower initial height and the same initial spacing. The final orientation angle was 110 degrees.

#### 5.1.0.10 Co-Rotating Case 8

Co-Rotating Case 8 is the case with the spacing of  $\frac{a_0}{b_0} = 0.2$  with the highest initial height, with a height of  $\frac{h_0}{a_0} = 10$ . This gives an  $\frac{h_0}{b_0} = 2.0$  and allows the impact of ground effect on the evolution of the vortex pair to be investigated.

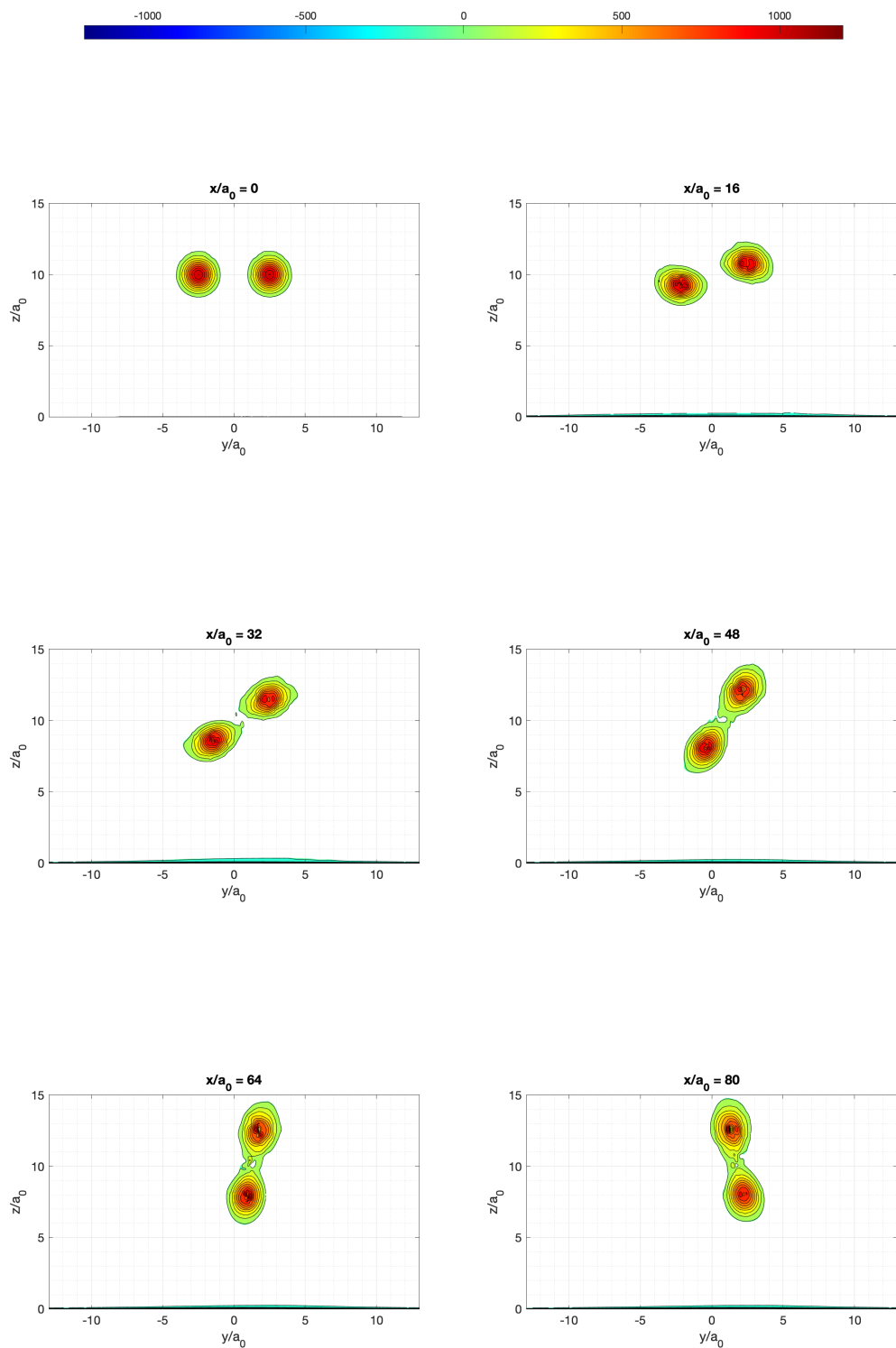


Figure 5.29: Contours of  $\omega_x$  for Co-Rotating Case 8.

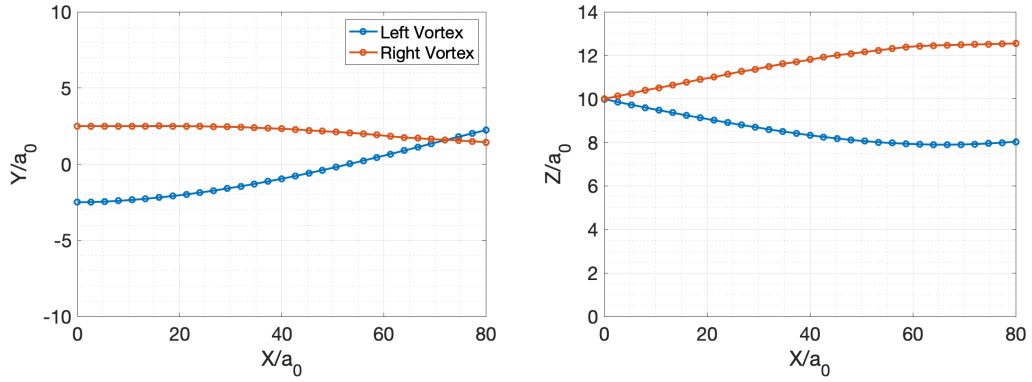


Figure 5.30: Vortex centroids for Co-Rotating Case 8. The trajectories in the XY plane are shown on the left and in the XZ plane on the right.

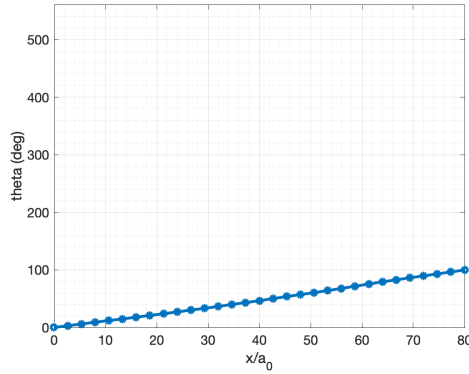


Figure 5.31: Angle of orientation for Co-Rotating Case 8.

It can be seen in Figure 5.29 that the vortices had started to deform due to the induced strain [10] by  $\frac{x}{a_0} = 16$  however, the vortices had changed from their initial shape less at this location when compared to Co-Rotating Cases 2, 6 and 7. Also, layer of secondary vorticity had formed at that location. At  $\frac{x}{a_0} = 48$ , the vortices had elongated and remained similarly shaped throughout the domain from that position onwards. The layer of secondary vorticity did not increase in thickness like with Co-Rotating Cases 6 and 7.

From the plots of the vortex centroids in Figure 5.30 the lateral movement of the vortex pair can be seen, which moved  $3.67a_0$  laterally. Like with Co-Rotating Case 7, no vortex rebound was observed due to the small layer of secondary vorticity remaining attached to the ground [28, 26, 27, 9]. The angle of orientation is shown in Figure 5.31. The rate of increase in orientation angle is slower at this initial height

than for the vortex pairs with the same initial spacing but lower initial heights of Co-Rotating Cases 6 and 7, with the vortex pair at this height reaching a final angle of 100 degrees.

#### **5.1.0.11 Co-Rotating Case 9**

Co-Rotating Case 9 has the same spacing of  $\frac{a_0}{b_0} = 0.3$  as Co-Rotating Cases 3, 10 and 11, but with a higher initial height than case 3 of  $\frac{h_0}{a_0} = 3.33$ . This initial height gives an  $\frac{h_0}{b_0} = 1$ . The increased  $h_0$  allows the impact of ground effect on the interaction of the co-rotating vortex pair to be investigated.

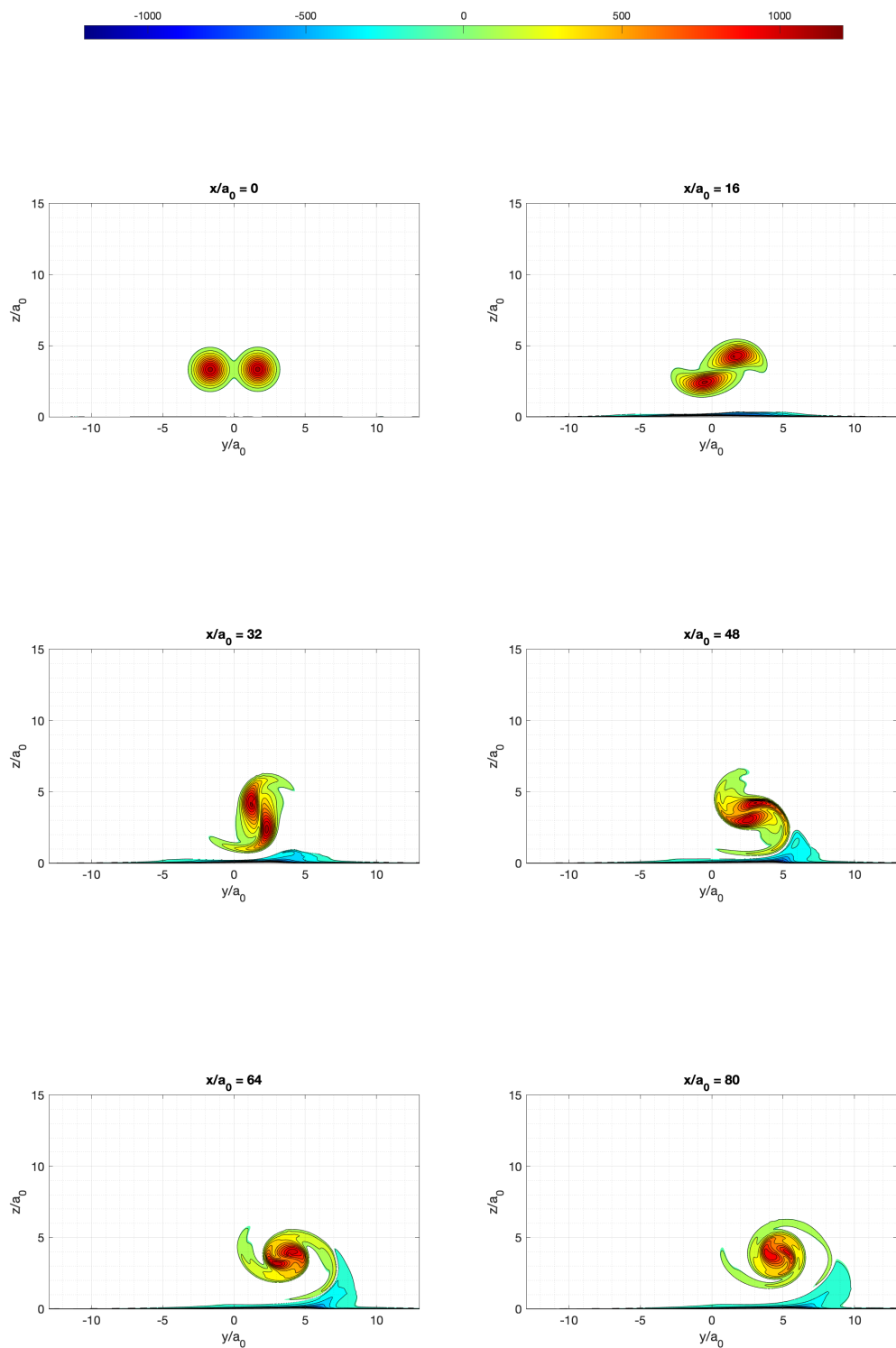


Figure 5.32: Contours of  $\omega_x$  for Co-Rotating Case 9.

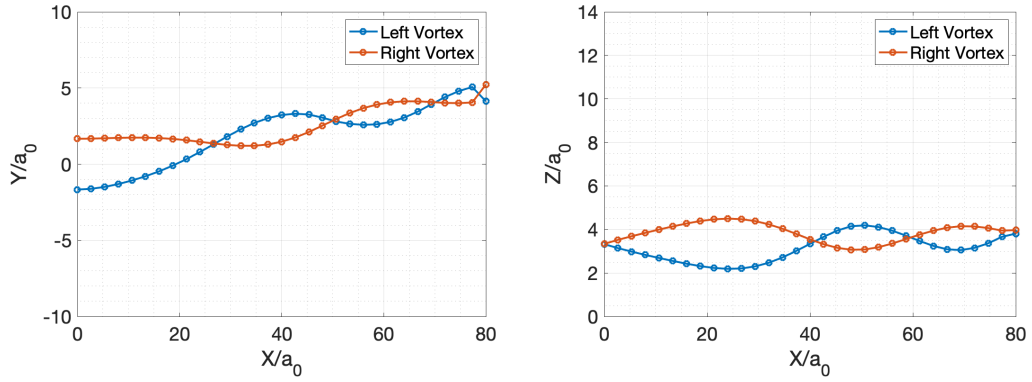


Figure 5.33: Vortex centroids for Co-Rotating Case 9. The trajectories in the XY plane are shown on the left and in the XZ plane on the right.

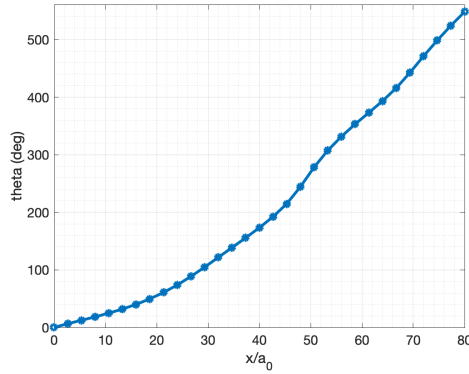


Figure 5.34: Angle of orientation for Co-Rotating Case 9.

In observing Figure 5.32 it can be seen the vortices quickly started to rotate around each other. At  $\frac{x}{a_0} = 16$ , the left vortex was starting to approach the ground and both vortices were starting to develop filaments. A layer of secondary vorticity was also present at this streamwise location. At  $\frac{x}{a_0} = 32$ , the left vortex had moved past the position where it was closest to the ground, as a result secondary vorticity had started to separate from the ground. Both vortices developed filaments, however the filament of the vortex which passed closest to the ground was more elongated than that of the other vortex. Filaments form when  $\omega_x$  diffuses into the outer recirculation region, shown in Figure 2.2, the rotation within this region then elongates this  $\omega_x$  into filaments [17]. Moving to the subsequent downstream locations, the region of separated secondary vorticity grows and is advected upwards and the filaments of the vortices become more symmetric. The vortex pair was

un-merged at the final location of  $\frac{x}{a_0} = 80$ .

There was a lateral movement of the vortex pair, as shown by Figure 5.33, with the initially left vortex moving  $5.8a_0$  and the initially right vortex moving  $3.6a_0$  in the y-direction. A small amount of vortex rebound was observed with both vortices final heights being less than  $a_0$  higher than their initial height. As the vortices move towards each other the rate of increase of the orientation angle increases, reaching a final orientation angle of 550 degrees. This can be seen in Figure 5.34.

#### 5.1.0.12 Co-Rotating Case 10

Co-Rotating Case 10 has the same spacing of  $\frac{a_0}{b_0} = 0.3$  as Co-Rotating Cases 3, 9 and 11, but with a higher initial height than cases 3 and 9 of  $\frac{h_0}{a_0} = 5$ . This initial height gives an  $\frac{h_0}{b_0} = 1.5$ .

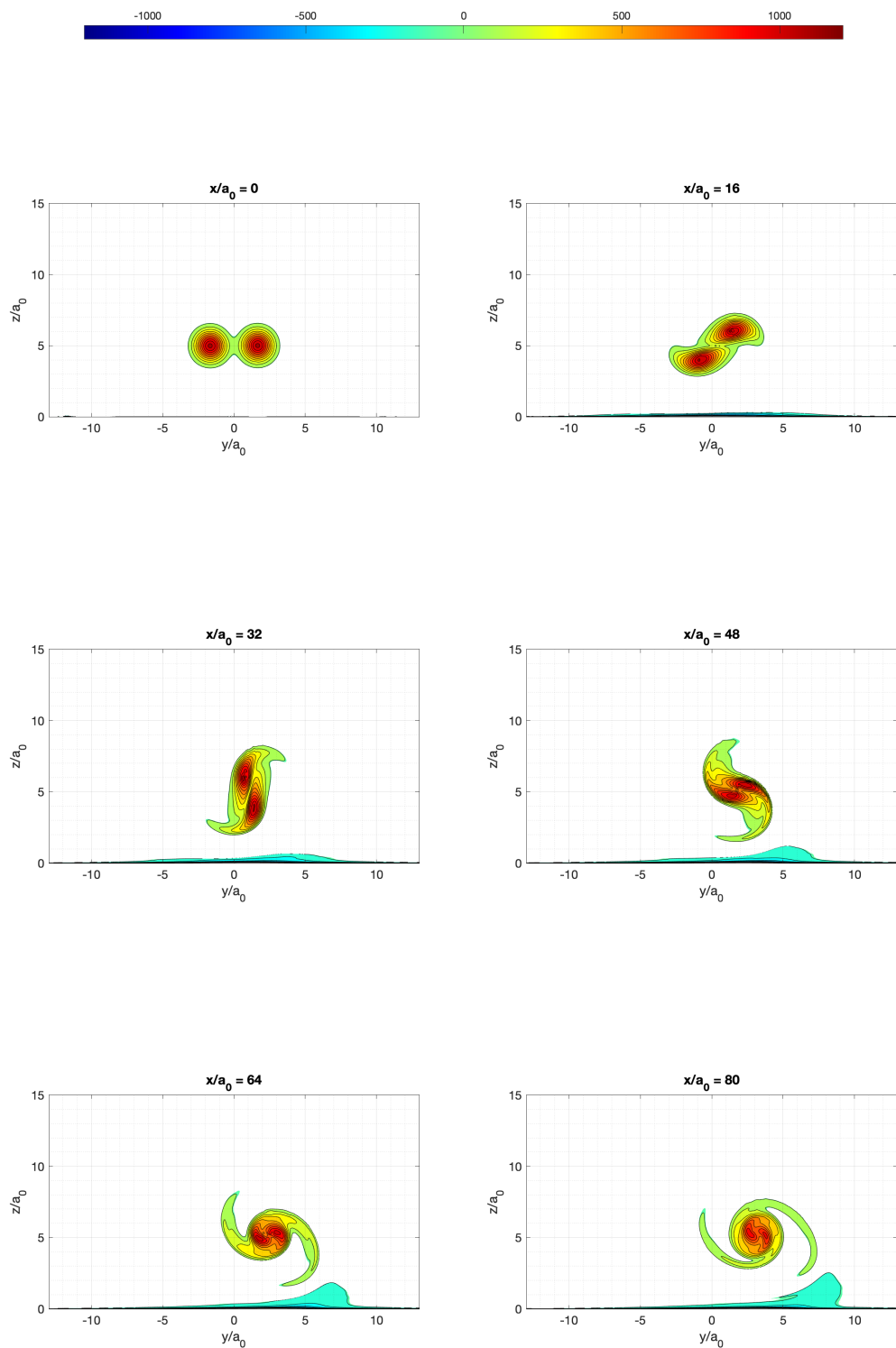


Figure 5.35: Contours of  $\omega_x$  for Co-Rotating Case 10.

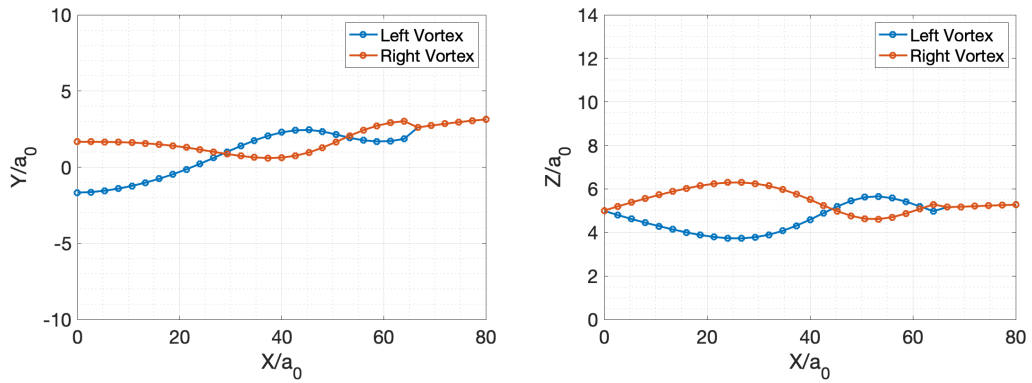


Figure 5.36: Vortex centroids for Co-Rotating Case 10. The trajectories in the XY plane are shown on the left and in the XZ plane on the right.

Figure 5.35 shows the initially axisymmetric vortices quickly become stretched and started to develop filaments by  $\frac{x}{a_0} = 16$ . A layer of secondary vorticity had also formed. This layer increased in thickness at  $\frac{x}{a_0} = 32$  before separating from the ground at  $\frac{x}{a_0} = 48$ . At  $\frac{x}{a_0} = 32$  the vortices formed filaments, which then grew by  $\frac{x}{a_0} = 48$ , where the filament of the vortex which passed closest to the ground was longer than the other. At  $\frac{x}{a_0} = 64$  the filaments had become symmetric. Like in Co-Rotating Case 9, the vortices remained un-merged.

A lateral movement of the vortex pair was observed in Figure 5.36, however no significant vortex rebound was observed. The initially left vortex moved by  $4.8a_0$  in the y-direction between  $\frac{x}{a_0} = 0$  and  $\frac{x}{a_0} = 80$ . Figure 5.37 shows the angle of orientation for the vortex pair, the rotational rate of the pair increased as the vortices moved downstream and towards each other.

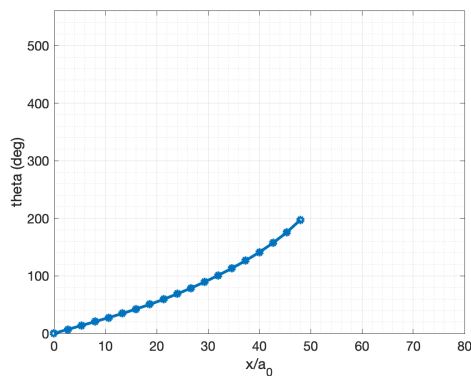


Figure 5.37: Angle of orientation for Co-Rotating Case 10.

### 5.1.0.13 Co-Rotating Case 11

Co-Rotating Case 11 is the case with a spacing of  $\frac{a_0}{b_0} = 0.3$  with the highest initial height, with an  $h_0 = 6.67$  and an  $\frac{h_0}{b_0} = 2$ .

From Figure 5.38 it can be seen that the vortex pair quickly started to rotate and stretch and filaments started to form. At  $\frac{x}{a_0} = 16$ , the pair had rotated less than at the same streamwise location for Co-Rotating Cases 9 and 10. A layer of secondary vorticity had formed by  $\frac{x}{a_0} = 16$ , which increased in thickness moving downstream until  $\frac{x}{a_0} = 8-$  where the thickness decreased. At  $\frac{x}{a_0} = 48$  the filament of the vortex which passed closest to the ground was longer than the other, as in Co-Rotating Cases 9 and 10, but by  $\frac{x}{a_0} = 64$  the filaments were symmetric. The vortices did not merge by the most downstream location.

Lateral motion of the vortices was observed, this motion was less than in Co-Rotating Cases 9 and 10, with the initially left and right vortices moving  $4a_0$  and  $0.7a_0$  in the y-direction respectively. There was no vortex rebound observed for this case, due to the lack of secondary vorticity separating from the ground. The paths of the vortices are shown in Figure 5.39. As with previous co-rotating cases, the rotational rate of the pair increased as the vortices moved towards each other. This is shown in Figure 5.40.

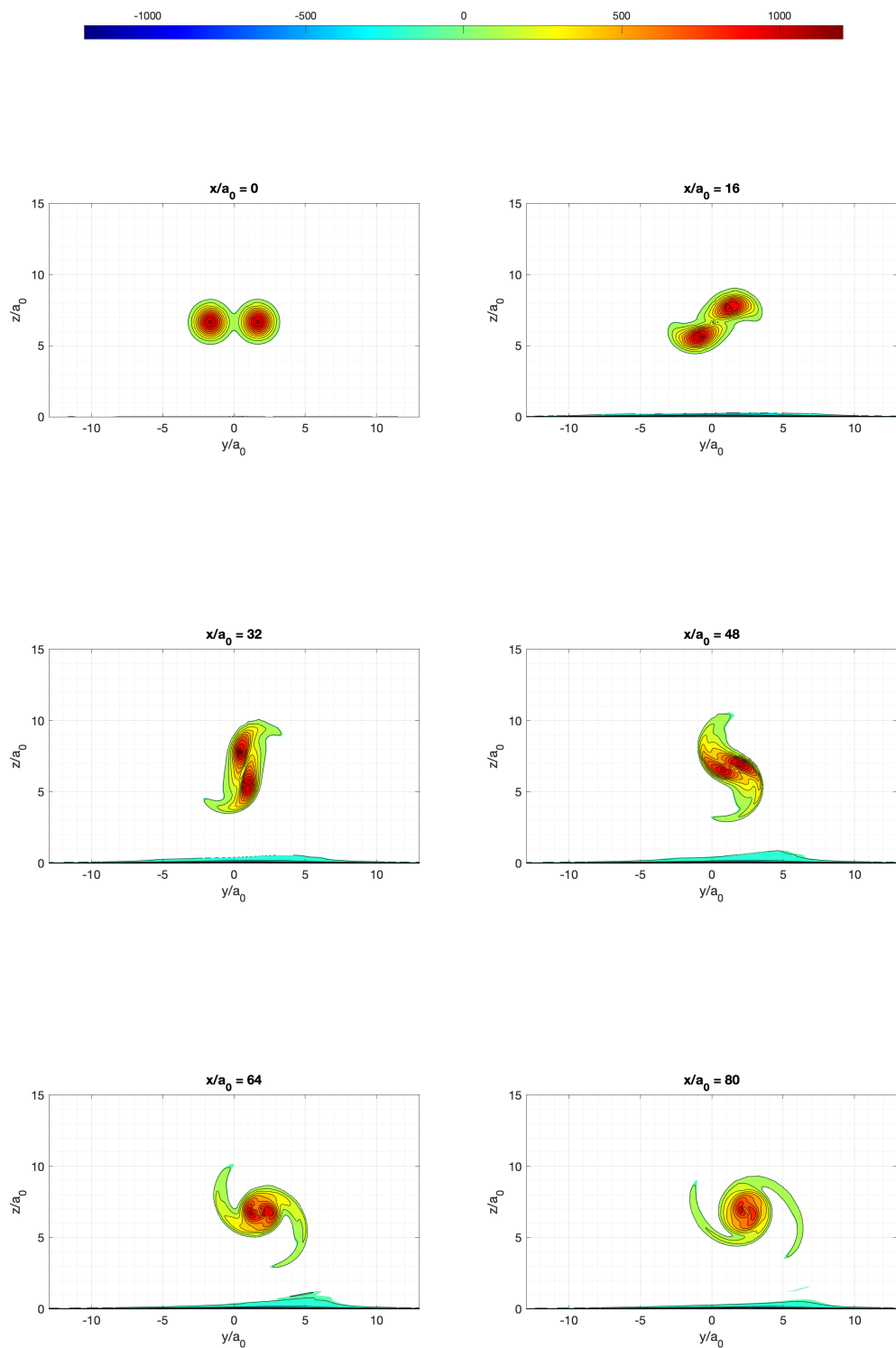


Figure 5.38: Contours of  $\omega_x$  for Co-Rotating Case 11.

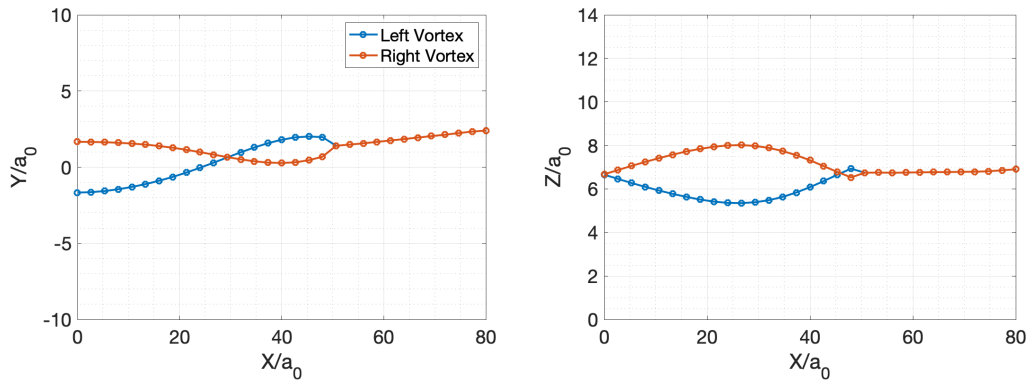


Figure 5.39: Vortex centroids for Co-Rotating Case 11. The trajectories in the XY plane are shown on the left and in the XZ plane on the right.

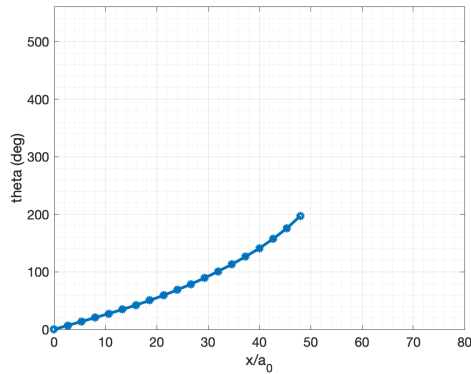


Figure 5.40: Angle of orientation for Co-Rotating Case 11.

## 5.2 Counter-Rotating Results

### 5.2.0.1 Counter- Rotating Case 1

Counter-Rotating Case 1 is a simulation of a counter-rotating vortex pair at an initial spacing of  $\frac{a_0}{b_0} = 0.1$  and initial height of  $\frac{h_0}{a_0} = 1.67$ . This is the same spacing as in Co-Rotating Case 1, however the vortices are counter rotating in such a way that the vortices will move towards each other and away from the ground. This configuration was chosen as there has been less research for such counter rotating pairs than of those that move downwards and away from each other, this configuration can be seen in Figure 5.41.

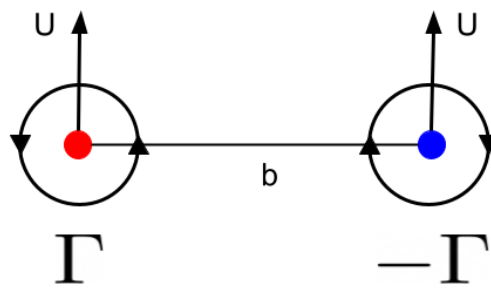


Figure 5.41: A schematic of the configuration of the counter-rotating vortex pairs investigated.  $U$  is the vertical velocity each vortex induces upon the other and  $b$  is the separation distance.

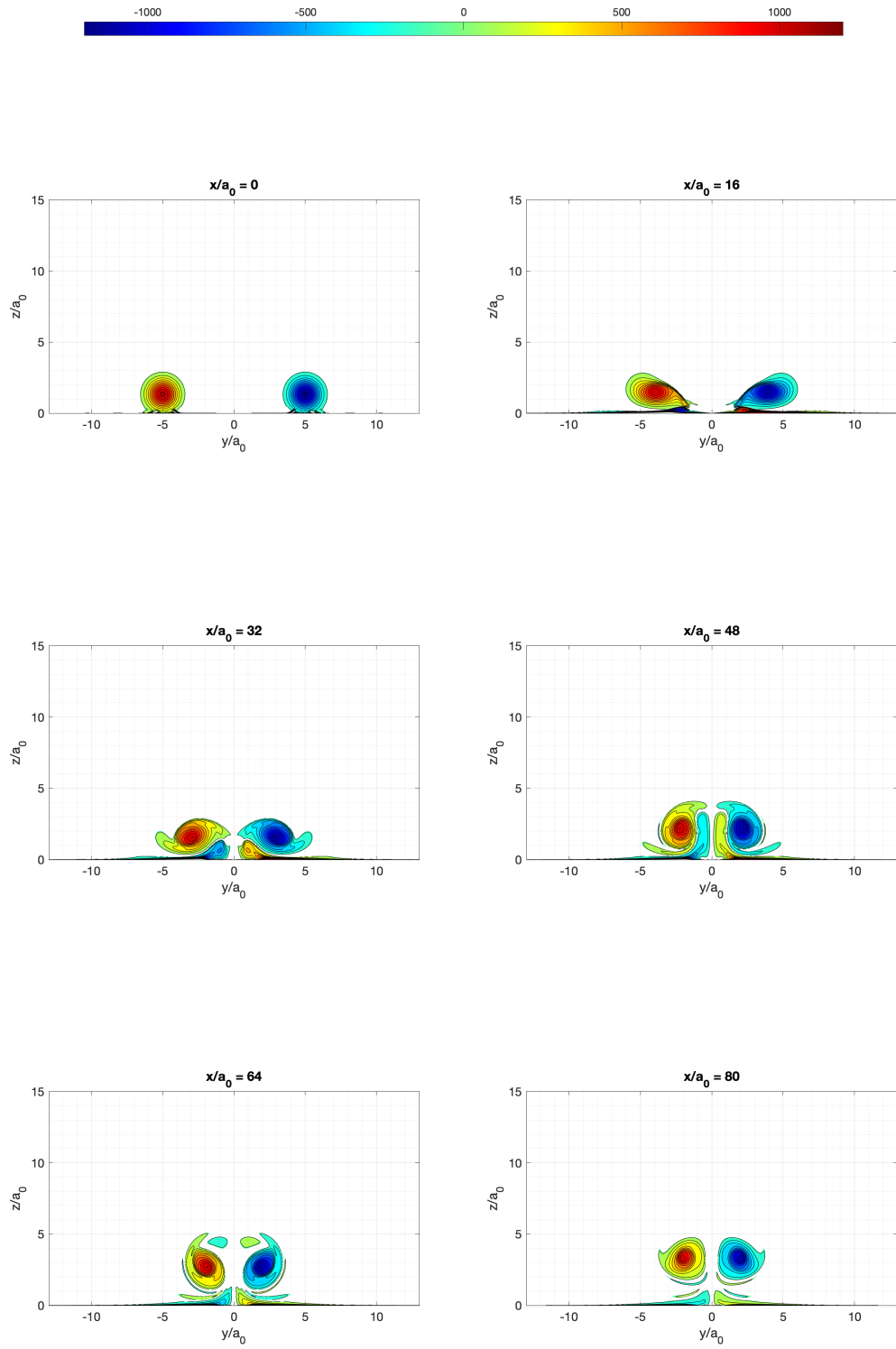


Figure 5.42: Contours of  $\omega_x$  for Counter-Rotating Case 1.

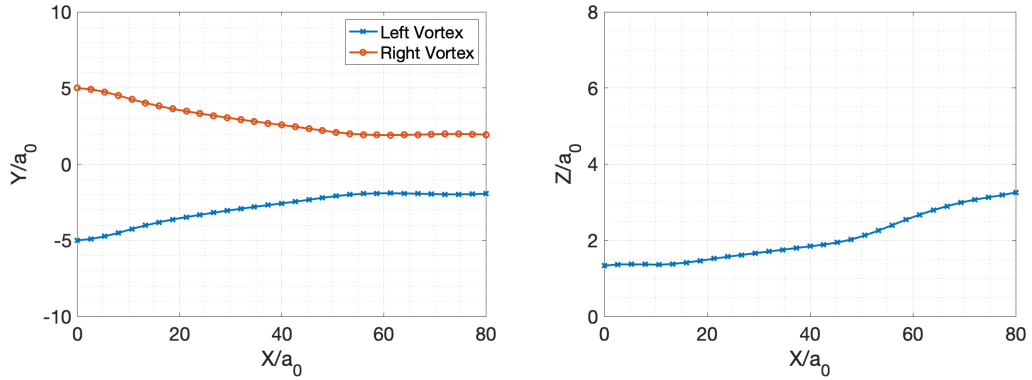


Figure 5.43: Vortex centroids for Counter-Rotating Case 1. The trajectories in the XY plane are shown on the left and in the XZ plane on the right.

$\omega_x$  contour plots in Figure 5.42 show that as the pair begins to shift laterally by  $\frac{x}{a_0} = 16$ , the vortices started to stretch parallel to the line between their centres. Counter-rotating pairs usually stretch normal to the line between their centres however due to the ground plane and the distance between them they do not. Also at this location, secondary vorticity had started to form at the ground, similar to the formation of secondary vorticity in the simulations of Kramer [28]. The location of the area of separation of vorticity from the ground is at the side of the vortex which is closest to the other, this can clearly be seen at  $\frac{x}{a_0} = 32$ . At this location the vortices have started to develop filaments. At  $\frac{x}{a_0} = 48$  the separated secondary vorticity was advected up and started to wrap around the primary vortices. The separated secondary vorticity then started to rotate around the primary vortices at  $\frac{x}{a_0} = 64$  and by  $\frac{x}{a_0} = 80$  had become strained out by the stronger primary vortices.

The trajectories of the vortices are shown in Figure 5.43. The vortices moved laterally due to the induced velocity due to the ground plane, they continued to move towards each other until  $\frac{x}{a_0} = 60$  when they remained a constant distance of  $3.44a_0$  apart. In the z-direction, the pair remained a constant height above the ground until  $\frac{x}{a_0} = 10$  when they started to move upwards. At  $\frac{x}{a_0} = 50$  the vertical velocity of the pair increased and reached a final height  $1.588a_0$  higher than  $h_0$ .

As discussed above, the vortices move laterally, this can be explained by the interaction of primary vortices with their images vortices, shown in Figure 5.44. The deformation of the primary vortices seen at  $\frac{x}{a_0} = 16$ , before the primary vortices interact, can also be explained by the interaction of the primary vortices with their

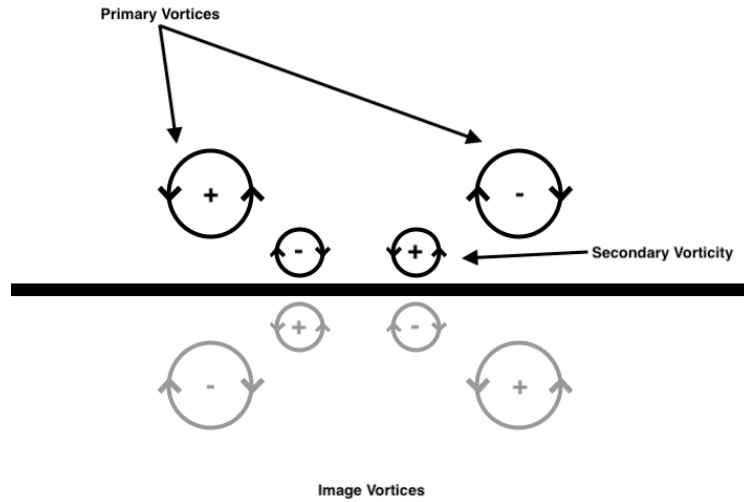


Figure 5.44: A schematic of a counter-rotating vortex pair close to the ground and its image vortices.

image vortices. They form two primary-image counter-rotating vortex pairs, and stretch perpendicular to the line separating them.

### 5.2.0.2 Counter- Rotating Case 2

Counter-Rotating Case 2 is a simulation of a counter-rotating vortex pair at an initial spacing of  $\frac{a_0}{b_0} = 0.2$  and initial height of  $\frac{h_0}{a_0} = 1.67$ . This is the same spacing as in Co-Rotating Case 2, however the vortices are counter rotating in such a way that the vortices will move towards each other and away from the ground.

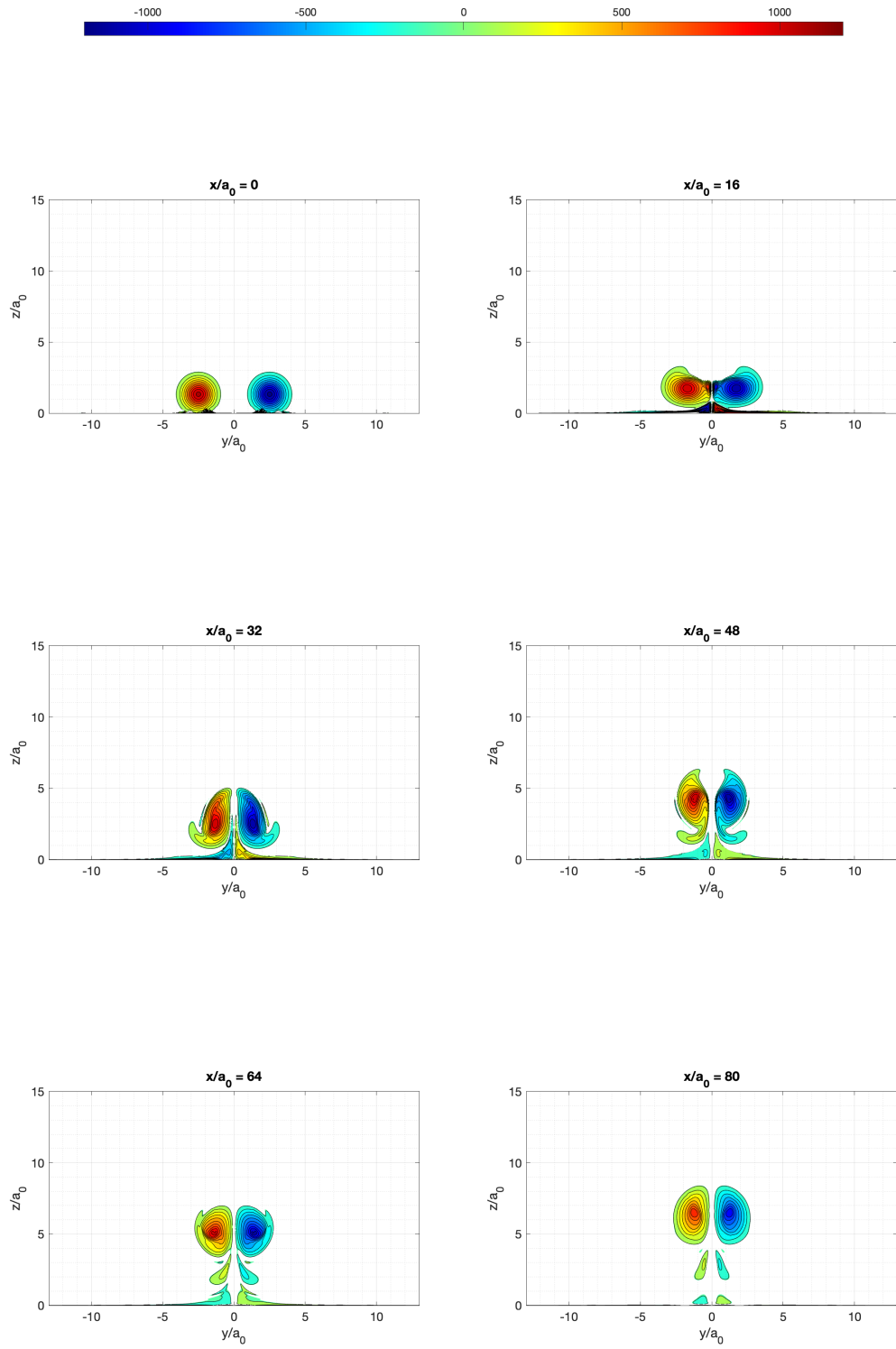


Figure 5.45: Contours of  $\omega_x$  for Counter-Rotating Case 2.

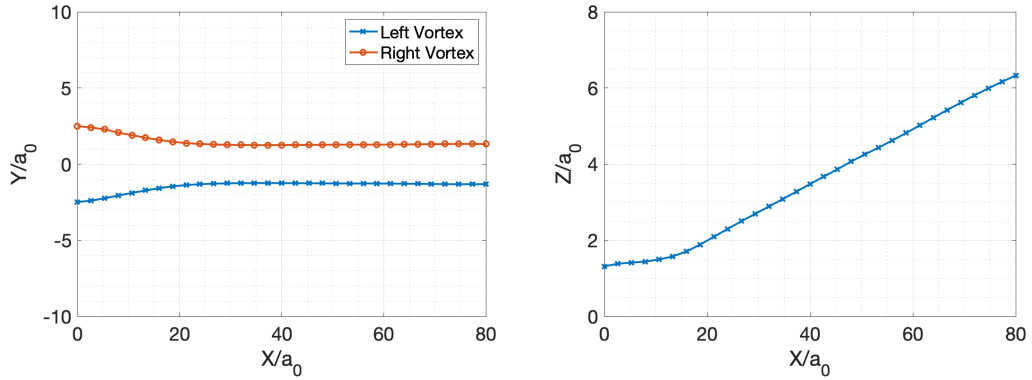


Figure 5.46: Vortex centroids for Counter-Rotating Case 2. The trajectories in the XY plane are shown on the left and in the XZ plane on the right.

Observing Figure 5.45 it can be seen that the vortices moved together quickly and had significantly reduced their spacing by  $\frac{x}{a_0} = 16$ . Secondary vorticity had also formed by that location. At  $\frac{x}{a_0} = 32$  the vortices started to develop filaments and stretch in the direction normal to the line between their centres. Secondary vorticity had also started to separate from the wall. The vortices continued to move upwards and by  $\frac{x}{a_0} = 64$  the filaments became detached from the primary vortices. The region of separated secondary vorticity also decreased in size.

From Figure 5.46 it can be seen that the vortices initially moved laterally before reaching a spacing of  $2.644a_0$  by  $\frac{x}{a_0} = 20$  and remained this distance apart as they moved downstream. The vortices initially remain a constant height above the ground before inducing a vertical velocity upon each other and moving rapidly upwards to a final height  $4.659a_0$  above  $h_0$ .

### 5.2.0.3 Counter- Rotating Case 3

Counter-Rotating Case 3 is a simulation of a counter-rotating vortex pair at an initial spacing of  $\frac{a_0}{b_0} = 0.3$  and initial height of  $\frac{h_0}{a_0} = 1.67$ . This is the same spacing as in Co-Rotating Case 3, however the vortices are counter rotating in such a way that the vortices will move towards each other and away from the ground.

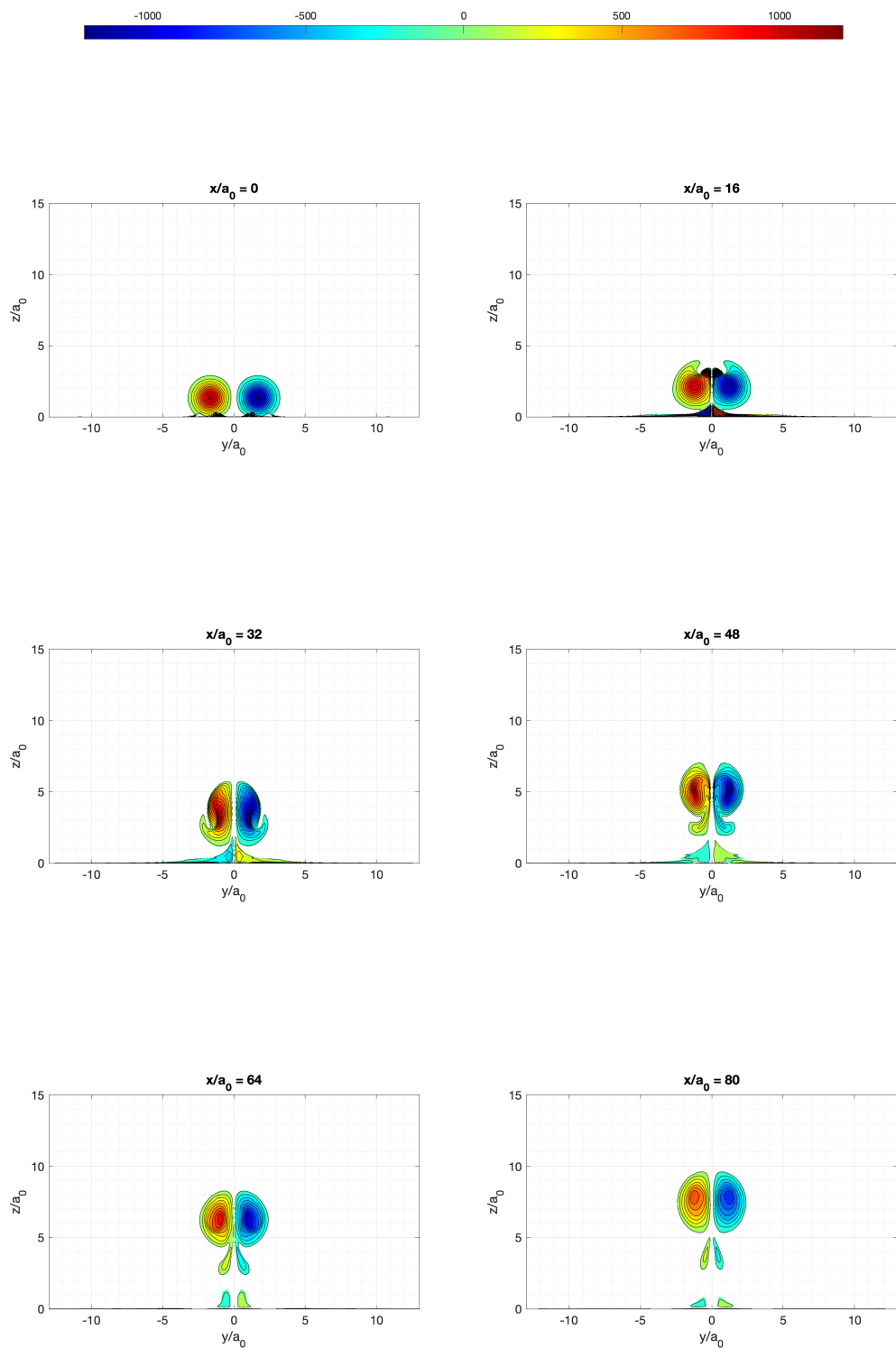


Figure 5.47: Contours of  $\omega_x$  for Counter-Rotating Case 3.

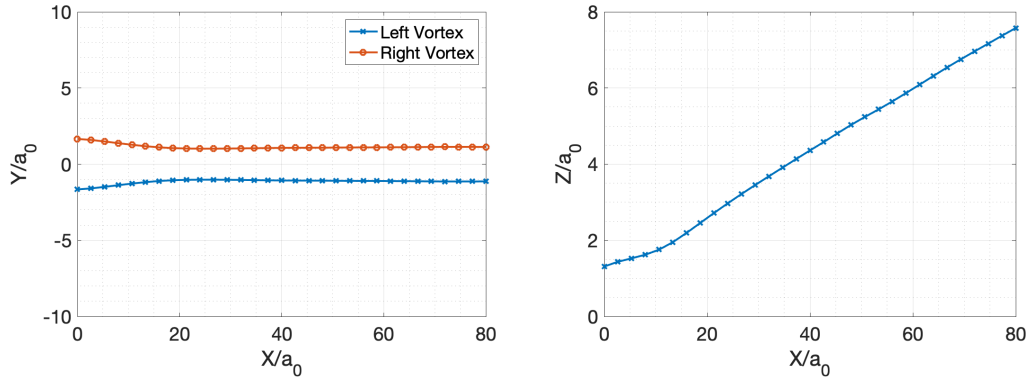


Figure 5.48: Vortex centroids for Counter-Rotating Case 3. The trajectories in the XY plane are shown on the left and in the XZ plane on the right.

As shown by Figure 5.47 the vortices moved together and filaments and second peaks of  $\omega_x$  formed as they moved towards each other at  $\frac{x}{a_0} = 16$ . Secondary vorticity also started to form. By  $\frac{x}{a_0} = 32$  the vortices had become stretched and secondary vorticity started to separate from the ground. At  $\frac{x}{a_0} = 48$  the vortices continued to move upwards due to the mutually induced vertical velocity and there was an increase in the size of the region of separated secondary vorticity. By  $\frac{x}{a_0} = 64$  the region of separated secondary vorticity had decreased and by the final downstream location the filaments detached from the primary vortices.

As shown in Figure 5.48 the vortices quickly reached their final spacing, moving to a distance of  $2.266a_0$  apart by  $\frac{x}{a_0} = 20$  and following a linear path thereafter. The vortices moved vertically initially however they saw an increase in vertical velocity at  $\frac{x}{a_0} = 15$  as they moved towards each other. The pair moved  $5.906a_0$  between the first and last planes.

#### 5.2.0.4 Counter- Rotating Case 4

Counter-Rotating Case 4 is a simulation of a counter-rotating vortex pair at an initial spacing of  $\frac{a_0}{b_0} = 0.4$  and initial height of  $\frac{h_0}{a_0} = 1.67$ . This is the same spacing as in Co-Rotating Case 4, however the vortices are counter rotating in such a way that the vortices will move towards each other and away from the ground.

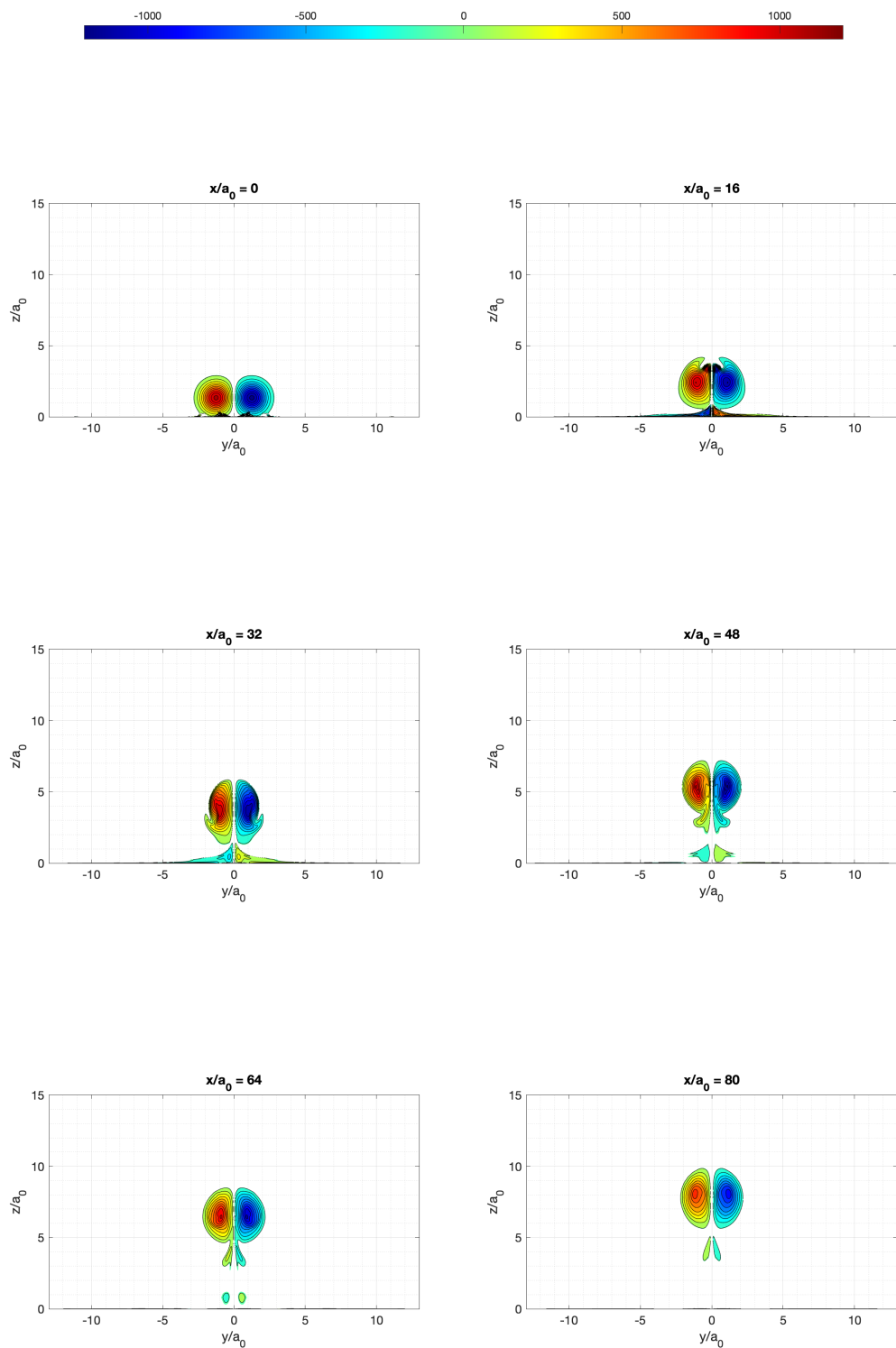


Figure 5.49: Contours of  $\omega_x$  for Counter-Rotating Case 4.

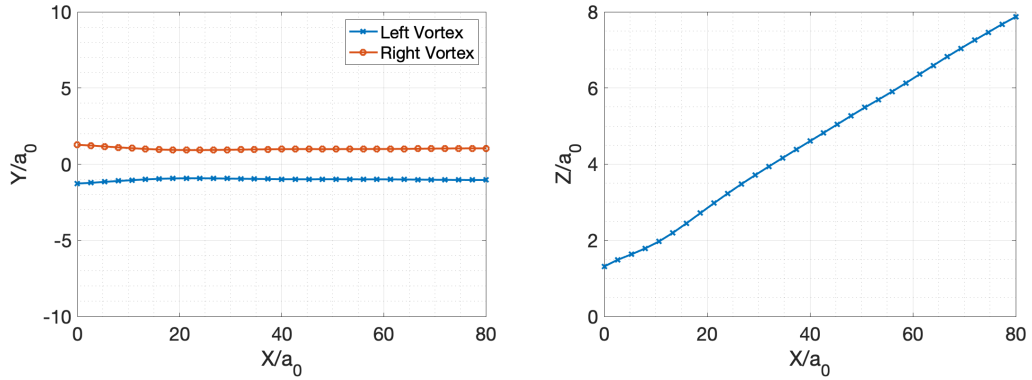


Figure 5.50: Vortex centroids for Counter-Rotating Case 4. The trajectories in the XY plane are shown on the left and in the XZ plane on the right.

The  $\omega_x$  contour plots can be seen in Figure 5.49. At  $\frac{x}{a_0} = 0$  the vortices were not circular at this close spacing. By  $\frac{x}{a_0} = 16$ , the vortices had started to stretch. They also formed filaments and second peaks of  $\omega_x$ . At  $\frac{x}{a_0} = 32$  the vortices had stretched further, becoming highly elongated. The vortices ascended and at  $\frac{x}{a_0} = 80$  the filaments had become detached from the primary vortices. Secondary vorticity had formed by  $\frac{x}{a_0} = 16$  and became detached by  $\frac{x}{a_0} = 32$ , however by  $\frac{x}{a_0} = 80$  no detached secondary vorticity was present.

Inspecting Figure 5.50 it can be seen that the path of the vortices in the XY plane is almost linear, with the closest spacing of the vortices was  $2.08a_0$ . The vortices also immediately started to move upwards at this initial spacing, moving upwards by  $6.07a_0$ .

### 5.2.0.5 Counter- Rotating Case 5

Counter-Rotating Case 5 is a simulation of a counter-rotating vortex pair at an initial spacing of  $\frac{a_0}{b_0} = 0.5$  and initial height of  $\frac{h_0}{a_0} = 1.67$ . This is the same spacing as in Co-Rotating Case 5, however the vortices are counter rotating in such a way that the vortices will move towards each other and away from the ground.

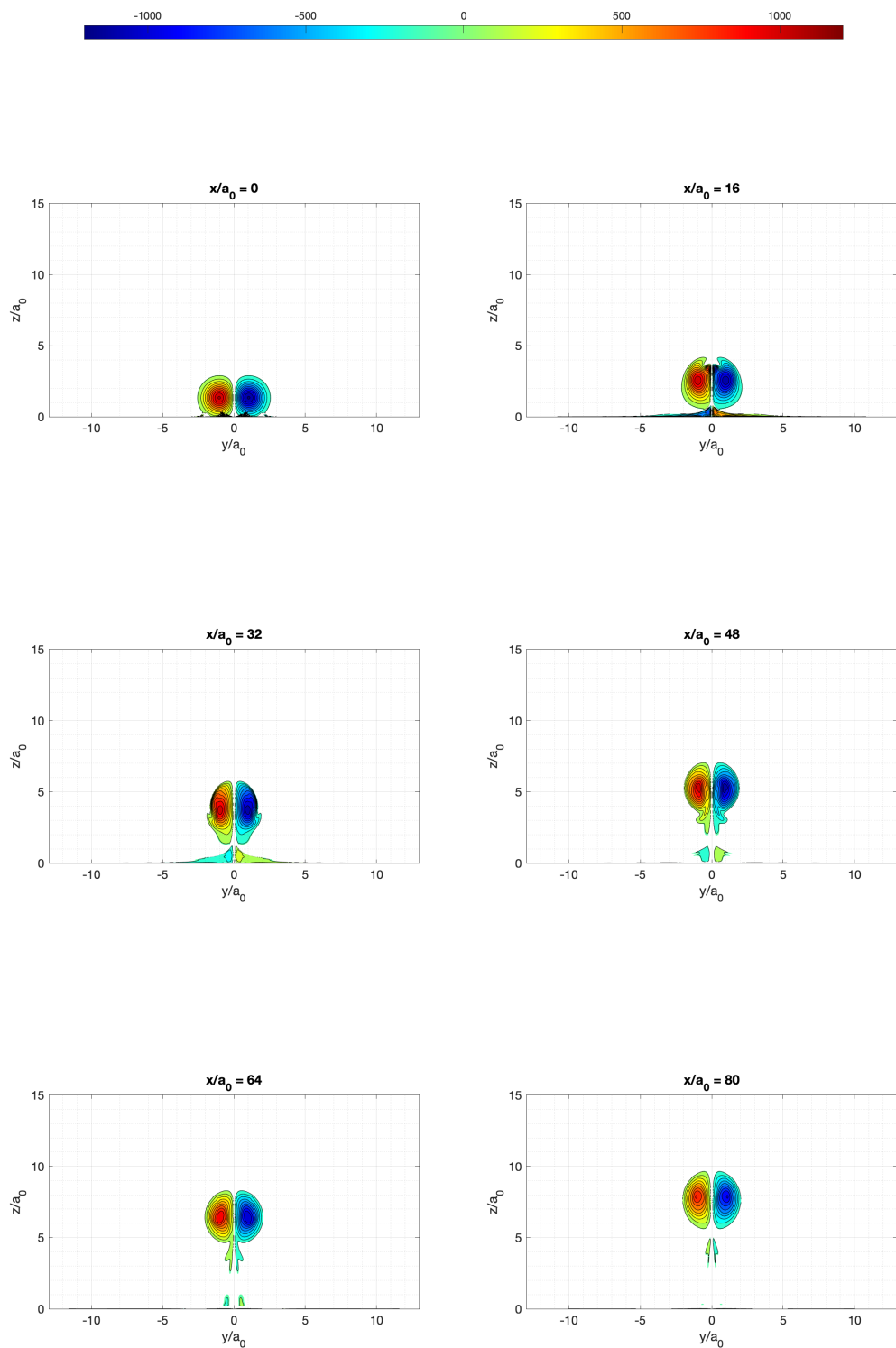


Figure 5.51: Contours of  $\omega_x$  for Counter-Rotating Case 5.

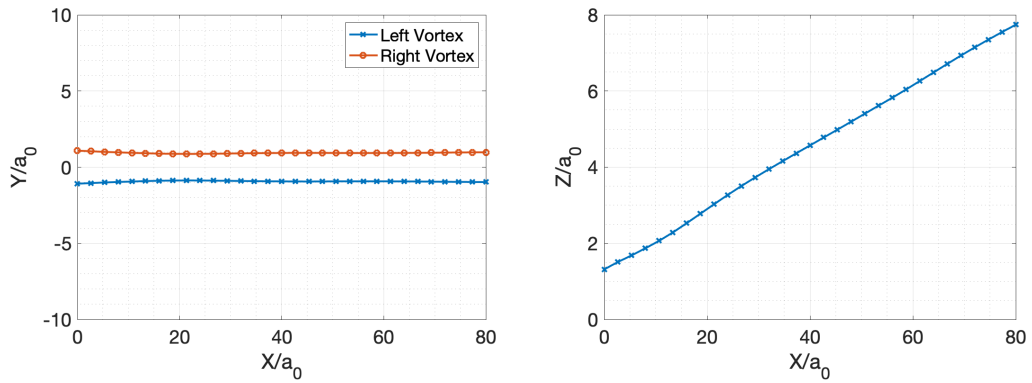


Figure 5.52: Vortex centroids for Counter-Rotating Case 5. The trajectories in the XY plane are shown on the left and in the XZ plane on the right.

Like with Counter-Rotating Case 4 at  $\frac{x}{a_0} = 0$ , which can be seen in Figure 5.51, the vortices are not circular at this close spacing. At  $\frac{x}{a_0} = 16$  the vortices started to stretch and became significantly elongated by  $\frac{x}{a_0} = 32$ . By  $\frac{x}{a_0} = 48$ , the amount of separated secondary vorticity started to decrease and as in Counter-Rotating Case 4, no separated secondary vorticity was visible by  $\frac{x}{a_0} = 80$ .

Like with Counter-Rotating Case 4, the vortices immediately moved upwards, as can be seen in Figure 5.52. As expected at the pair with the closest spacing moved the most vertically, moving by  $6.2a_0$ . The vertical velocity was almost constant. There was almost no lateral movement, with the vortices going from an initial spacing of  $2a_0$  to a final spacing of  $1.95a_0$ .

# Chapter 6

## Discussion

### 6.1 Comparison Between Experimental and Numerical Co-Rotating Cases and Limitations

Although  $Re_T$  is lower for the experimental cases than the numerical simulations, the results show many similarities. Co-Rotating Cases 2 and 4 had the closest  $\frac{a_0}{b_0}$  values, due to the lower  $h_0$  of the experimental cases, it makes the most sense to compare Experimental Cases 1 and 2 to Co-Rotating Cases 1 and 3 respectively, due to the more similar values of  $\frac{h_0}{b_0}$ .

When comparing Experimental Case 1 to Co-Rotating Case 1, it can be seen from the  $\omega_x$  plots (Figures 5.1 and 5.5) that both vortex pairs exhibited similar behaviour. The vortices in both cases stretched parallel to the line between them. Figures 5.2 and 5.6 show that the vortex pairs in both cases shifted laterally (movement in the x-y plane for CFD cases and x-z plane for experimental) and rebounded (movement in the x-z plane for CFD and x-y plane for experimental), the mechanism for which was explained in Chapter 5. The lateral movement exhibited in co-rotating case 1 and experimental case 1 are very similar. The vertical movements of the two cases appear to show some differences, but upon closer inspection, they can also be seen to be similar. Figure 5.6 shows that the vortex pair in co-rotating case 1 initially moved upwards before moving very slightly downwards between  $\frac{X}{a_0} = 21$  and  $\frac{X}{a_0} = 40$ . After this, the vortices moved upwards again. The experimental vortex pair show similar behaviour. This is shown in Figure 5.2, the pair initially moved upwards, then between  $x=3C$  and  $x=4C$ , the vortices moved down by less than

1mm. The downstream positions where this slight downward movement occurred normalised by  $a_0$  are  $\frac{X}{a_0} = 25$  and  $\frac{X}{a_0} = 33.3$ , similar to the locations this occurred in co-rotating case 1. Furthermore, in Experimental Case 1, the vortices behaved like two single vortices, something which was also observed in Co-Rotating Case 1. Further evidence for this can be seen in Figures 6.1 and 6.2, where the separation distances remained almost constant for both cases.

For Experimental Case 2 it can be seen in Figure 5.3 that the vortex which passed closest to the ground merged into the other vortex, merging as if it were an asymmetric vortex pair. This phenomenon is also seen in Co-Rotating Case 3, as well as Co-Rotating Cases 2, 4 and 5. Unlike in the experimental case a very high vortex aspect ratio was seen in the vortex which passed closest to the ground. This is possibly due to the low spatial resolution of the experimental measurement technique. For both cases the separation distance rapidly reduced initially, shown in Figures 6.2 and 6.1, with the vortex pairs of neither case exhibiting signs of being in the first diffusive stage of merging. Figures 5.4 and 5.14 show that a lateral shift, as well as rebound, occurs in both the experimental and numerical cases. Comparing the lateral movements of the two cases they are very similar. In both the experimental case and the numerical case, the vortex which passed closest to the ground shifts more laterally than the other vortex. At  $\frac{x}{a_0} \approx 26$  for co-rotating case 3 and  $X=3C$  ( $\frac{X}{a_0} = 25$ ) for experimental case 2, the vortices crossed over. The vertical movements again look different, but upon closer inspection similarities can be found. In experimental case 2, the left side vortex initially moved upwards and the right side vortex downwards. Then, the left side vortex moved slightly downwards between  $X=3C$  ( $\frac{X}{a_0} = 25$ ) and  $X=4C$  ( $\frac{X}{a_0} = 33.3$ ). The right side vortex moved slightly upwards between  $X=2C$  ( $\frac{X}{a_0} = 16.67$ ) and  $X=4C$  ( $\frac{X}{a_0} = 33.3$ ). A similar trajectory is observed in co-rotating case 3. Again, the left side vortex initially moved upwards and the right side vortex downwards. At approximately  $\frac{x}{a_0} = 30$ , the left side vortex started to move downwards, whilst the right side vortex moved upwards. By  $\frac{x}{a_0} = 35$  the vertical position of the vortices had not crossed over, as is the case at the most downstream measurement plane in experimental case 2. Although the vertical motion of both pairs shows similarities, the movement was more pronounced in co-rotating case 3.

For the numerical investigation of this research the RANS turbulence model was

utilised to investigate the vortex interactions and their evolution downstream. This model used time and Reynolds averaging, as a result transient effects are not included and any subgrid scale eddies are not resolved. However, the evolution of secondary vortices has been addressed subject to this limitation, for example in Figures 5.5, 5.32 and 5.42. As discussed in 3, the secondary vortices were not resolved due to limitations in both the spatial resolution of the pneumatic probe and the lowest height to which it could be traversed. However, the effects of the secondary vortices, such as vortex rebound can be observed in Figures 5.2 and 5.4.

## 6.2 Vortex Merging

As identified by Wang et al [9], the merger of two co-rotating vortices is promoted by the influence of the ground. This can be seen in observing Figures 5.13 and 5.32, the two cases have the same initial spacing but the case with the lower initial height merged within the domain whereas the case with the higher  $h_0$  had not. This promoted merging phenomenon can be seen more clearly in observing the change in vortex separation in Figures 6.1, 6.2, 6.3 and 6.4. It is clear to see that the vortex pairs closer to the ground more rapidly move together.

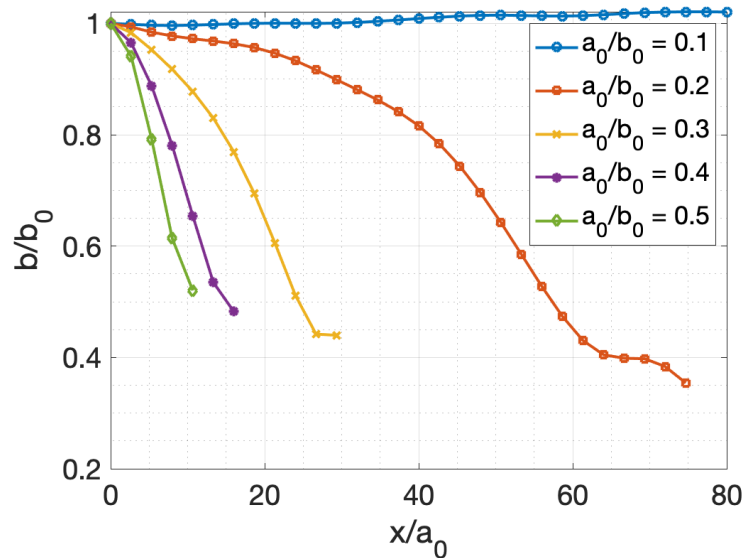


Figure 6.1: The change in vortex separation for vortex pairs at the same initial height,  $\frac{h_0}{a_0} = 1.667$  but varying initial spacings.

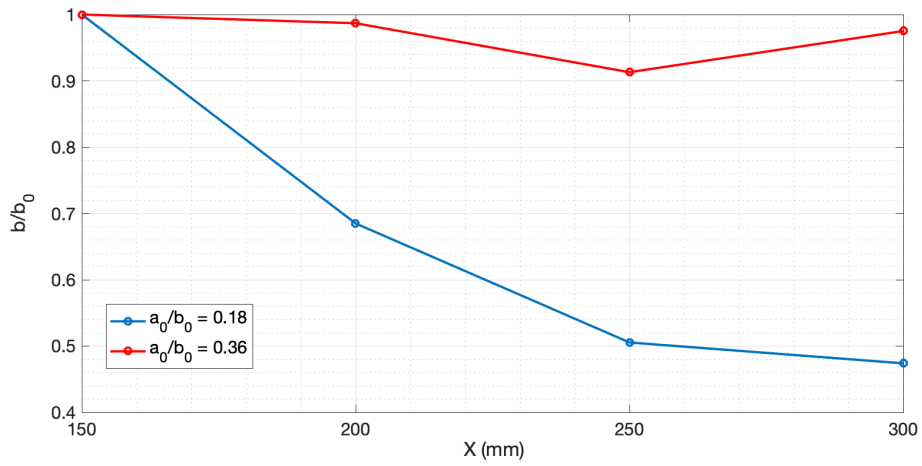


Figure 6.2: The change in vortex separation for the experimental cases, which had an initial height of  $\frac{h_0}{a_0} = 1.73$  and initial spacings of  $\frac{a_0}{b_0} = 0.12$  and  $\frac{a_0}{b_0} = 0.32$  respectively.

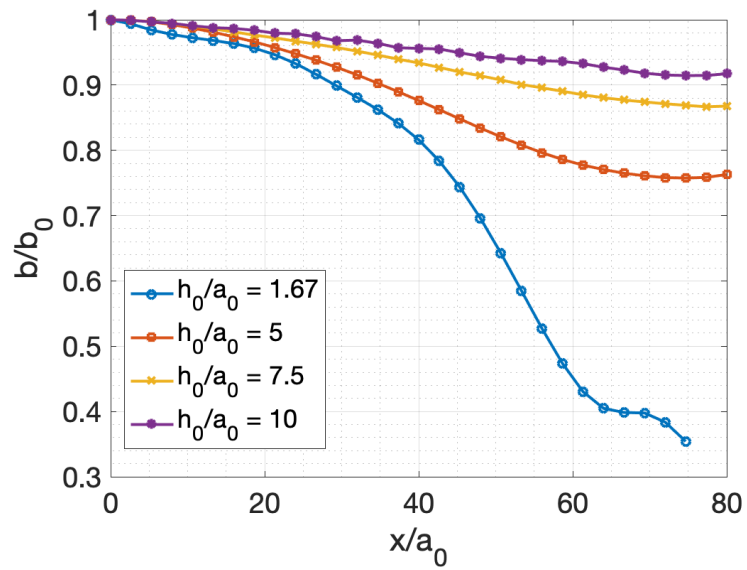


Figure 6.3: The change in vortex separation for vortex pairs at the same initial spacing,  $\frac{a_0}{b_0} = 0.2$ , but varying initial heights.

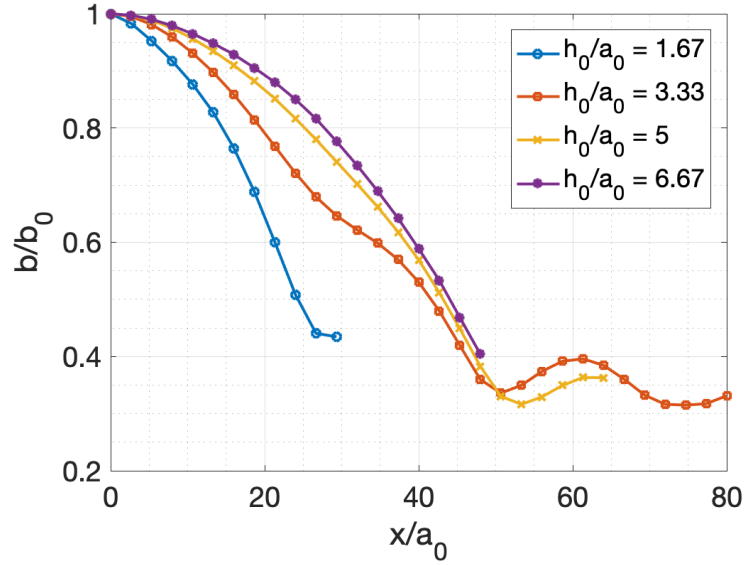


Figure 6.4: The change in vortex separation for vortex pairs at the same initial spacing,  $\frac{a_0}{b_0} = 0.3$ , but varying initial heights.

As discussed in Chapter 2, Wang et al. concluded that merging was promoted due to the image vortices and secondary vortices. This is supported by comparing Co-Rotating Cases 9, 10 and 11 (Figures 5.32, 5.35 and 5.38). As the initial height of the vortex pair decreases the separation decreases more quickly. Also with decreasing height above the ground, there are increases in induced lateral and vertical velocities, as evidenced by the increased lateral and vertical movement of the vortex pair of Co-Rotating Case 9 compared to Case 10, shown in Figures 5.33 and 5.36. Wang et al. [9] also suggested that when the angle of orientation,  $\theta$ , of the vortex pair was  $90^\circ \leq \theta \leq 180^\circ$  the image vortices delayed merger by slowing the rate of decrease in separation distance. This is because in this orientation the vortex closest to the ground, thus experiencing the greater induced lateral velocity, will move away from the other vortex. This is shown schematically in Figure 6.5 (b), where the vortex closest to the ground is closer to its image vortex. This means that the lateral spacing of the vortices will increase. This effect can be seen in Figure 6.4 for the vortex pair with  $\frac{h_0}{b_0} = 3.33$ , at  $\frac{x}{a_0} \approx 30$  there is a decrease in the rate at which the vortices approach each other. This  $\frac{x}{a_0}$  corresponds at an angle of orientation of  $\theta = 90^\circ$ , shown in Figure 5.34. When the angle of orientation is  $0^\circ \leq \theta \leq 90^\circ$ , the lateral velocities resulting from the image vortices will cause the separation distance to reduce, as in this orientation the vortex closest to the ground is on the left, when

the lateral movement is moving the vortices to the right.

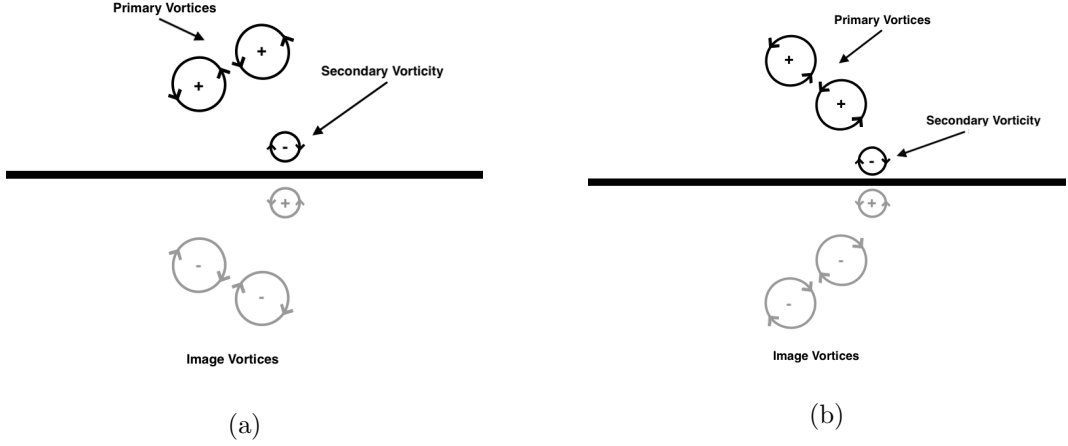


Figure 6.5: A schematic of a co-rotating vortex pair with an angle of orientation of (a)  $0 \leq \theta \leq 90^\circ$  and (b)  $90^\circ \leq \theta \leq 180^\circ$ .

The same trend is seen in Co-Rotating Cases 6, 7 and 8 (Figures 5.22, 5.26 and 5.29). Although these cases do not enter the convective stage of merging, which can be seen in both the  $\omega_x$  contour plots, as no filaments form, and Figure 6.3 where there is no rapid reduction in b. Despite this, the vortex pairs with lower  $h_0$  still show a greater reduction in separation distance. As the vortex pairs did not enter the convective stage of merging this reduction in b can not be due to antisymmetric vorticity. Antisymmetric  $\omega_x$  was shown by Cerretelli and Williamson [17] to be the cause of the reduction in b during the convective stage of merging. Thus, this reduction in b must be due to the induced lateral and vertical velocities.

The effect of the secondary vorticity can be seen by comparing Co-Rotating Case 6 to Cases 7 and 8, only in Case 6 does secondary vorticity separate from the ground. and that case has a reduction in b of 24% compared to 13% and 8% for Cases 7 and 8 respectively. The ground effect also modifies the first diffusive stage of merging. For an out of ground effect vortex pair the separation remains constant or close to constant throughout the first diffusive stage [17], but for the in ground effect pairs even during this stage b reduces, as shown in Figure 6.3.

As well as the induced lateral and vertical velocities promoting vortex merging of co-rotating vortex pairs in ground effect, there is also an increase in the length of the filaments that form in the vortex which passes closest to the ground. This suggests an increased amount of antisymmetric  $\omega_x$ , which was shown to be the reason

the vortices move towards each other during the convective stage of merging [17]. Cerretelli and Williamson split the total  $\omega_x$  in symmetric and antisymmetric  $\omega_x$  by making the total  $\omega_x$  skew-symmetric. As the vortex pair becomes asymmetric due to the interaction with the ground it is not possible to make  $\omega_x$  skew-symmetric. As such the vorticity which is advected outside of the core region was integrated between  $\frac{x}{a_0} = 32$  and  $\frac{x}{a_0} = 64$  for Co-Rotating Cases 9, 10 and 11 and is presented in Figure 6.6. The core region was defined by the contour line at  $e^{-1}$  of the peak in plane  $\omega_x$ . These streamwise locations were chosen as it can be seen from Figures 5.32, 5.35 and 5.38 that filaments had formed at those locations. This shows that there is an increase in  $\omega_x$  outside of the core region which suggests there is also a greater amount of antisymmetric  $\omega_x$  as  $h_0$  decreases. This, as well as the effect of secondary vorticity explains the more rapid movement of the vortices towards each other as the height above the ground decreases.

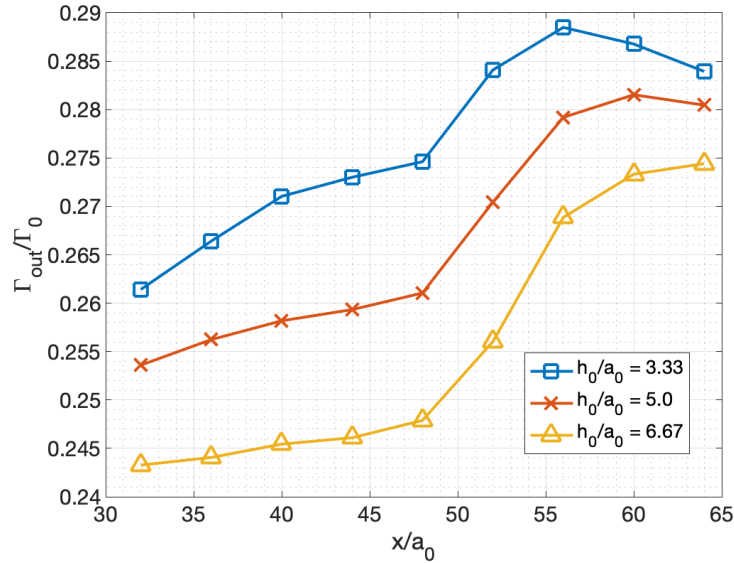


Figure 6.6: The circulation outside of the core region for vortex pairs at the same initial spacing of  $\frac{a_0}{b_0} = 0.3$ , but varying initial heights.

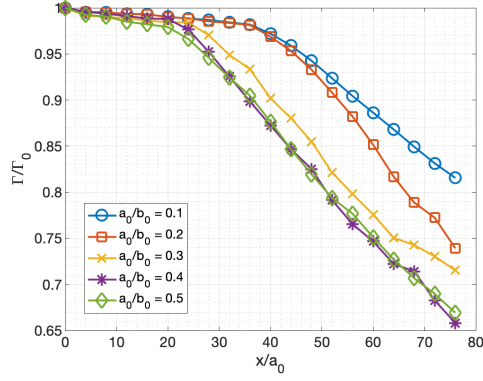
For the vortex pairs with the lowest initial heights Co-Rotating Cases 3, 4 and 5 merge within the domain. Whilst Case 1 sees no reduction in  $b$  and Case 2 enters the convective stage of merging. Cases 3, 4 and 5 has close enough initial spacings that they immediately start to rapidly move together where in Case 2 the vortices initially slowly move together before  $b$  rapidly reduces. At the low initial height of  $\frac{h_0}{a_0} = 1.67$ ,

when the vortices start to rotate around each other, the vortex which passes closest to the ground becomes partially strained. Due to this, the initially symmetric vortex pair become asymmetric, which is why the merging differs significantly from the cases with a higher  $h_0$ . The merger of the vortices show similarities to the simulations of Brandt and Nomura [19] for vortex pairs with circulation ratios of 0.9 and 0.8, despite the vortices being initially equal.

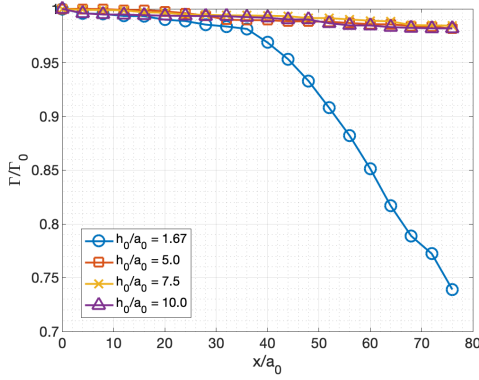
## 6.3 Decay of Circulation

### 6.3.1 Co-Rotating Pairs

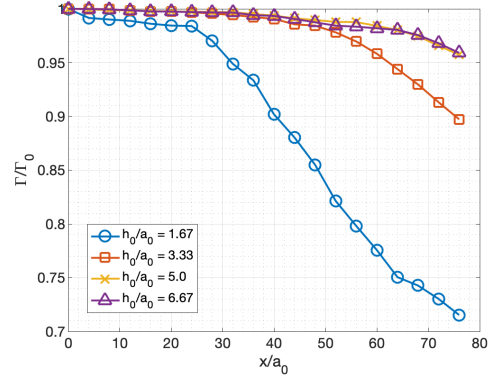
It can be seen in Figures 6.7 that for the vortex pairs at low initial heights there is a sudden and fast decay of circulation. The circulation was calculated using 3.8. This trend in circulation decay varies significantly from the decay seen in the investigations of co-rotating vortex pairs out of ground effect undertaken by Cerretelli and Williamson [17]. A similar decay trend was seen in the experimental work of Wang et al. [9], who suggested the commencement of the rapid decay was due to the onset of vortex merging, when  $\omega_x$  is advected out of the inner core region to the outer core region and is no longer included in calculations of vortex  $\Gamma$ . From Figure 6.7 (a) it can be seen that this sudden and rapid decrease in  $\Gamma$  occurs even in the vortex pair with  $h_0 = 1.67$  and  $\frac{a_0}{b_0} = 0.1$ , which sees no decrease in  $b$  (Figure 6.1), and therefore had not entered the convective stage of merging. Furthermore, in Figure 6.7 C the rapid decrease in  $\Gamma$  is only observed in the vortex pairs at initial heights of  $\frac{h_0}{a_0} = 1.67$  and  $\frac{h_0}{a_0} = 3.33$  but all vortex pairs with spacing of  $\frac{a_0}{b_0} = 0.3$  entered the convective stage of merging. From this it can be concluded that there must be other factors causing the observed decay of  $\Gamma$ .



(a)



(b)



(c)

Figure 6.7: Circulation for: (a) vortex pairs at multiple spacings and an initial height of  $\frac{h_0}{a_0} = 1.67$  (b) vortex pairs at an initial spacing of  $\frac{a_0}{b_0} = 0.2$  and multiple heights and (c) vortex pairs at an initial spacing of  $\frac{a_0}{b_0} = 0.3$  and multiple heights.

It was found by Stephan et al. [81] and Holzapfel et al. [82] that the interaction between secondary vorticity and primary vortices, which causes turbulence and annihilation of vorticity, resulting in the decay of primary vortex  $\Gamma$ . The vortex pairs which do not exhibit rapid decay of  $\Gamma$  also do not experience any significant interaction with secondary vorticity. This can be seen qualitatively in Figures 5.22, 5.26, 5.29, 5.35 and 5.38, as no secondary vorticity separates from the ground and subsequently interacts with the primary vortices. Further evidence of this can be seen in Figure 6.9 where there is less secondary circulation produced in the cases with higher initial heights.

In order to quantify the interaction between the primary vortices and secondary

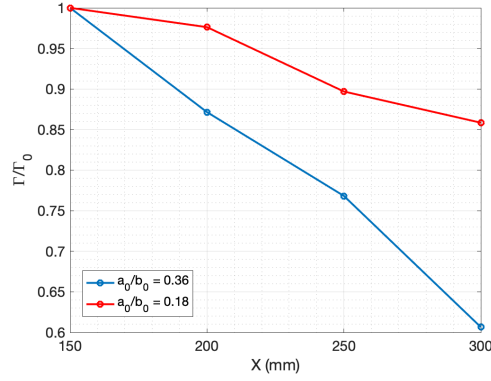


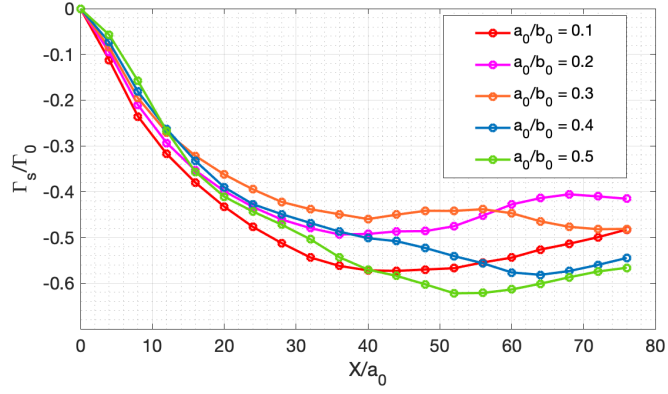
Figure 6.8: Circulation for the Experimental Co-Rotating Vortex Pairs at initial spacings of:  $\frac{a_0}{b_0} = 0.12$  and  $\frac{a_0}{b_0} = 0.32$

vorticity, in plane turbulent kinetic energy,  $k$ , has been integrated at multiple downstream locations. Turbulent kinetic energy is generated due to the shear at the ground but also due to the interaction between the primary and secondary vortices. Figures 6.10 B and C show that for the case in which no secondary vorticity separated from the ground and no rapid decay of  $\Gamma$  occurred, there is no significant increase in  $k$ . This suggests that the interaction between the primary vortices and secondary vorticity is the reason for the decay of  $\Gamma$ .

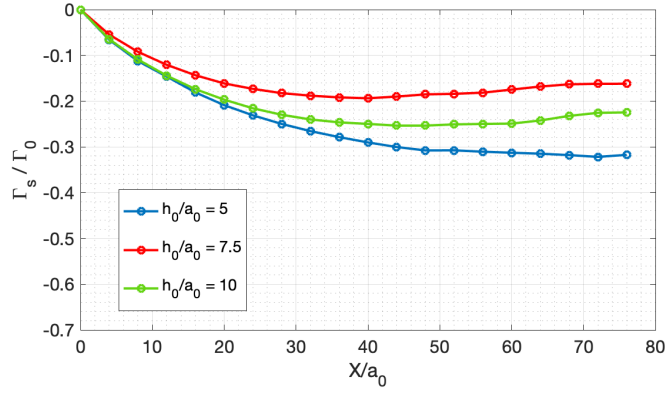
The variation in initial septation changes the streamwise location at which the rapid decay of circulation commences, as shown by Figure 6.7 (a). The two cases with the largest spacings, Co-Rotating Cases 1 and 2, the rapid decay begins at around  $\frac{x}{a_0} \approx 36$ , with Case 2 decaying more from that point onwards. The other cases with an initial height of  $\frac{h_0}{a_0} = 1.67$  begin to decay rapidly at approximately  $\frac{x}{a_0} \approx 20$ . A similar decay pattern can be seen in the experimental cases (Figure 6.8), where the vortex pair with the largest separation, ( $\frac{a_0}{b_0} = 0.12$ ) which does not enter the convective stage of merging, sees a rapid decrease in circulation after  $x = 200\text{mm}$ . Whereas the experimental case with a closer initial spacing,  $\frac{a_0}{b_0} = 0.32$ , rapidly decays from  $x = 150\text{mm}$ . From the  $\omega_x$  contour plots in Chapter 5, it is clear that as the initial spacing decreased the secondary vorticity wrapped further around the primary vortices. Stephan et al [81] found that for a counter rotating vortex pair in ground effect, the wrapping around of secondary vorticity caused the rapid decay of the primary vortices. Figure 6.10 (a) shows there is an increase in turbulent kinetic energy,  $k$ , and the increase in  $k$  coincides with the beginning of the

rapid decay of  $\Gamma$  for those cases.

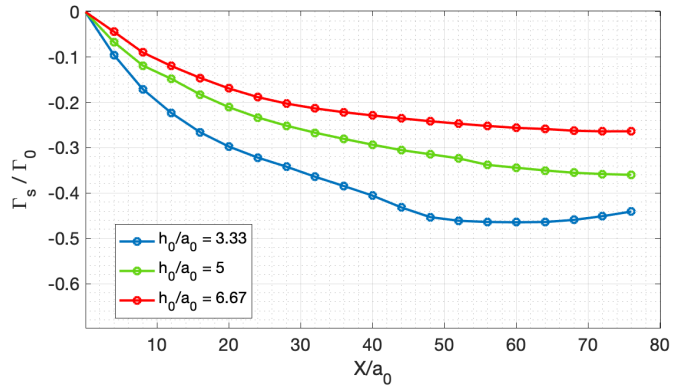
The difference in decay of  $\Gamma$  plots between the in of ground effect co-rotating pairs studied in this thesis and out ground effect pairs, such as in the research of Cerretelli and Williamson [17], can be explained by the interaction between primary and secondary vortices. As discussed in this section, when a co-rotating pair is close to a solid surface, secondary vortices will form and wrap around the primary vortices. Turbulent kinetic energy is generated by this interaction between primary and secondary vortices. Stephan et al. and Holzapfel et al. [81, 82] showed that this leads to rapid decay of  $\Gamma$ . Where as for a co-rotating pair out of ground effect, no secondary vortices form, thus the decay of  $\Gamma$  for such a pair does not see a sudden and rapid decrease in  $\Gamma$ . The decay plots of co-rotating cases 7 and 8 are similar to the decay trend of an out of ground effect pair, as can be seen in Figure 6.7 (b). This is because the  $h_0$  of those pairs were far enough from the ground that no secondary vortices wrapped around the primary vortices. This can be seen quantitatively in Figures 5.26 and 5.29 and quantitatively in Figure 6.9 (b).



(a)



(b)



(c)

Figure 6.9: Secondary Circulation for: (a) vortex pairs at multiple spacings and an initial height of  $\frac{h_0}{a_0} = 1.67$  (b) vortex pairs at an initial spacing of  $\frac{a_0}{b_0} = 0.2$  and multiple heights and (c) vortex pairs at an initial spacing of  $\frac{a_0}{b_0} = 0.3$  and multiple heights.

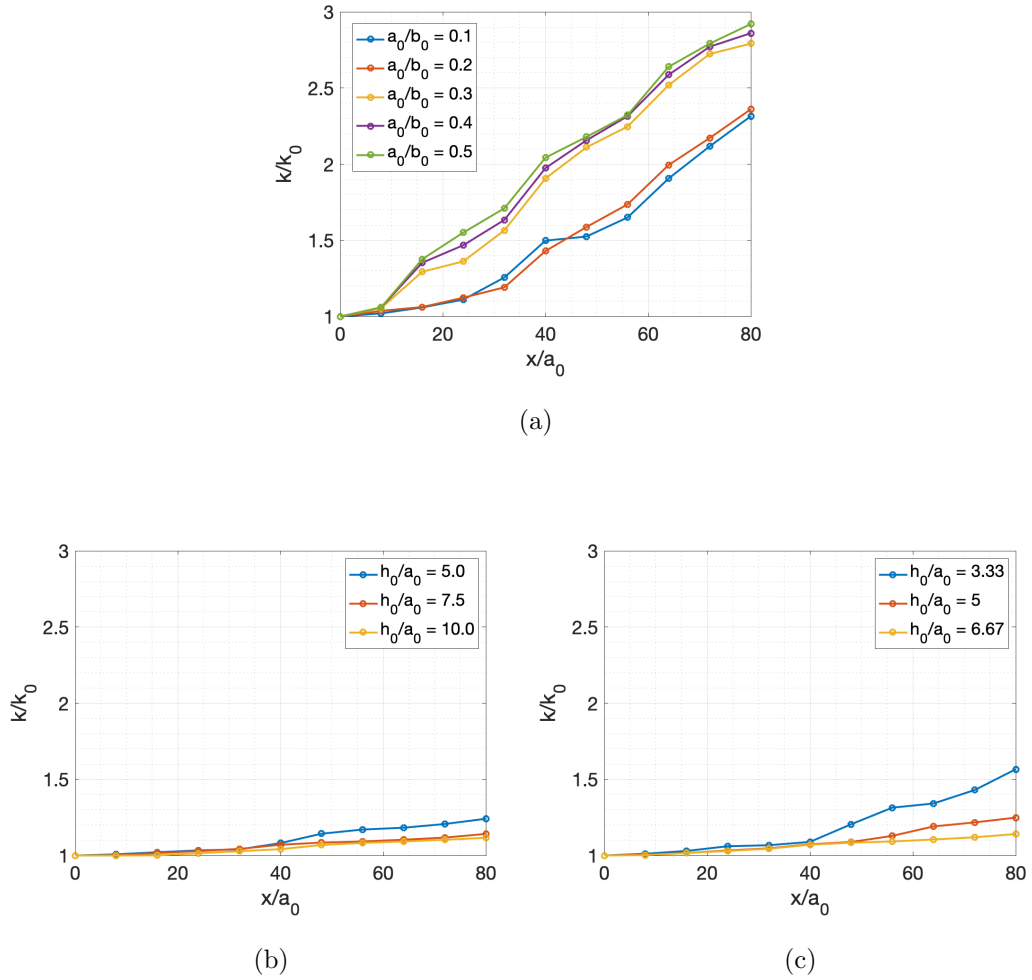


Figure 6.10: Turbulent kinetic energy for: (a) vortex pairs at multiple spacings and an initial height of  $\frac{h_0}{a_0} = 1.67$  (b) vortex pairs at an initial spacing of  $\frac{a_0}{b_0} = 0.2$  and multiple heights and (c) vortex pairs at an initial spacing of  $\frac{a_0}{b_0} = 0.3$  and multiple heights.

### 6.3.2 Counter-Rotating Pairs

The decay of  $\Gamma$  for counter-rotating vortex pairs at multiple initial spacings are presented in Figure 6.11. To calculate this, the plane was split down the line of symmetry between the vortex pair. The positive  $\omega_x$  of the left side of the plane and the negative  $\omega_x$  were integrated, the modulus of the right side circulation was taken. The left and right circulations were then summed to give the total in-plane circulation for the counter-rotating vortex pair. As the initial spacing increases the final circulation value decreases. The only case which shows significant decay of  $\Gamma$  is Counter-Rotating Case 1. This is because Case 1 is the only vortex pair which

interacted significantly with secondary vorticity, as it remained closer to the ground than the vortex pairs of the other cases. Figure 6.12 shows that in Counter-Rotating Case 1 the peak secondary circulation,  $\Gamma_s$ , is 29% greater than Counter-Rotating Case 2, which produced the second most secondary circulation. It is also clear from the  $\omega_x$  contour plots, presented in Chapter 5 (Figures 5.42), that at  $\frac{x}{a_0} = 48$  the secondary vorticity separated from the ground starts to wrap around the primary vortices. Thus,  $\Gamma$  decays due to the mechanism presented by Stephan et al. [81]. It is also clear from the  $\omega_x$  contour plots that this does not occur in any of the other Counter-Rotating Cases. Weaker secondary vorticity is generated as the initial spacing reduces as the vortex pair more quickly move away from the wall due to the increased vertical velocity they induce upon each other as the vortices are closer together.

When compared to the co-rotating cases at the same initial height, the counter-rotating circulation decays much less throughout the domain. This is due to the reduced interaction with secondary vorticity when compared to the co-rotating cases. In all co-rotating cases with an initial height of  $\frac{h_0}{a_0} = 1.67$  the secondary vorticity wraps around the primary vortices, however that only occurred in Counter-Rotating Case 1.

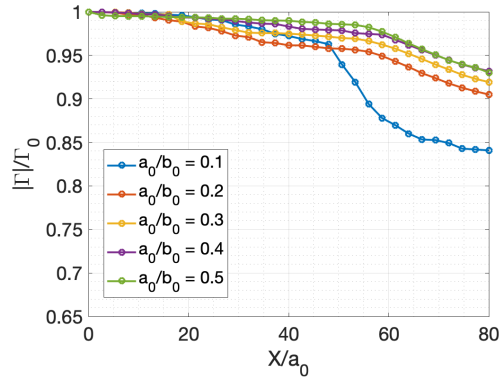


Figure 6.11: The circulation at multiple downstream locations for counter-rotating pairs at multiple initial spacings and an initial height of  $\frac{h_0}{a_0} = 1.67$ .

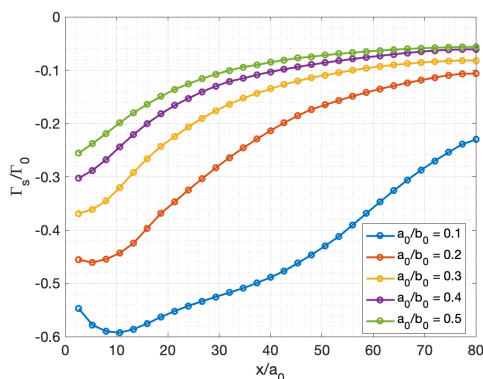


Figure 6.12: The circulation of secondary vorticity at multiple downstream locations for counter-rotating pairs at multiple initial spacings and an initial height of  $\frac{h_0}{a_0} = 1.67$ .

## 6.4 Vortex Pair Trajectories

### 6.4.1 Co-Rotating Pairs

As expected as the initial height was reduced the lateral movement of the vortex pair increased. Co-Rotating Cases 6, 7 and 8 moved by  $6.4a_0$ ,  $4.3a_0$  and  $3.67a_0$  respectively, as can be seen in Figures 5.23, 5.27 and 5.30. As found by Wang et al. [9] vortex rebound occurs in co-rotating vortex pairs in ground effect. Like with counter-rotating pairs this is due to the separation of secondary vorticity from the ground. This can be seen by comparing the vertical motion of the vortices in Co-Rotating Cases 3 and 11. The initial spacing is the same, but Case 3 is at a lower initial height. No secondary vorticity separates from the ground in Case 11 where it does in Case 3 and Case 3 moves vertically approximately 5 times more than in Case 11, which can be seen by comparing Figure 5.14 to Figure 5.39.

As seen in Chapter 5 the ground effect also influences the rotation of the vortex pair. Wang et al. [9] found that ground effect increased the rate of rotation of the vortex pair. The results of Co-Rotating Cases 6, 7, 8, 9, 10 and 11 support this (Figures 5.24, 5.28, 5.31, 5.34, 5.37 and 5.40). However, at the lowest initial heights the presence of the ground inhibits this rotation. This is most prominent in Co-Rotating Cases 1 and 12. There is no change in angle of orientation in Co-Rotating Case 1 and little change in orientation angle in Experimental Case 1. For Co-Rotating Cases 2, 3 and 4, the rotation is initially suppressed before

rapidly increase as the vortex which passes closest to the ground wraps around and merges into the other. This is shown in Figures 5.11, 5.15 and 5.18.

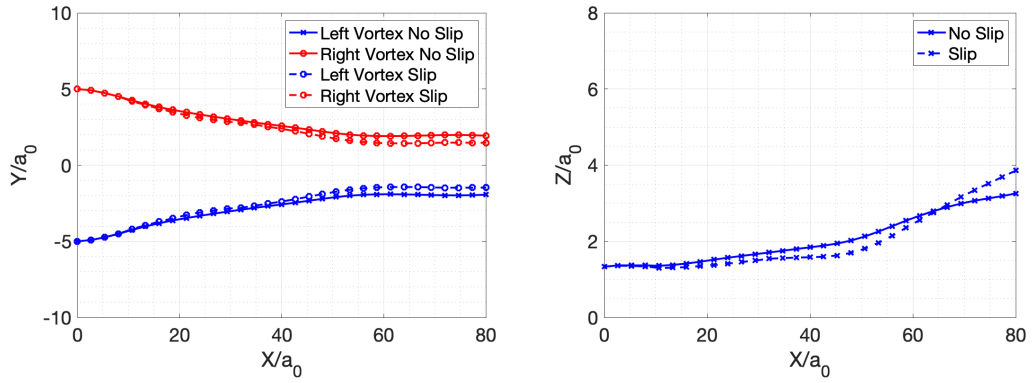
### 6.4.2 Counter-Rotating Pairs

The paths of the counter-rotating vortices, shown in Chapter 5, in the vertical direction can be grouped into three categories. Counter-Rotating Case 1 in which the pair remained at an almost constant height above the ground before moving upwards, as shown in Figure 5.43. Counter-Rotating Cases 2 and 3, which remained at an almost constant height above the ground for a short distance downstream (around  $15a_0$ ) before moving upwards at a constant rate, as seen in Figures 5.46 and 5.48. Finally, Counter-Rotating Cases 4 and 5, which moved upwards at an almost constant rate immediately, shown in Figures 5.50 and 5.52. Co-Rotating Cases 4 and 5 moved vertically around 3 times more than Co-Rotating Case 1.

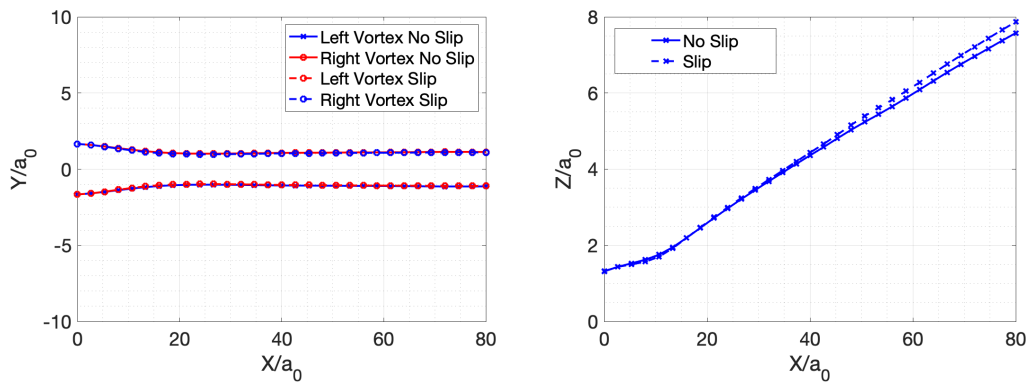
As the vortices move towards each other due to the velocity induced upon each vortex due to the ground, the spacing between the vortices reduces. The final spacing of the vortices is related to the initial spacing. Counter-Rotating Case 1 has a final spacing 2 times greater than that of Counter-Rotating Case 5. This occurs as once the vortices are close enough to induce a vertical velocity upon each other the pair moves away from the ground. As a result the induced lateral velocity reduces until it becomes 0. At which point the vortices are out of ground effect and no longer move towards each other.

It has been shown that for a counter-rotating vortex pair in which the induced velocity results in a downward movement of the pair, the secondary vortices which form due to the interaction with the ground significantly alter the trajectories of the vortices when compared to a slip wall [28, 26, 27, 25]. As presented in Chapter 5 and as shown by Wang et al. [9], secondary vorticity significantly affects the dynamics of co-rotating vortex pairs in ground effect. However, little research exists on the effect of counter-rotating vortex pairs in which the induced velocity moves the pair away from the ground, this configuration is shown in Figure 5.41. In order to determine the effect of the secondary vortices on the trajectory of such counter-rotating vortices simulations with a slip condition applied to the ground were completed for comparison to the simulations with the no-slip condition applied to the ground.

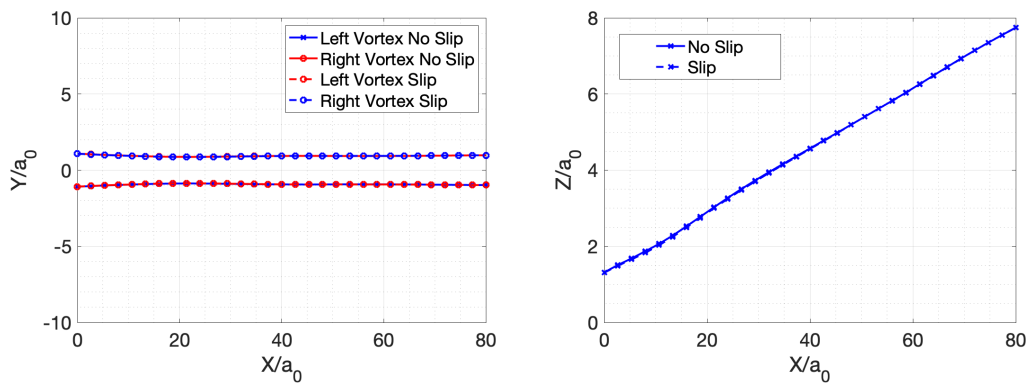
It is clear from Figure 6.13 that in this configuration the secondary vortices have significantly less impact on the dynamics of the pair than that of a counter-rotating vortex pair which moves downwards. It can be seen that at the closest spacing, the secondary vorticity has no effect on the trajectory of the vortex pair. A negligible difference in vertical trajectory between the case with a spacing of  $\frac{a_0}{b_0} = 0.3$  when comparing the simulations with a slip and no-slip condition applied to the ground. At the largest spacing of  $\frac{a_0}{b_0} = 0.1$  the secondary vorticity has more effect on the trajectory. The secondary vorticity has the effect of reducing the lateral velocity of the primary vortices as the velocity induced by the secondary vorticity is in the opposite direction to that of the primary vortices. This results in a closer final spacing of the primary vortices in the simulation with a slip wall. The secondary vorticity also initially increases the vertical velocity of the primary vortices, as shown in Figure 6.13, due to vortex rebound described in [28, 26, 27, 25]. However, the final height of the vortex pair is lower in the simulation with a no slip wall as the final spacing is wider, thus the vertical velocity induced by the primary vortices is lower. As the primary vortices are much stronger than the secondary vortices, any velocity they induce upon each other is much greater than the velocity induced by the secondary vortices on the primary.



(a)



(b)



(c)

Figure 6.13: The trajectories counter-rotating vortices for simulation with a no slip condition applied to the ground and a slip condition applied to the ground. The initial spacings of the vortex pairs are: (a)  $\frac{a_0}{b_0} = 0.1$ , (b)  $\frac{a_0}{b_0} = 0.3$  (c)  $\frac{a_0}{b_0} = 0.5$

## Chapter 7

# Conclusions and Future Work

### 7.1 Conclusions

The work presented has investigated both co-rotating and counter-rotating vortex pairs using a mixture of experimental methods and numerical methods. A five hole pneumatic pressure probe was used to take pressure measurements within a wind tunnel with two NACA0012 vortex generators used to generate the vortices close to a flat plate. Simulations utilising RANS modelling were performed for co-rotating and counter-rotating vortex pairs at multiple initial spacings and heights. The counter-rotating vortex pairs studied had a mutually induced velocity which moved away from the flat plate. Little research exists on vortex pairs with such a configuration, they occur in the wakes of race car front and rear wings and in the rear diffuser and around the bargeboard area of race cars [8, 2, 1]. The  $k-\omega$  SST turbulence model was used for the simulations and this was chosen as it has been shown to match well to experiments for similar flows [62].

Despite the difference in  $Re_T$  between the experiments and the simulations, the two matched well. For both Experimental Case 1, which had the widest initial spacing of the experimental cases, and Co-Rotating Case 1, the two vortices did not interact. The separation distance remained almost constant for both at all downstream locations analysed. The vortices in both cases also exhibited similar deformations, although lower vortex aspect ratios were seen in the experimental case. This is possibly due to the low spatial resolution of the experimental measurement technique. In Experimental Case 2 and Co-Rotating Case 3, a similar merging pattern was observed. The vortex which passed closest to the ground became

partially strained and then started to merge into the other vortex. Although, the very high vortex aspect ratio observed in the numerical simulation was not seen in the experiment.

It was found from both experiments and simulations that an initially equal strength co-rotating vortex pair very close to the ground will merge like an asymmetric vortex pair. This is due to the vortex which passes closest to the ground becoming partially strained as it moves between the ground plane and the other vortex. This vortex will then merge into the other. As found by Wang et al. [9], merging was found to be promoted by the ground effect. The rate at which separation distance decreased was found to increase with decreasing initial height. The conclusions of Wang et. [9] are supported by this work, as image vortices and secondary vorticity results in the faster movement of the vortices towards each other. It was also found that, the vortex pairs that are closer to the ground had longer filaments, which means an increased amount of antisymmetric  $\omega_x$ , which further increases the rate at which the vortices move towards each other.

The decay of  $\Gamma$  was found to be accelerated by the generation of secondary vorticity and the subsequent interaction of the primary vortices with this secondary vorticity. The interaction of the secondary vorticity with the primary vortices causes turbulence, shown by the increase in turbulent kinetic energy, which results in annihilation of  $\omega_x$ . It was found that as the initial height of the co-rotating cases increased the rate of decay of  $\Gamma$  decreased, due to less interaction of primary vortices with secondary vortices and well as weaker secondary vorticity being generated. For the counter-rotating cases investigated, it was found that only the widest spacing case showed a significant decrease in  $\Gamma$ . This is due to the mutually induced vertical velocity moving the vortices away from the ground, thus limiting their interaction with secondary vorticity.

Lateral movement and rebound were observed in the co-rotating vortex pairs both in the experimental work and the numerical work. These movements were greater as the initial height of the vortex pair decreased, due to the stronger interaction of primary vortices with their image vortices and the secondary vorticity. It was also found from the simulations that the ground effect increased the rotational rate of the co-rotating pairs, as identified by Wang et al. [9]. However, at the lowest initial heights, as well as in the experimental work, the presence of the ground initially

inhibited the rotation of the pair, before then rapidly increasing as the vortex which passes closest to the ground then merges into the other.

The counter-rotating vortex pairs moved both laterally and vertically. However, the trajectories of the counter-rotating pairs investigated in this work were not significantly affected by the secondary vorticity. This was shown by comparing simulations where the ground was modelled as a no slip and slip wall respectively. This was due to the mutually induced vertical velocity moving the pair away from the ground, this resulting in both weaker secondary vorticity being generated and less interaction of primary vortices with the secondary vorticity. This is significantly different than counter-rotating pairs whose mutually induced velocity moves the pair towards the ground.

## 7.2 Future Work

The following areas have been identified as possible areas of further work regarding vortex interactions in ground effect.

Experiments at  $Re_\Gamma$  similar to that of the numerical simulations presented in this thesis would be of interest. In the numerical co-rotating cases where merging occurs, very high aspect ratios can be seen in the vortex which passes closest to the ground. This would allow it to be ascertained if this also occurs during experiments.

Experiments which use a measurement technique with a higher spatial resolution than in this research, such as particle image velocimetry, would be of interest. This would allow secondary vortices to be captured and their interaction with primary vortices could be better analysed. Furthermore, this would also allow any transient effects to be observed.

As this research used a RANS turbulence model for numerical work, numerical investigations using large eddy simulations (LES) would be of interest. This would allow transient effects to be analysed and some eddies not resolved in the RANS simulations to be resolved. Alternatively, direct numerical simulations (DNS) could be undertaken, this would allow the eddies down to the Kolmogorov scale to be resolved. However, due to the computational expense of such simulations,  $Re_\Gamma$  would have to be lower than in the RANS simulations.

A study of unequal strength co-rotating pairs would also be of interest. In both

the experimental work and numerical work at the lowest  $h_0$  it was seen that pair merged like an unequal strength pair. It was shown by Brandt and Nomura and Dritschel and Waugh [19, 20] that unequal strength pairs have significantly different merging than equal strength pairs. It was also shown that the circulation ratio ( $\frac{\Gamma_2}{\Gamma_1}$ ) affects the type of merging that occurs in unequal pairs, as discussed in 2. From such research, it could be discovered if proximity to the ground affects the type of merging that occurs for a given circulation ratio.

# Bibliography

- [1] M. Nakagawa, S. Kallweit, F. Michaux, and T. Hojo, “Typical Velocity Fields and Vortical Structures around a Formula One Car, based on Experimental Investigations using Particle Image Velocimetry,” *SAE International Journal of Passenger Cars - Mechanical Systems*, vol. 9, pp. 754–771, Apr. 2016.
- [2] X. Zhang, W. Toet, and J. Zerihan, “Ground Effect Aerodynamics of Race Cars,” *Applied Mechanics Reviews*, vol. 59, pp. 33–49, Jan. 2006.
- [3] T. R. Quackenbush, A. J. Bilanin, and R. M. McKillip, Jr., “Vortex wake control via smart structures technology,” (San Diego, CA), pp. 78–92, May 1996.
- [4] T. R. Quackenbush, A. J. Bilanin, and B. F. Carpenter, “Test results for an SMA-actuated vortex wake control system,” (Newport Beach, CA), pp. 84–94, July 1999.
- [5] M. Gad-el Hak, *Flow Control: Passive, Active, and Reactive Flow Management*. Cambridge University Press, 1 ed., Aug. 2000.
- [6] P. R. Spalart, “AIRPLANE TRAILING VORTICES,” *Annual Review of Fluid Mechanics*, vol. 30, pp. 107–138, Jan. 1998.
- [7] D. Fabre and L. Jacquin, “Stability of a four-vortex aircraft wake model,” *Physics of Fluids*, vol. 12, no. 10, p. 2438, 2000.
- [8] J. Katz, *Race car aerodynamics: designing for speed*. Cambridge, MA, USA: R. Bentley, 1995.
- [9] Y. Wang, P. Liu, T. Hu, and Q. Qu, “Investigation of co-rotating vortex merger in ground proximity,” *Aerospace Science and Technology*, vol. 53, pp. 116–127, June 2016.

- [10] T. Leweke, S. Le Dizès, and C. H. Williamson, “Dynamics and Instabilities of Vortex Pairs,” *Annual Review of Fluid Mechanics*, vol. 48, pp. 507–541, Jan. 2016.
- [11] P. G. Saffman and R. Szeto, “Equilibrium shapes of a pair of equal uniform vortices,” *Physics of Fluids*, vol. 23, no. 12, p. 2339, 1980.
- [12] D. G. Dritschel, “The stability and energetics of corotating uniform vortices,” *Journal of Fluid Mechanics*, vol. 157, pp. 95–134, Aug. 1985.
- [13] D. G. Dritschel, “The nonlinear evolution of rotating configurations of uniform vorticity,” *Journal of Fluid Mechanics*, vol. 172, p. 157, Nov. 1986.
- [14] P. Meunier, U. Ehrenstein, T. Leweke, and M. Rossi, “A merging criterion for two-dimensional co-rotating vortices,” *Physics of Fluids*, vol. 14, pp. 2757–2766, Aug. 2002.
- [15] M. V. Melander, N. J. Zabusky, and J. C. McWilliams, “Symmetric vortex merger in two dimensions: causes and conditions,” *Journal of Fluid Mechanics*, vol. 195, p. 303, Oct. 1988.
- [16] P. Meunier and T. Leweke, “Three-dimensional instability during vortex merging,” *Physics of Fluids*, vol. 13, pp. 2747–2750, Oct. 2001.
- [17] C. Cerretelli and C. H. K. Williamson, “The physical mechanism for vortex merging,” *Journal of Fluid Mechanics*, vol. 475, pp. 41–77, Jan. 2003.
- [18] P. Meunier, S. Le Dizès, and T. Leweke, “Physics of vortex merging,” *Comptes Rendus Physique*, vol. 6, pp. 431–450, May 2005.
- [19] L. K. Brandt and K. K. Nomura, “Characterization of the interactions of two unequal co-rotating vortices,” *Journal of Fluid Mechanics*, vol. 646, pp. 233–253, Mar. 2010.
- [20] D. G. Dritschel and D. W. Waugh, “Quantification of the inelastic interaction of unequal vortices in two-dimensional vortex dynamics,” *Physics of Fluids A: Fluid Dynamics*, vol. 4, pp. 1737–1744, Aug. 1992.

- [21] R. R. Trieling, M. Beckers, and G. J. F. Van Heijst, “Dynamics of monopolar vortices in a strain flow,” *Journal of Fluid Mechanics*, vol. 345, pp. 165–201, Aug. 1997.
- [22] R. R. Trieling and G. J. F. v. Heijst, “Kinematic properties of monopolar vortices in a strain flow,” *Fluid Dynamics Research*, vol. 23, pp. 319–341, Dec. 1998.
- [23] B. Legras and D. Dritschel, “Vortex stripping and the generation of high vorticity gradients in two-dimensional flows,” *Applied Scientific Research*, vol. 51, pp. 445–455, June 1993.
- [24] A. Mariotti, B. Legras, and D. G. Dritschel, “Vortex stripping and the erosion of coherent structures in two-dimensional flows,” *Physics of Fluids*, vol. 6, pp. 3954–3962, Dec. 1994.
- [25] J. K. Harvey and F. J. Perry, “Flowfield produced by trailing vortices in the vicinity of the ground,” *AIAA Journal*, vol. 9, pp. 1659–1660, Aug. 1971.
- [26] A. J. Peace and N. Riley, “A viscous vortex pair in ground effect,” *Journal of Fluid Mechanics*, vol. 129, p. 409, Apr. 1983.
- [27] P. Orlandi, “Vortex dipole rebound from a wall,” *Physics of Fluids A: Fluid Dynamics*, vol. 2, pp. 1429–1436, Aug. 1990.
- [28] W. Kramer, H. J. H. Clercx, and G. J. F. van Heijst, “Vorticity dynamics of a dipole colliding with a no-slip wall,” *Physics of Fluids*, vol. 19, p. 126603, Dec. 2007.
- [29] T. Leweke and C. H. K. Williamson, “Experiments on long-wavelength instability and reconnection of a vortex pair,” *Physics of Fluids*, vol. 23, p. 024101, Feb. 2011.
- [30] S. C. Crow, “Stability theory for a pair of trailing vortices,” *AIAA Journal*, vol. 8, pp. 2172–2179, Dec. 1970.
- [31] S. Kida and M. Takaoka, “Vortex Reconnection,” *Annual Review of Fluid Mechanics*, vol. 26, pp. 169–177, Jan. 1994.

- [32] J. Jimenez, “Stability of a pair of co-rotating vortices,” *Physics of Fluids*, vol. 18, no. 11, p. 1580, 1975.
- [33] S. E. Widnall, D. Bliss, and A. Zalay, “Theoretical and Experimental Study of the Stability of a Vortex Pair,” in *Aircraft Wake Turbulence and Its Detection* (J. H. Olsen, A. Goldburg, and M. Rogers, eds.), pp. 305–338, Boston, MA: Springer US, 1971.
- [34] R. Klein, A. J. Majda, and K. Damodaran, “Simplified equations for the interaction of nearly parallel vortex filaments,” *Journal of Fluid Mechanics*, vol. 288, pp. 201–248, Apr. 1995.
- [35] D. Fabre, L. Jacquin, and A. Loof, “Optimal perturbations in a four-vortex aircraft wake in counter-rotating configuration,” *Journal of Fluid Mechanics*, vol. 451, pp. 319–328, Jan. 2002.
- [36] D. J. Asselin and C. H. K. Williamson, “Influence of a wall on the three-dimensional dynamics of a vortex pair,” *Journal of Fluid Mechanics*, vol. 817, pp. 339–373, Apr. 2017.
- [37] D. Dehtyriov, K. Hourigan, and M. C. Thompson, “Direct numerical simulation of a counter-rotating vortex pair interacting with a wall,” *Journal of Fluid Mechanics*, vol. 884, p. A36, Feb. 2020.
- [38] D. Moore and P. Saffman, “The instability of a straight vortex filament in a strain field,” *Proceedings of the Royal Society of London. A. Mathematical and Physical Sciences*, vol. 346, pp. 413–425, Nov. 1975.
- [39] C.-Y. Tsai and S. E. Widnall, “The stability of short waves on a straight vortex filament in a weak externally imposed strain field,” *Journal of Fluid Mechanics*, vol. 73, pp. 721–733, Feb. 1976.
- [40] S. E. Widnall, D. B. Bliss, and C.-Y. Tsai, “The instability of short waves on a vortex ring,” *Journal of Fluid Mechanics*, vol. 66, pp. 35–47, Oct. 1974.
- [41] T. Leweke and C. H. K. Williamson, “Cooperative elliptic instability of a vortex pair,” *Journal of Fluid Mechanics*, vol. 360, pp. 85–119, Apr. 1998.

- [42] P. Meunier and T. Leweke, “Elliptic instability of a co-rotating vortex pair,” *Journal of Fluid Mechanics*, vol. 533, June 2005.
- [43] G. K. Batchelor, *An introduction to fluid dynamics*. Cambridge, U.K.: Foundation Books, 2007. OCLC: 928892326.
- [44] L. Lacaze, A.-L. Birbaud, and S. Le Dizès, “Elliptic instability in a Rankine vortex with axial flow,” *Physics of Fluids*, vol. 17, pp. 017101–017101–5, Jan. 2005.
- [45] L. Lacaze, K. Ryan, and S. Le Dizès, “Elliptic instability in a strained Batchelor vortex,” *Journal of Fluid Mechanics*, vol. 577, pp. 341–361, Apr. 2007.
- [46] C. Roy, N. Schaeffer, S. Le Dizès, and M. Thompson, “Stability of a pair of co-rotating vortices with axial flow,” *Physics of Fluids*, vol. 20, p. 094101, Sept. 2008.
- [47] K. Ryan, C. J. Butler, and G. J. Sheard, “Stability characteristics of a counter-rotating unequal-strength Batchelor vortex pair,” *Journal of Fluid Mechanics*, vol. 696, pp. 374–401, Apr. 2012.
- [48] H. Igarashi, P. Durbin, H. Hu, and H. Ma, “A Stereoscopic PIV Study of a Near-Field Wingtip Vortex,” in *48th AIAA Aerospace Sciences Meeting Including the New Horizons Forum and Aerospace Exposition*, (Orlando, Florida), American Institute of Aeronautics and Astronautics, Jan. 2010.
- [49] A. Vogt, P. Baumann, J. Kompenhans, and M. Gharib, “Investigations of a wing tip vortex in air by means of DPIV,” in *Advanced Measurement and Ground Testing Conference*, (New Orleans, LA, U.S.A.), American Institute of Aeronautics and Astronautics, June 1996.
- [50] B. Wendt and B. Reichert, “The modelling of symmetric airfoil vortex generators,” in *34th Aerospace Sciences Meeting and Exhibit*, (Reno, NV, U.S.A.), American Institute of Aeronautics and Astronautics, Jan. 1996.
- [51] K. J. Forster, T. J. Barber, S. Diasinos, and G. Doig, “Interactions of a counter-rotating vortex pair at multiple offsets,” *Experimental Thermal and Fluid Science*, vol. 86, pp. 63–74, Sept. 2017.

- [52] K. J. Forster, T. J. Barber, S. Diasinos, and G. Doig, “Interactions of a co-rotating vortex pair at multiple offsets,” *Physics of Fluids*, vol. 29, p. 057102, May 2017.
- [53] K. J. Forster, *The Interactions of Streamwise, Co-rotating and Counter-rotating Vortices*. PhD thesis, University of New South Wales, School of Mechanical and Manufacturing Engineering, Jan. 2018.
- [54] R. F. Huang and C. L. Lin, “Vortex shedding and shear-layer instability of wing at low-Reynolds numbers,” *AIAA Journal*, vol. 33, pp. 1398–1403, Aug. 1995.
- [55] H. K. Versteeg and W. Malalasekera, *An Introduction to Computational Fluid Dynamics: The Finite Volume Method*. Harlow, Essex: Pearson Education, 2nd ed., 2007.
- [56] J. Slotnick, A. Khodadoust, J. Alonso, D. Darmofal, W. Gropp, E. Lurie, and D. Mavriplis, “CFD Vision 2030 Study: A Path to Revolutionary Computational Aerosciences,” *NASA CR-2014-218178*, Mar. 2014.
- [57] S. Ghosh, J.-I. Choi, and J. R. Edwards, “Numerical Simulations of Effects of Micro Vortex Generators Using Immersed-Boundary Methods,” *AIAA Journal*, vol. 48, pp. 92–103, Jan. 2010.
- [58] J. C. Dudek, “Modeling Vortex Generators in a Navier-Stokes Code,” *AIAA Journal*, vol. 49, pp. 748–759, Apr. 2011.
- [59] C.-C. Tseng and Y.-E. Cheng, “Numerical investigations of the vortex interactions for a flow over a pitching foil at different stages,” *Journal of Fluids and Structures*, vol. 58, pp. 291–318, Oct. 2015.
- [60] P. R. Spalart, M. K. Strelets, A. K. Travin, and M. L. Shur, “Modeling the Interaction of a Vortex Pair with the Ground,” *Fluid Dynamics*, vol. 36, no. 6, pp. 899–908, 2001.
- [61] F. R. Menter, “Performance of popular turbulence model for attached and separated adverse pressure gradient flows,” *AIAA Journal*, vol. 30, pp. 2066–2072, Aug. 1992.

- [62] S. B. Wibowo, Sutrisno, and T. A. Rohmat, “Archive of Mechanical Engineering,” 2018. Publisher: Polish Academy of Sciences, Committee on Machine Building.
- [63] D. C. Wilcox, “Reassessment of the scale-determining equation for advanced turbulence models,” *AIAA Journal*, vol. 26, pp. 1299–1310, Nov. 1988.
- [64] *Turbulence, heat, and mass transfer 4: proceedings of the fourth international symposium on turbulence, heat and mass transfer, Antalya, Turkey, 12-17 October, 2003*. New York: Begell House, 2003.
- [65] J. H. Ferziger and M. Perić, *Computational Methods for Fluid Dynamics*. Berlin, Heidelberg: Springer Berlin Heidelberg, 2002. OCLC: 851753498.
- [66] F. Menter, “Improved Two-Equation k-omega Turbulence Models for Aerodynamic Flows,” *NASA Technical Memorandum*, Oct. 1992.
- [67] D. Jones, M. Chapuis, M. Liefvendahl, D. Norrison, and R. Widjaja, “RANS Simulations using OpenFOAM Software,” Jan. 2016.
- [68] G. K. Batchelor, “Axial flow in trailing line vortices,” *Journal of Fluid Mechanics*, vol. 20, pp. 645–658, Dec. 1964.
- [69] C. J. Heaton and N. Peake, “Transient growth in vortices with axial flow,” *Journal of Fluid Mechanics*, vol. 587, pp. 271–301, Sept. 2007.
- [70] P. J. S. A. Ferreira de Sousa and J. C. F. Pereira, “Laminar co-rotating Batchelor vortex merging,” *Theoretical and Computational Fluid Dynamics*, vol. 23, pp. 1–14, Mar. 2009.
- [71] M. R. Ruith, P. Chen, E. Meiburg, and T. Maxworthy, “Three-dimensional vortex breakdown in swirling jets and wakes: direct numerical simulation,” *Journal of Fluid Mechanics*, vol. 486, pp. 331–378, June 2003.
- [72] S. P. Jammy, *Direct Numerical Simulation of Vortices*. PhD thesis, University of Surrey, Oct. 2015.
- [73] S. Ragab and M. Sreedhar, “Numerical simulation of vortices with axial velocity deficits,” *Physics of Fluids*, vol. 7, pp. 549–558, Mar. 1995.

- [74] F. Viola, C. Arratia, and F. Gallaire, “Mode selection in trailing vortices: harmonic response of the non-parallel Batchelor vortex,” *Journal of Fluid Mechanics*, vol. 790, pp. 523–552, Mar. 2016.
- [75] U. Fernandez, P.-E. Rethore, N. N. Sorensen, C. M. Velte, F. Zahle, and E. Egusquiza, “Comparison of four different models of vortex generators,” in *Proceedings of EWEA 2012 - European Wind Energy Conference & Exhibition*, (Denmark), 2012.
- [76] A. Revell, G. Iaccarino, and X. Wu, “Advanced RANS modeling of wingtip vortex flows,” 2006.
- [77] P. J. Roache, “QUANTIFICATION OF UNCERTAINTY IN COMPUTATIONAL FLUID DYNAMICS,” *Annual Review of Fluid Mechanics*, vol. 29, pp. 123–160, Jan. 1997.
- [78] H. Schlichting, *Boundary Layer Theory*. The McGraw-Hill Companies, 7th ed., 1979.
- [79] J. Dacles-Mariani, G. G. Zilliac, J. S. Chow, and P. Bradshaw, “Numerical/experimental study of a wingtip vortex in the near field,” *AIAA Journal*, vol. 33, pp. 1561–1568, Sept. 1995.
- [80] M. A. van den Berg, *Aerodynamic Interaction of an Inverted Wing with a Rotating Wheel*. PhD thesis, University of Southampton, School of Engineering Sciences, 2007.
- [81] A. Stephan, F. Holzäpfel, and T. Misaka, “Aircraft Wake-Vortex Decay in Ground Proximity—Physical Mechanisms and Artificial Enhancement,” *Journal of Aircraft*, vol. 50, pp. 1250–1260, July 2013.
- [82] F. Holzäpfel, T. Hofbauer, D. Darracq, H. Moet, F. Garnier, and C. F. Gago, “Analysis of wake vortex decay mechanisms in the atmosphere,” *Aerospace Science and Technology*, vol. 7, pp. 263–275, June 2003.